

Numerical Investigations on the Static Aeroelasticity of a Sailplane with a Morphing Forward Wing Section

Term Thesis

Submitted in partial fulfillment of the requirements for the degree
M.Sc. Aerospace at the Department of Mechanical Engineering
of the Technical University of Munich.

Supervised by Prof. Dr.-Ing. Mirko Hornung
Fabian Sturm, M.Sc.
Institute of Aircraft Design

Submitted by Gerrit Illenberger, B.Sc.
Student ID: 3638597

Submitted on April 1, 2019

Sequential number LS-SA 18/20

Abstract

An alternative structural concept in the wing design of sailplanes is the combination of a morphing forward wing section with a conventional trailing edge flap. Since the load-bearing wing cross section is reduced by a droop nose, the torsional stiffness of the structure decreases. This leads, under aerodynamic load, to undesirable twisting, which in turn deteriorates the aerodynamic efficiency of the wing. The present thesis deals with the investigation of a structural preliminary design with regard to its static aeroelastic deformation behavior. For this purpose, a simulation model is developed, enabling coupled aerodynamic and structural numerical analysis. Simulation results show that a morphing forward wing section contributes substantially to the overall wing torsional stiffness and has to be taken into account for further aeroelastic analysis. In order to counteract wing twisting, the effect of targeted layup variations, causing structural bending-twisting couplings, is shown. By means of Aeroelastic Tailoring it is possible to eliminate wing twisting for certain load cases identified in this thesis. Thus, the novel structural concept becomes feasible despite its reduced torsional stiffness. The developed model serves for further static and dynamic aeroelastic investigations.

Keywords: Aeroelasticity, Aeroelastic Tailoring, DLM, FEM, Morphing Wing

Contents

List of Figures	VI
List of Tables	VII
Nomenclature	X
1 Introduction and Motivation	1
2 State of the Art	4
2.1 Static Aeroelastic Responses	4
2.1.1 Twist of a two-dimensional rigid Airfoil	5
2.1.2 Twist of a fixed Root flexible Wing	7
2.1.3 Effect of Trim on Static Aeroelastic Behavior	9
2.2 Aeroelastic Tailoring	10
2.3 Finite Element Method	15
2.4 Doublet Lattice Method	17
3 Simulation Model Generation	20
3.1 Workflow	20
3.2 Geometry Model	21
3.2.1 Data Import	21
3.2.2 Geometry Design	22
3.2.3 Geometry Manipulation	24
3.3 Finite Element Model	25
3.3.1 Material Parameters and Layup	25
3.3.2 Wing Structure Model	29
3.3.3 Boundary Conditions	31
3.3.4 Fuselage and Empennage Model	32
3.3.5 Interface Model	32
3.4 Mass Model	33
3.4.1 Structural Mass	33
3.4.2 Ballast	34
3.4.3 Center of Gravity	34

3.5	Doublet Lattice Model	36
3.5.1	Aerodynamic Panel Model	37
3.5.2	Camber and Twist Correction	38
3.5.3	Coupling	40
4	Design Studies	41
4.1	Model Validation	41
4.1.1	Analysis of Influencing Parameters	41
4.1.2	Simulation Preparation	42
4.1.3	Identification of Load Cases	44
4.1.4	Comparison of Simulation Results	45
4.2	Investigations on Static Aeroelastic Responses	53
4.2.1	Supplementation of Load Cases	53
4.2.2	Analysis of Simulation Results	55
4.2.3	Effect of Aeroelastic Tailoring	63
5	Conclusion and Outlook	67
	Bibliography	69
A	Appendix	A-1

List of Figures

1.1	Laminar airfoil with droop nose and trailing edge flap (Weinzierl et al. 2015).	1
1.2	MILAN structural concept with morphing forward wing section and compliant mechanism rib (Achleitner 2016).	2
1.3	Wing cross sections with load-bearing components (dotted) for conventional design (above) and for the MILAN concept (below) (Wiessmeier 2011).	3
2.1	Collar's aeroelastic triangle (Wright 2015).	4
2.2	Two-dimensional airfoil with a torsional spring (Wright 2015).	5
2.3	Typical twist behavior for a wing cross section (Wright 2015).	7
2.4	Flexible rectangular wing with fixed root (Wright 2015).	7
2.5	Aircraft in steady flight (Wright 2015).	9
2.6	Wing tip twist and incidence for an aircraft with a flexible wing in trim (Wright 2015).	10
2.7	Outward redistribution of lift due to the increased twist towards the wing tip.	11
2.8	ABD matrix entries and their effect on loading-deformation coupling (Drechsler & Hartmann 2017).	12
2.9	Influence of the D submatrix entries on the deformation behavior of a non-swept wing (Shirk & Hertz 1984).	13
2.10	CAD rendering of the open class sailplane <i>Concordia</i> (Butler 2011).	14
2.11	<i>Concordia</i> wing twist under conventional lamination scheme and applying Aeroelastic Tailoring during cruise flight. Reconstructed from (Butler 2011).	14
2.12	<i>Concordia</i> wing twist under conventional lamination scheme and applying Aeroelastic Tailoring during thermaling flight. Reconstructed from (Butler 2011).	15
2.13	Basic element types in NASTRAN (MSC 2016a).	16
2.14	Aerodynamic surface, discretized into boxes for the DLM application (Albano & Rodden 1969).	17
3.1	Schematic representation of the workflow for the simulation model generation.	20
3.2	Wing planform with according airfoils used for model generation from preliminary studies.	21
3.3	Definition of coordinate systems.	21
3.4	CAD imported geometry data.	22

3.5	Interrupted upper shell for the integration of an airbrake box.	23
3.6	Cut upper shell and c web for the integration of control rod ducts.	23
3.7	Wing root geometry.	24
3.8	CAD shell model with all components.	25
3.9	Cross section of a UD composite ply (Drechsler et al. 2017).	27
3.10	Thickness distribution for the upper and the lower spar cap from a preliminary structural design by a project partner.	30
3.11	RBE2 actuators attach the compliant mechanisms (hidden) to the spar web via RBE3 connections. RBE2 normal force joints close the open wing cross section.	31
3.12	Interface model with chordwise RBE2 elements and coupling RBE3 elements for the morphing forward wing section (hidden) and the wing box (only spar and c web displayed).	33
3.13	Discrete mass grid points and their RBE3 attachment to the wing box.	34
3.14	Schematic illustration of the lever arms with respect to the aircraft coordinate system for the determination of the centers of gravity.	35
3.15	FE model with wing including morphing forward wing section, fuselage, empennage and interface.	36
3.16	Order of box numbering.	37
3.17	Aerodynamic panel model for the wing and the horizontal stabilizer including elevator.	38
3.18	Camber (a) and twist (b) correction for a row of DLM boxes in chord direction (Dillinger 2014).	38
3.19	Camber evaluation at the Pistolesi points of chordwise DLM boxes in unmorphed (a) and morphed (b) configuration.	39
4.1	Primary structure excluding morphing forward wing section. Twist with respect to the y -axis at load case 101.	46
4.2	Reference axes to describe wing twist.	47
4.3	Wing twist at load case 101. Continuous lines refer to the non-deformed elastic axis, the dot-dashed line refers to the deformed elastic axis.	47
4.4	Wing deflection at load case 101.	49
4.5	Local lift coefficient distribution at load case 101.	50
4.6	Elliptical lift distribution at load case 101.	51

4.7	Local lift coefficient distribution at load case 103.	51
4.8	Wing twist with respect to the non-deformed elastic axis at load case 103.	52
4.9	Local lift coefficient distribution at load case 117.	53
4.10	Increasing load factor due to centrifugal force Z in stationary level circle flight.	54
4.11	Primary structure including morphing forward wing section. Twist with respect to the y -axis at load case 101.	56
4.12	Effect of morphing forward wing section on twist behavior at load case 101.	57
4.13	Effect of morphing forward wing section on deflection behavior at load case 101.	58
4.14	Effect of morphing forward wing section on local lift coefficient distribution at load case 101.	58
4.15	Effect of morphing forward wing section on elliptical lift distribution at load case 101.	59
4.16	Wing twist at load case 201.	60
4.17	Elliptical lift distribution at load case 201.	61
4.18	Wing deflection at load case 201.	61
4.19	Wing twist at load case 202.	62
4.20	Elliptical lift distribution at load case 202.	63
4.21	Orientation of fibers for conventional layup scheme (a) and applying Aeroelastic Tailoring for the wing box (b).	64
4.22	Effect of ply angle variation at load case 101.	64
4.23	Effect of ply angle variation at load case 201.	65
4.24	Effect of ply angle variation at load case 202.	65

List of Tables

3.1	Available input data for anisotropic materials.	26
3.2	Available input data for isotropic materials.	26
3.3	Physical properties of fibers and matrix and resulting ply thicknesses.	27
3.4	Masses and corresponding center of gravity locations in MTOM configuration.	35
4.1	Selected values of the ISA, related to MSL (ICAO 1976).	43
4.2	Relevant load cases to compare for model validation.	44
4.3	NASTRAN SOL144 input values for model validation.	45
4.4	Relevant load cases for further aeroelastic investigations.	55
4.5	NASTRAN SOL144 input values for further aeroelastic investigations.	55

Nomenclature

Acronyms

AC	Aerodynamic center
CAD	Computer Aided Design
CAS	Calibrated Air Speed
CF	Carbon fiber
CLT	Classical Laminate Theory
DLM	Doublet Lattice Method
EAS	Equivalent Air Speed
EASA	European Union Aviation Safety Agency
FEM	Finite Element Method
GF	Glass fiber
HM	High modulus
HM	High tenacy
ICAO	International Civil Aviation Organization
ISA	International Standard Atmosphere
MAC	Mean aerodynamic chord
MILAN	Morphing Wings for Sailplanes
MSL	Mean sea level
MTOM	Maximum Take-Off Mass
NLP	Non-lifting parts
PEEK	Polyether ether ketone
UD	Unidirectional

Greek Symbols

α	Angle of attack
δ	Increment
ϵ	Strain
γ	Shear strain
κ	Kurvature, isentropic expansion coefficient
ν	Poisson's ratio
ϕ	Dihedral
ρ	Density
σ	Stress
θ	Incidence angle, twist angle, bank angle
φ_F	Fiber volume content

Indices

0	Base value
A	Aerodynamic, aeroelastic, aircraft, maneuvering
a	Aerodynamic
B	Ballast
D	Dive
div	Divergence
e	External
EA	Elastic axis
F	Fiber
g	Geometric
i	Matrix index, supporting point
j	Matrix index, box index
k	Ply index
M	Matrix
S	Structural, stall
T	Wing tip
W	Wing
x, y, z	Reference directions

Latin Symbols

AIC	Aerodynamic influence matrix
D	Relation matrix
f	Force
H	Coupling matrix
K, k	Stiffness matrices
p	Pressure
S	Box surface
u	Displacement
w	Downwash
A	Area
a	Speed of sound
A, B, D	Coupling terms of CLT
c	Chord length
c_L	Wing lift coefficient
c_l	Airfoil lift coefficient
c_m	Airfoil moment coefficient

d	Differential
E	Young's modulus
e	Aerodynamic center eccentricity
G	Shear modulus
g_0	Gravitational constant
GJ	Torsional rigidity
K_θ	Torsional spring stiffness
L	Lift
l	Lift per unit span
M	Moment
m	Laminate moment, mass
Ma	Mach number
N	Number of DLM boxes
n	Laminate force, ply number, leading edge point, load factor
q	Dynamic pressure
s	Wing semi-span
S_{wing}	Wing reference area
T	Temperature, thickness
t	Ply thickness
U	Energy
u	Vertical acceleration
V	Velocity, Volume
W	Work
w	Width
X, Y, Z	Aircraft coordinates
x, y, z	Wing coordinates
Z	Centrifugal force
z_k	Distance from ply bottom to laminate mid-plane
\bar{Q}	Composite stiffness matrix
ABD	Coupling matrix of CLT

1 Introduction and Motivation

The construction of sailplanes has been an ingenious tradition with numerous inventions since the early pioneering years of Otto Lilienthal. Especially in recent decades, there have been two major milestones in the development of sailplanes. The first was the introduction of laminar profiles, which significantly improved aerodynamic performance. The second was the innovative utilization of fiber composites, which led to a widening of the structural dimensions towards greater aspect ratios and, coupled with the use of laminar profiles, thinner wing cross sections. Today, commercial sailplane manufacturers focus more on alternative propulsion concepts, and from an aerodynamic-structural point of view, development work seems to be stagnating for cost reasons. Research into alternative aircraft concepts is more likely to be carried out at universities and, in the case of sailplanes, only takes place in prototype construction.

Regarding airfoil design, there are a number of requirements that have to be met. For one thing, gliding at low speeds, i.e. thermaling flight and landing, demands relatively high lift coefficients. On the other hand, only low values occur at high cruising speeds, and correspondingly low drag coefficients are desirable for maximum aerodynamic efficiency. Both can be achieved through the conventional and compromising use of trailing edge flaps by adjusting the airfoil camber to the respective flight condition.

The MILAN (Morphing Wings for Sailplanes) project was initiated at the Technical University of Munich and is currently being promoted by the Institute of Aircraft Design in cooperation with several industrial partners. The goal is to develop a wing with an adaptive forward section combined with a conventional trailing edge flap, which is illustrated in figure 1.1.



Figure 1.1: Laminar airfoil with droop nose and trailing edge flap (Weinzierl et al. 2015).

By morphing the forward section of the wing, which is realized by spanwise distributed *compliant mechanisms* as depicted in figure 1.2, the low-drag lift coefficient range within the region of laminar flow can be extended by approximately 25 % to higher lift coefficients.

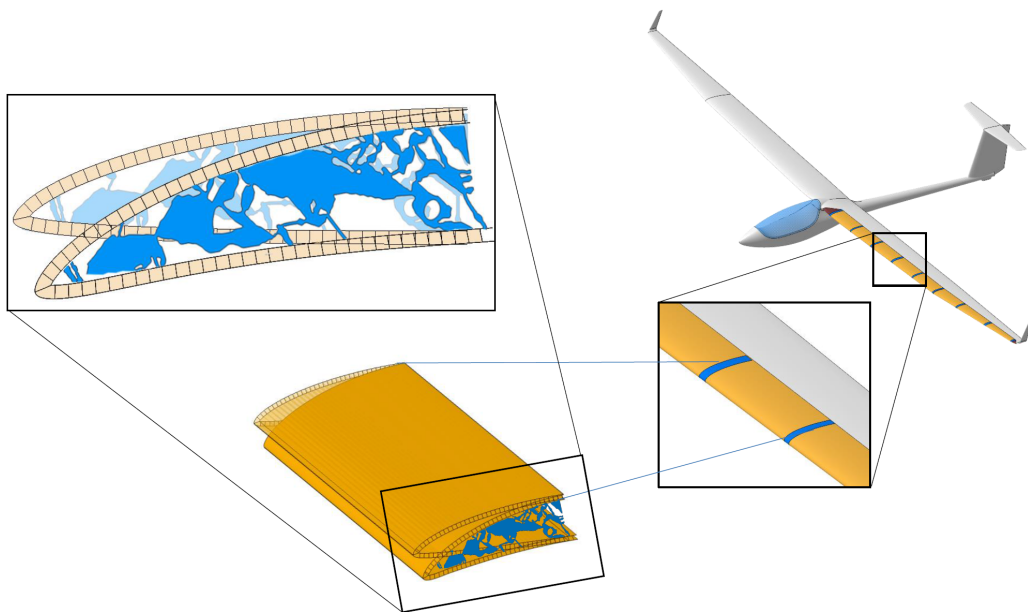


Figure 1.2: MILAN structural concept with morphing forward wing section and compliant mechanism rib (Achleitner 2016).

This structurally novel concept allows a reduction of the wing area and thus an increase of the wing loading, shifting the aerodynamic efficiency in unmorphed airfoil configuration towards higher speeds while maintaining the high lift demanding circular flight characteristics in morphed configuration at low speeds. Thus it meets the demands of modern competitive and record gliding. However, the gain in performance is also accompanied by challenges with regard to the structural design of the wing. The variable shape of the forward section results in a modified structural layout to a conventional wing with a rigid forward section. The front area is no longer fully available as a closed cross section, so that the rear area has to contribute the main part of the torsional stiffness. The backward movement of the spar and the open cross section the morphing skin cause a rearward position of shear center around which the wing twists according to figure 1.3.

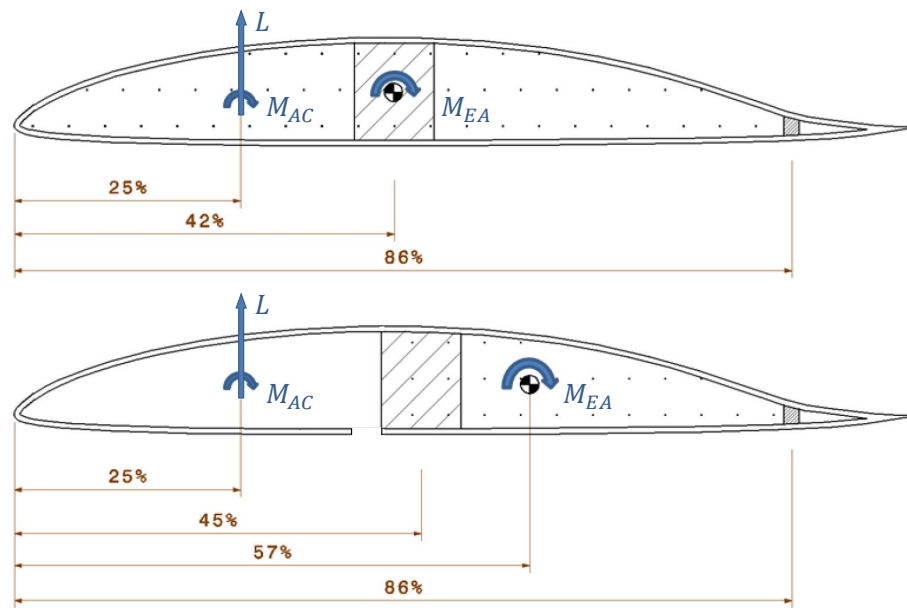


Figure 1.3: Wing cross sections with load-bearing components (dotted) for conventional design (above) and for the MILAN concept (below) (Wiessmeier 2011).

The MILAN wing is designed in such a way that an elliptical lift distribution is achieved, keeping the induced drag low. Torsion of the wing by aerodynamic forces is undesirable, as it would lead to an increase in drag, lowering the aerodynamic efficiency. In order to counteract this phenomenon by design, a detailed static aeroelastic analysis of the wing becomes necessary. Therefore, a complex simulation model is developed, considering coupled elastic and aerodynamic forces. Based on the results of preliminary studies, a Computer Aided Design (CAD) geometry is generated to build a Finite Element (FE) model. This will be coupled with an aerodynamic model according to the Doublet Lattice Method (DLM). The coupled model will then be used for static aeroelastic simulations in order to investigate the wing for its torsion and the induced redistribution of lift. Various representative load cases are identified for this purpose. The aeroelastic optimization of an early wing design (Schlothauer 2016) has already provided valuable findings regarding the structural feasibility of the concept. However, aerodynamic forces have been simplified in these investigations and not coupled with structural deformations, so that the results are only a first approximation. The present thesis is intended to provide a more accurate aeroelastic evaluation at the current point of development with completely different geometry and airfoil data. Special attention is given to show the bending-torsion coupling effect of composite layup modification by means of Aeroelastic Tailoring. This is to optimize the wing with regard to its aerodynamic efficiency for the further development.

2 State of the Art

2.1 Static Aeroelastic Responses

Generally, it can be distinguished between dynamic and static aeroelasticity. The former includes structural, aerodynamic and inertial forces whereas the latter only combines the first two mentioned according to figure 2.1.

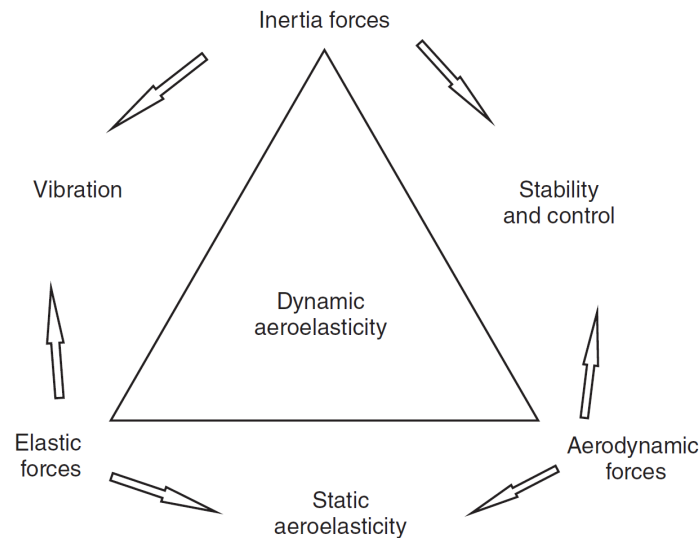


Figure 2.1: Collar's aeroelastic triangle (Wright 2015).

Static aeroelasticity considers the deformation behavior of a flexible structure under static or quasi-static, i.e. time independent, aerodynamic loading. Lift and drag cause a flexible wing structure to bend and twist, changing the local angle of attack and thus the stream flow. This in turn changes the distribution of aerodynamic forces acting on the structure, thus bending and twisting, until an equilibrium state is achieved. Regarding aircraft, static aeroelasticity governs the lift and drag distribution in wing span direction, the control effectiveness as well as the trim behavior and the static stability in each flight condition (Wright 2015). Therefore, knowledge about static aeroelastic responses is crucial in aircraft design.

To describe the aeroelastic behavior of any structure, the following parameters are defined:

- The *shear center* of a two-dimensional cross section describes the point at which a transverse force has to attack without inducing twist of this cross section.
- The *flexural center*, on the other hand, is the point at which a transverse force has to attack in order to have zero twist with respect to the wing root.

- Furthermore, the *elastic axis* is defined to be the connection of all shear centers along the wing span, whereas
- the *flexural line* connects all flexural centers.

The twist behavior of wings mostly refers to the latter, although the former has become established in general linguistic usage (Wright 2015). This is why the term elastic axis, actually meaning the flexural axis, is utilized to describe the wing torsional behavior in this thesis. All outlines are based on the assumption that this axis lies beyond the aerodynamic center (AC).

2.1.1 Twist of a two-dimensional rigid Airfoil

In order to describe the twist that results from lift, a two-dimensional rigid and symmetric wing cross section is considered as depicted in figure 2.2.

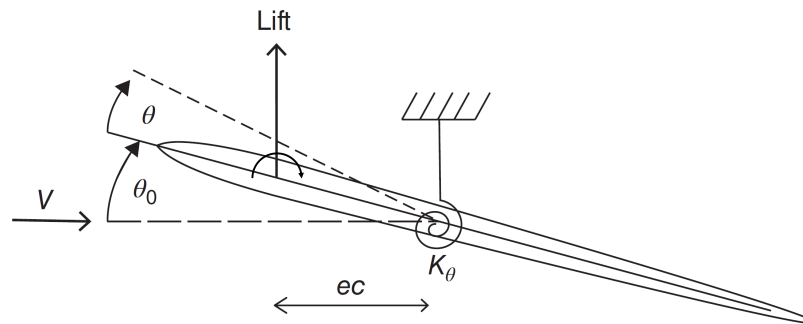


Figure 2.2: Two-dimensional airfoil with a torsional spring (Wright 2015).

The airfoil with an initial incidence angle of θ_0 rotates around its shear center with an unknown twist angle θ due to the aerodynamic force. For the following considerations it is assumed that only the lift component induces twisting, which is reasonable for small angles where drag has negligibly small lever arms. The lift L and the resulting moment M_{EA}^A per unit span become

$$L = q c c_l = q c c_{l_\alpha} (\theta_0 + \theta) \quad (2.1)$$

$$M_{EA}^A = M_{AC} + L e c = q c^2 (c_{m_{AC}} + e c_{l_\alpha} (\theta_0 + \theta)) \quad (2.2)$$

with e the dimensionless distance of the aerodynamic center to the shear center in terms of the local chord length c , c_{l_α} the constant gradient of the airfoil lift coefficient, M_{AC} the lift induced moment in the AC, $c_{m_{AC}}$ the according moment coefficient and q the dynamic pressure:

$$q = \frac{\rho}{2} V^2 \quad (2.3)$$

with ρ the air density and V the free stream velocity.

The structural moment M_{EA}^S that counteracts the aerodynamic pitching can be described by the stiffness K_θ of a torsional spring:

$$M_{EA}^S = K_\theta \theta \quad (2.4)$$

By setting equation (2.2) and (2.4) equal and solving for θ results in a direct expression for the structural torsional deflection:

$$\theta = \frac{q c^2 (c_{mAC} + e c_{l_\alpha} \theta_0)}{K_\theta - q e c^2 c_{l_\alpha}} \quad (2.5)$$

The above equation indicates that the torsional deflection depends on the position of the shear center with respect to the aerodynamic center (i.e. quarter chord) and that growing values for e accompany with increasing aerodynamic moments. Furthermore, the structural torsional stiffness is reduced by the aerodynamic term with increasing dynamic pressure. If the denominator becomes to zero, i.e. the aerodynamic pitching moment exceeds the structural restoring moment, twist theoretically goes to infinity, which is the phenomenon of aeroelastic *divergence*. The according value for the dynamic pressure q_{div} yields from setting the denominator to zero and solving for q :

$$q_{div} = \frac{K_\theta}{e c^2 c_{l_\alpha}} \quad (2.6)$$

Equation (2.5) then can be rewritten in terms of the divergence dynamic pressure:

$$\theta = \frac{(q/q_{div})}{(1 - q/q_{div})} \theta_0 \quad (2.7)$$

Figure 2.3 illustrates the typical divergence behavior, whereby it is recognizable that in the absence of aerodynamic forces, i.e. zero dynamic pressure, there is a limit value that is described by the initial incidence. For growing dynamic pressures aerodynamic forces exceed the structural resistance until divergence is reached at q_{div} , where twist tends to infinity. In practice, however, the structure will fail at lower speeds due to *flutter*.

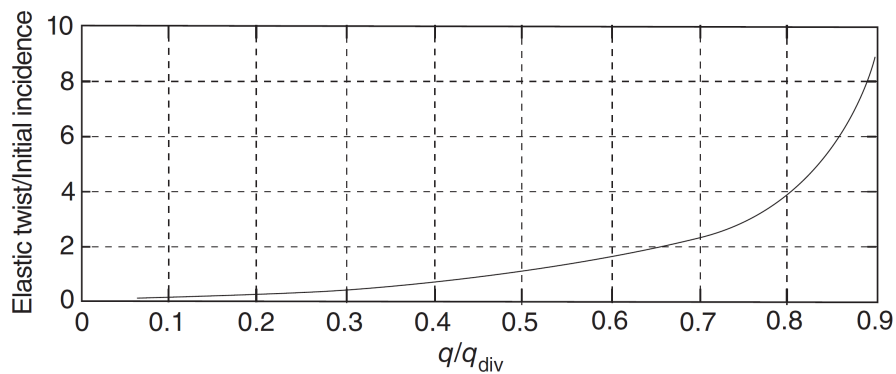


Figure 2.3: Typical twist behavior for a wing cross section (Wright 2015).

2.1.2 Twist of a fixed Root flexible Wing

In figure 2.4 a flexible rectangular wing structure is considered. It has a symmetrical airfoil along the entire span and is fixed at the root, where the angle of attack is θ_0 .

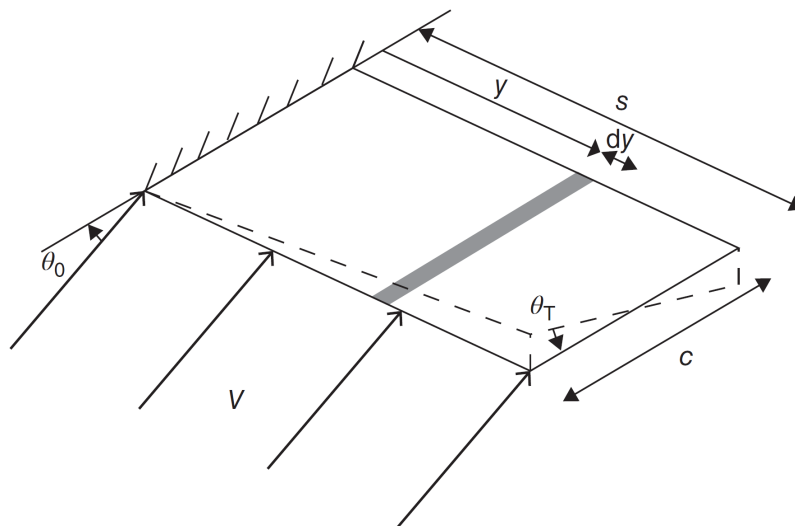


Figure 2.4: Flexible rectangular wing with fixed root (Wright 2015).

At zero angle of attack $\theta_0 = 0^\circ$ there is no pitching moment due to the absence of lift. For any positive incidence, the lift acting on a strip with infinitesimal width dy becomes

$$dL = q c c_{L_\alpha} \left(\theta_0 + \frac{y}{s} \theta_T \right) dy \quad (2.8)$$

with c_{L_α} the gradient of the wing lift coefficient, s the semi-span and θ_T the aeroelastic twist at the wing tip.

Integrating equation (2.8) over the semi-span yields the total lift L of the wing:

$$L = \int_0^s q c c_{L_\alpha} \left(\theta_0 + \frac{y}{s} \theta_T \right) dy = q c c_{L_\alpha} \left(s \theta_0 + \frac{s}{2} \theta_T \right) \quad (2.9)$$

For static aeroelastic considerations there is no kinetic energy, hence the system solely stores potential energy that corresponds to the strain energy due to twist, where bending is neglected:

$$U = \frac{1}{2} \int_0^s GJ \left(\frac{d\theta}{dy} \right)^2 dy = \frac{1}{2} \int_0^s GJ \left(\frac{d\theta_T}{s} \right)^2 dy = \frac{GJ}{2s} \theta_T^2 \quad (2.10)$$

with GJ the torsional rigidity of the structure, defined about the elastic axis. An incremental twist angle $\delta\theta$ can be expressed in the form

$$\delta\theta = \frac{y}{s} \delta\theta_T \quad (2.11)$$

Integrating the incremental twist induced work components on each strip over the semi-span yields the total incremental work δW :

$$\begin{aligned} \delta W &= \int_0^s dL e c \delta\theta = \int_0^s q c c_{L_\alpha} \left(\theta_0 + \frac{y}{s} \theta_T \right) e c \delta\theta dy \\ &= \int_0^s q c^2 c_{L_\alpha} \left(\theta_0 + \frac{y}{s} \theta_T \right) e \frac{y}{s} \delta\theta_T dy = q e c^2 c_{L_\alpha} \left(\frac{s \theta_0}{2} + \frac{s \theta_T}{3} \right) \delta\theta_T \end{aligned} \quad (2.12)$$

The application of Lagrange's equation (Wright 2015) for the generalized coordinate θ_T gives

$$\frac{GJ \theta_T}{s} = q e c^2 c_{L_\alpha} \left(\frac{s \theta_0}{2} + \frac{s \theta_T}{3} \right) \quad (2.13)$$

Solving equation (2.13) for θ_T yields an expression for the wing tip twist in terms of the initial incidence θ_0 :

$$\theta_T = \frac{3 q e c^2 s^2 c_{L_\alpha}}{6 GJ - 2 q e c^2 s^2 c_{L_\alpha}} \theta_0 \quad (2.14)$$

In the same manner as shown in equation (2.5), the structural resistance is reduced by the dynamic pressure in the denominator of equation (2.14).

Setting this to zero and solving for q yields the wing divergence dynamic pressure q_W :

$$q_W = \frac{3 GJ}{e c^2 s^2 c_{L_\alpha}} \quad (2.15)$$

It becomes clear, that increasing dynamic pressures result in higher wing tip twists until theoretically divergence occurs at q_W . In practice, however, the root fixed structure will fail first.

2.1.3 Effect of Trim on Static Aeroelastic Behavior

The configuration that corresponds to the aeroelastic simulation in this thesis is that of a trimmed aircraft that can experience pitch and heave motions. For the sake of simplicity, in this example it is assumed that only the wing generates lift whose point of attack coincides with the center of gravity and no force components occur in the direction of flow. Figure 2.5 shows an aircraft in such a configuration during steady level flight.

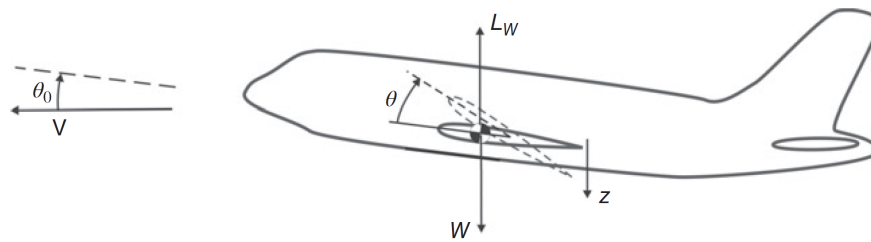


Figure 2.5: Aircraft in steady flight (Wright 2015).

In a similar way as the divergence dynamic pressure q_{div} for a two-dimensional airfoil and q_W for a wing with fixed root have been derived, an expression for a trimmed aircraft can be found by equation (2.16). For its derivation reference is made to further literature (Wright 2015).

$$q_A = \frac{12 GJ}{e c^2 s^2 c_{L_\alpha}} = 4 q_W \quad (2.16)$$

It becomes clear that the divergence dynamic pressure for a trimmed aircraft q_A is four times that of the fixed root wing and thus double the divergence speed according to equation (2.3).

Figure 2.6 illustrates normalized values for the wing tip twist θ_T and the root incidence θ_0 . Whereas the above diagram shows the same course as for the two-dimensional airfoil, the diagram below indicates that for increasing dynamic pressures the root incidence decreases and even become negative for values greater than the divergence dynamic pressure q_W for the fixed root wing.

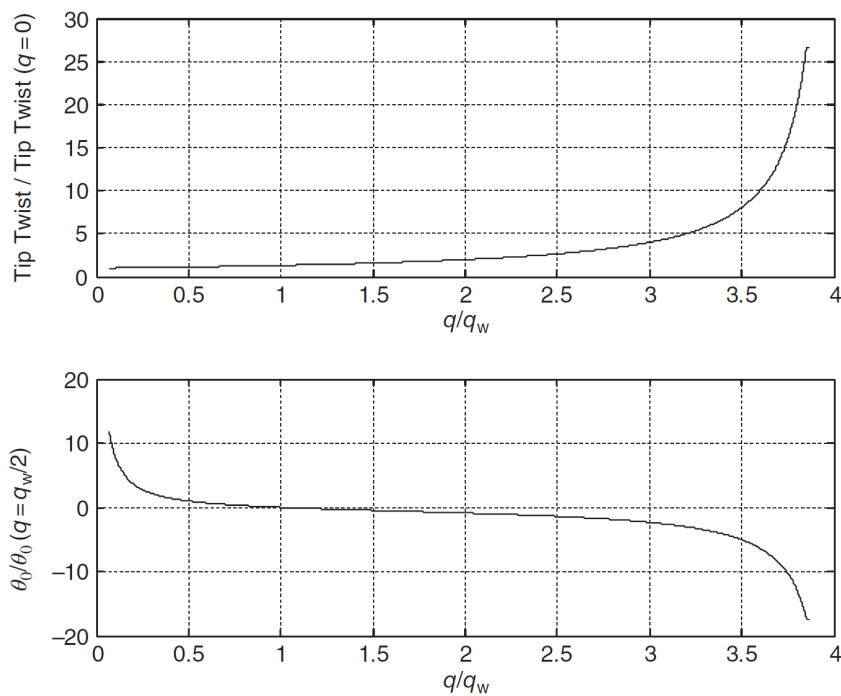


Figure 2.6: Wing tip twist and incidence for an aircraft with a flexible wing in trim (Wright 2015).

At $q = q_A = 4q_w$ both the twist values for the wing tip and the root tend to infinity but with opposite signs, which again implies structural failure. However, the aircraft will leave the trimmable speed range even at lower values for the dynamic pressure. This is the reason why divergence of wings is unlikely to occur from a practical point of view (Wright 2015).

Nevertheless, the described phenomena are important for aircraft design and do not change in their significance with the addition of further influencing variables that determine the exact trim parameters of an aircraft. An innovative method providing a remedy for wing twist and divergence will be presented in chapter 2.2.

2.2 Aeroelastic Tailoring

In general, aeroelastic twist induces an outward redistribution of lift according to figure 2.7. This is associated with an increase in induced drag and a deterioration in the aerodynamic efficiency of the wing. Furthermore, the increased bending moment at the root requires structural reinforcement in this area, which is associated with an increase in weight.

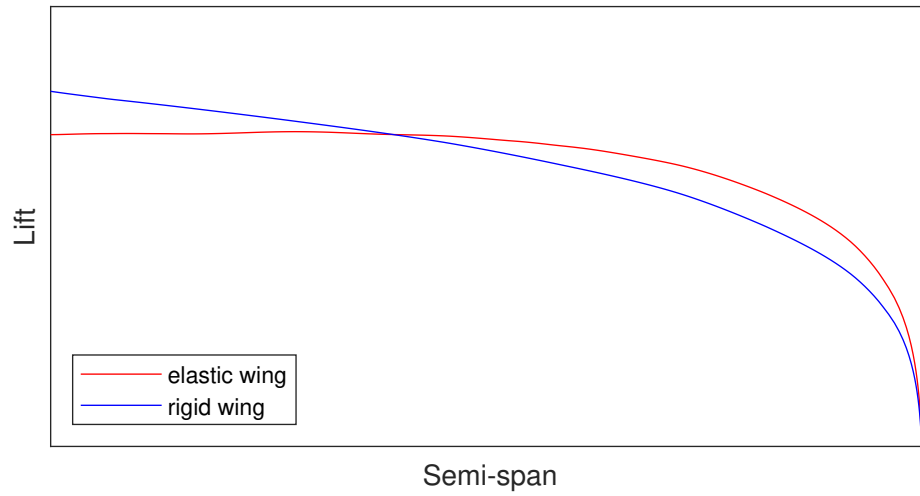


Figure 2.7: Outward redistribution of lift due to the increased twist towards the wing tip.

The basic idea of Aeroelastic Tailoring is to make use of the anisotropic material behavior of composites in order to achieve a bending-torsion coupling by varying the laminate layup, which counteracts the aeroelastic twist. This is done by specifically influencing the ABD matrix treated in the classical laminate theory (CLT). The ABD matrix establishes a direct relationship between laminate forces and moments as well as the resulting deformations.

$$\begin{Bmatrix} n_x \\ n_y \\ n_{xy} \\ m_x \\ m_y \\ m_{xy} \end{Bmatrix} = \begin{bmatrix} A_{11} & A_{12} & A_{16} & B_{11} & B_{12} & B_{16} \\ A_{12} & A_{22} & A_{26} & B_{12} & B_{22} & B_{26} \\ A_{16} & A_{26} & A_{66} & B_{16} & B_{26} & B_{66} \\ \hline B_{11} & B_{12} & B_{16} & D_{11} & D_{12} & D_{16} \\ B_{12} & B_{22} & B_{26} & D_{12} & D_{22} & D_{26} \\ B_{16} & B_{26} & B_{66} & D_{16} & D_{26} & D_{66} \end{bmatrix} \begin{Bmatrix} \epsilon_x^0 \\ \epsilon_y^0 \\ \gamma_{xy}^0 \\ \kappa_x \\ \kappa_y \\ \kappa_{xy} \end{Bmatrix} \quad (2.17)$$

The submatrices A , B and D denote extensional stiffness matrix, bending-extension coupling stiffness matrix and bending stiffness matrix respectively. They become

$$A_{ij} = \sum_{k=1}^n \bar{Q}_{ij,k} t_k \quad (2.18)$$

$$B_{ij} = \sum_{k=1}^n \bar{Q}_{ij,k} t_k \left(z_k - \frac{t_k}{2} \right) \quad (2.19)$$

$$D_{ij} = \sum_{k=1}^n \bar{Q}_{ij,k} \left(\frac{t_k^3}{12} + t_k \left(z_k - \frac{t_k}{2} \right)^2 \right) \quad (2.20)$$

where \bar{Q}_k results from the individual relation between stresses σ_k and strains ϵ_k for every ply k with thickness t_k and distance z_k to the middle plane of the laminate with n layers:

$$\sigma_{i,k} = \bar{Q}_{i,j,k} \epsilon_{j,k} \quad (2.21)$$

Figure 2.8 illustrates the implications of the individual ABD matrix entries on the deformation behavior of a composite part under certain loading conditions.

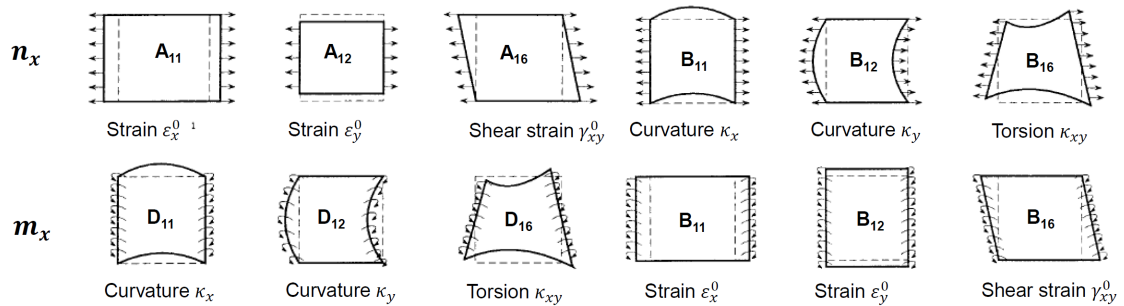


Figure 2.8: ABD matrix entries and their effect on loading-deformation coupling (Drechsler & Hartmann 2017).

In general, a symmetric layup is aimed at when designing composite structures. In this case, the B submatrix becomes zero and the corresponding laminate does not undergo any bending-extension coupling. The components D_{16} and D_{26} representing the bending-torsion coupled behavior of the laminate are particularly essential for Aeroelastic Tailoring. Figure 2.9 schematically shows the influence of the main fiber directions on the entries of the D submatrix and their influence on the wing deformation.

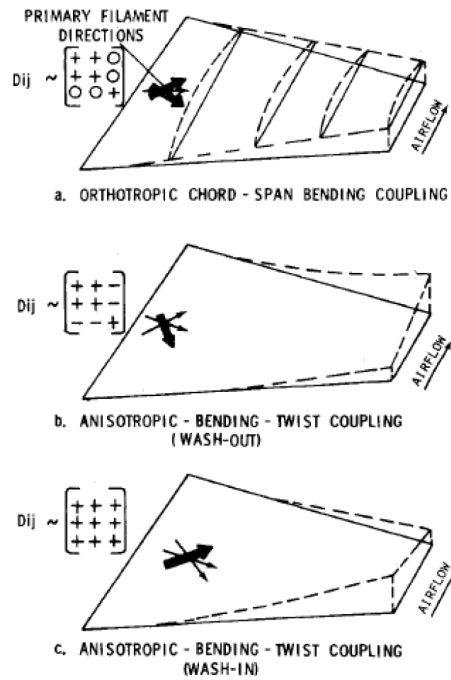


Figure 2.9: Influence of the D submatrix entries on the deformation behavior of a non-swept wing (Shirk & Hertz 1984).

Where the targeted influence on the entries of the ABD matrix in geometrically simple composite structures seems analytically feasible, this develops into a highly sophisticated numerical optimization problem for complex wing structures under certain boundary conditions (Schlothauer 2016).

A suitable method for solving this numerical problem is the FEM coupled with an optimization algorithm. Thus, sensitivities and structural responses can be analyzed depending on selected design variables. In Aeroelastic Tailoring, these include in particular the materials used and their orientation, i.e. the fiber angles and ply thicknesses, in each part. By varying the design variables during the optimization process it is possible to achieve the desired structural behavior under certain loads (Dillinger et al. 2013).

Although both NASA and the U.S. defense industry have shown with experimental aircraft such as the X-29 that it is possible to counteract wing twisting without excessive weight penalty by means of Aeroelastic Tailoring (Gibbs 2017), this innovative method has hardly been applied in the development of sailplanes yet. The best known example where it could be still successfully carried out in order to improve the aerodynamic efficiency is the open class sailplane *Concordia*, illustrated in figure 2.10.



Figure 2.10: CAD rendering of the open class sailplane *Concordia* (Butler 2011).

As figure 2.11 indicates, with conventional layup the wing tip of this sailplane would have experienced an upward twist of 0.4° during cruise flight at design speed. This would have resulted in an undesirable lift distribution due to the increased incident angles in the outer wing area and could be eliminated by a suitable wing layup design.

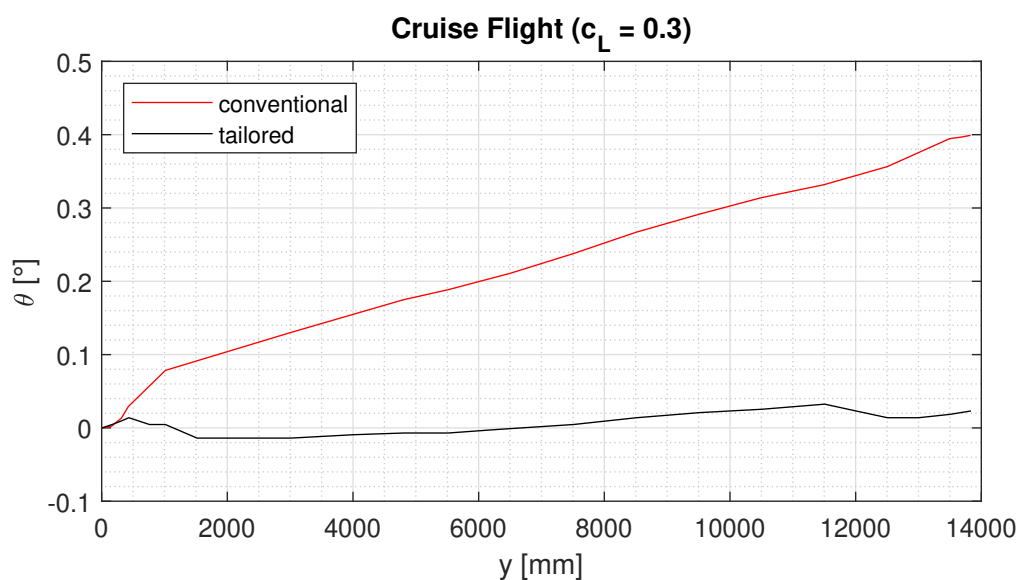


Figure 2.11: *Concordia* wing twist under conventional lamination scheme and applying Aeroelastic Tailoring during cruise flight. Reconstructed from (Butler 2011).

However, since Aeroelastic Tailoring represents a compromise between distinct load cases, the negative twist of *Concordia* increased during thermaling flight according to figure 2.12.

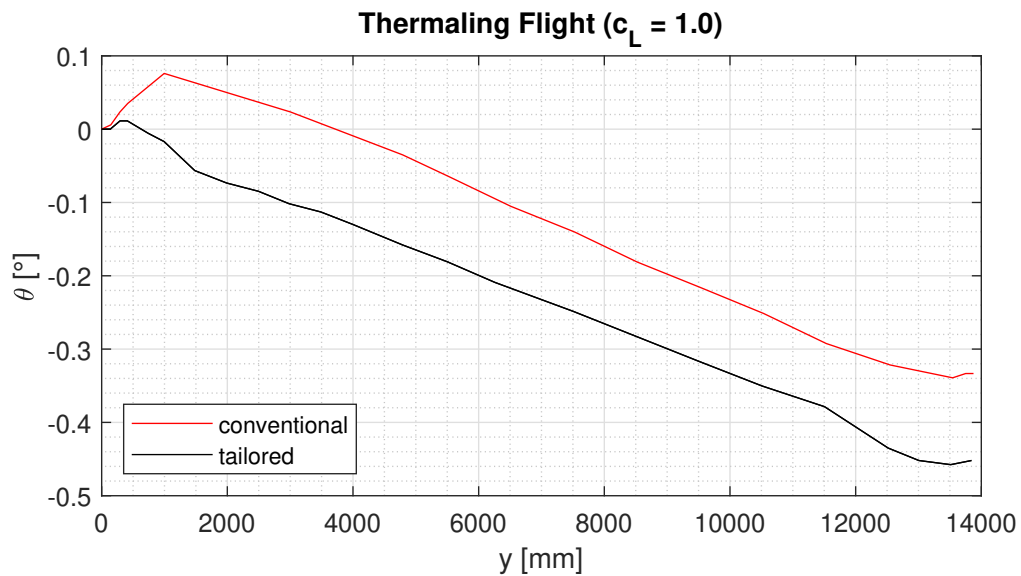


Figure 2.12: *Concordia* wing twist under conventional lamination scheme and applying Aeroelastic Tailoring during thermaling flight. Reconstructed from (Butler 2011).

The general design goal is to keep the amount of twist as small as possible within the entire flight envelope, which can be achieved by a high torsional stiffness of the wing. Aeroelastic Tailoring, moreover, is suitable for sailplanes to optimize the aerodynamic efficiency at a designated load case.

2.3 Finite Element Method

The Finite Element Method (FEM) has been developing into a powerful instrument over the last decades and is applicable in a wide range of engineering problems, which can be described by partial location- and time-dependent differential equations. Improved computer performance nowadays enables analyses of very complex models within a relative short time (Kress 2004). Calculus and solving of huge equation systems are done by computers in a numerical approach, whereas the user of FEM implements the model to be analyzed and evaluates calculated solutions. This chapter briefly describes the background of linear static structural analysis by applying FEM as it is done in this thesis.

The mathematical model of a structure is described by a stiffness matrix. In order to do so, the structure needs to be discretized into small, so called finite elements. For each of these elements, more precisely for all nodes of each element, the relationship between forces $f_{element}$ and deformations $u_{element}$ is known according to equation 2.22, which is information

stored in element stiffness matrices $k_{element}$. These are later summed up to a global stiffness matrix K_{global} that has to be solved numerically (Baier 2011).

$$f_{element} = k_{element} u_{element} \quad (2.22)$$

There exists a huge number of element types. Some commonly used, including those in this thesis, are listed in figure 2.13.


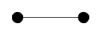
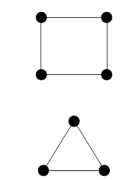
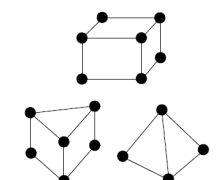

Category	Spring Elements	Line Elements	Surface Elements	Solid Elements	Rigid Elements
Physical Behavior	Simple Spring	Rod, Bar, Beam	Membrane, Thin Plate	Thick Plate, Brick	Rigid Bar
MSC Nastran Element Name	CELAS2*	CONROD* CROD CBAR	CQUAD4 CTRIA3	CHEXA CPENTA CTETRA	RBE2*
Associated Property Entry	None Required	PROD PBAR	PSHELL	PSOLID	None Required
					
* A separate property entry is not required – it is built directly into the element entry.					

Figure 2.13: Basic element types in NASTRAN (MSC 2016a).

The fundamental steps of numerical structural analysis by means of FEM software are:

1) Pre-Processing

At first the user translates a geometrical model of the structure to be analyzed into a discretized model of finite elements. The implementation of element stiffness matrices that build up a global stiffness matrix and the definition of material parameters, loading and boundary conditions are done during the preparation for calculus. It has to be pointed out that model preparation is an abstraction of the reality and the model only should be as simple as possible and as detailed as necessary.

2) Solving

During this step, the solver (FEM software) creates a results database by solving a linear equation system for displacements. Thus strains and stresses can be calculated under consideration of material laws and geometric constraints.

3) Post-Processing

Finally, calculated results can be evaluated and visualized. Users have to be careful when interpreting the results and critically question their physical plausibility.

2.4 Doublet Lattice Method

The Doublet Lattice Method (DLM) is based on the aerodynamic potential theory, where singularities like sources, vortices or doublets are superimposed with the undisturbed free stream. It is an extension of the unsteady subsonic lifting line theory and was first introduced in 1969 (Albano & Rodden 1969).

The discretization of an aerodynamic surface is achieved by splitting it into smaller strips (panels) parallel to the free stream. These panels again are divided into a specified number of discrete trapezoids (boxes), such that the bounding lines of the original aerodynamic surface and the control surfaces coincide with the bounding lines of the resulting boxes (Schwochow 2012). The lateral edges of the boxes are parallel to the free stream. Each box comprises a control point for a flow tangency reference at $\frac{1}{4}$ and a point for the pressure evaluation at $\frac{3}{4}$ of element depth in free stream direction and half span. The $\frac{1}{4}$ -chord line of each box contains a distributed acceleration potential doublet of uniform strength, describing the bound segment of a horseshoe vortex (Albano & Rodden 1969).

The division of an aerodynamic surface into a mesh of boxes can be seen in figure 2.14.

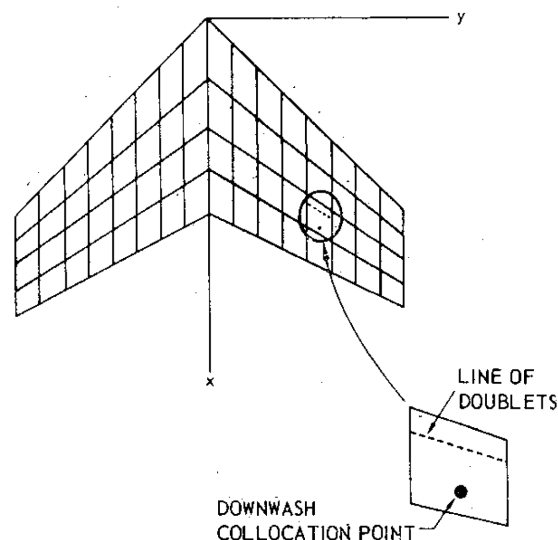


Figure 2.14: Aerodynamic surface, discretized into boxes for the DLM application (Albano & Rodden 1969).

The DLM calculates the surface pressure p_j in each box j as a function of the free stream conditions. It relates the surface pressure, which is assumed to be constant in each box, to the local angle of attack with respect to the free stream velocity vector. This angle is denoted as the non-dimensional downwash w_j . The surface pressure in each box is influenced by the downwashes of all surrounding vortices. An expression relating the local pressure to the local downwash under steady free stream conditions, described by a global dynamic pressure q , is the aerodynamic influence matrix AIC :

$$\mathbf{w}_j = \frac{1}{q} \mathbf{AIC}_{jj} p_j \quad (2.23)$$

The local downwash w_j can be subdivided into two components: A purely geometric part w_j^g and a part that results from the spatial displacement of the aerodynamic mesh \mathbf{u}_a under steady flow conditions. The matrix D_{ja} relates this displacement to the induced part, so the total downwash in each box can be described by the sum of both components:

$$\mathbf{w}_j = D_{ja} \mathbf{u}_a + \mathbf{w}_j^g \quad (2.24)$$

Another matrix S_{aj} integrating over the box surface area leads to the local force \mathbf{f}_a :

$$\mathbf{f}_a = S_{aj} p_j \quad (2.25)$$

Combining equation (2.23) and (2.24) and inserting into equation (2.25) leads to an expression that directly relates the box force \mathbf{f}_a to the box displacement \mathbf{u}_a :

$$\mathbf{f}_a = q S_{aj} \mathbf{AIC}_{jj}^{-1} D_{ja} \mathbf{u}_a + q S_{aj} \mathbf{AIC}_{jj}^{-1} \mathbf{w}_j^g \quad (2.26)$$

In order to achieve a coupled expression, aerodynamic displacements \mathbf{u}_j are related to structural deformations \mathbf{u}_s via the matrix \mathbf{H}_{as} . The transposed matrix \mathbf{H}_{sa} transforms aerodynamic forces \mathbf{f}_a into aeroelastic structural forces \mathbf{f}_s^A :

$$\mathbf{u}_a = \mathbf{H}_{as} \mathbf{u}_s \quad (2.27)$$

$$\mathbf{f}_s^A = \mathbf{H}_{sa} \mathbf{f}_a \quad (2.28)$$

Replacing aerodynamic displacements \mathbf{u}_a and forces \mathbf{f}_a in equation (2.26) by equation (2.27) and (2.28) leads to the following expression:

$$\mathbf{f}_s^A = q \mathbf{K}^A \mathbf{u}_s + q \mathbf{f}_s^{Ag} \quad (2.29)$$

with

$$\mathbf{K}^A = \mathbf{H}_{sa} \mathbf{S}_{aj} \mathbf{AIC}_{jj}^{-1} \mathbf{D}_{ja} \mathbf{H}_{as} \quad (2.30)$$

$$\mathbf{f}_s^{Ag} = \mathbf{H}_{sa} \mathbf{S}_{aj} \mathbf{AIC}_{jj}^{-1} \mathbf{w}_j^g \quad (2.31)$$

\mathbf{K}^A is denoted as the aerodynamic stiffness matrix coupling aerodynamic forces with structural displacements.

The static equilibrium, i.e. the steady state without the presence of inertial forces, can be characterized by:

$$\mathbf{K} \mathbf{u}_s = \mathbf{f}_s^A + \mathbf{f}_e \quad (2.32)$$

with \mathbf{K} to be the structural stiffness, \mathbf{f}_s^A the aeroelastic forces and \mathbf{f}_e external forces, e.g. gravitation. Inserting equation (2.29) into equation (2.32) leads to an expression for the structural displacement \mathbf{u}_s :

$$\mathbf{K} \mathbf{u}_s = q \mathbf{K}^A \mathbf{u}_s + q \mathbf{f}_s^{Ag} + \mathbf{f}_e \quad (2.33)$$

$$(\mathbf{K} - q \mathbf{K}^A) \mathbf{u}_s = q \mathbf{f}_s^{Ag} + \mathbf{f}_e \quad (2.34)$$

The presented set of equations represents the coupling of a structural and aerodynamic system and is to be solved for the static equilibrium as depicted in equation (2.32) (Dillinger 2014).

3 Simulation Model Generation

3.1 Workflow

In this chapter the overall workflow comprising all development steps before starting the aero-elastic simulation in NASTRAN is briefly outlined. Figure 3.1 shows the general development sequence including all input and output data as well as the programs generated in this thesis.

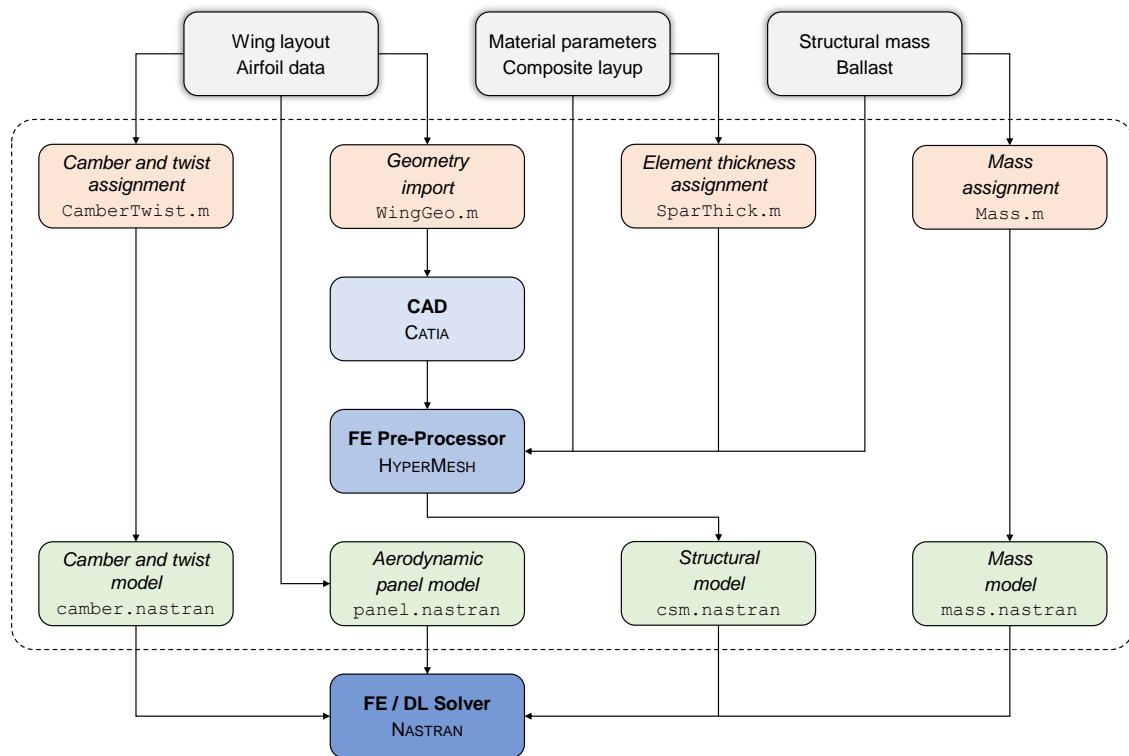


Figure 3.1: Schematic representation of the workflow for the simulation model generation.

A preliminary design provides the required input data for the model generation. These are in particular the wing planform and airfoil data (designed at TUM), selected material parameters and a designated composite layup as well as information about masses and their distribution (from a project partner). CAD work is done by means of CATIA to prepare for the FE model development, which is carried out in HYPERMESH. Programs coded in MATLAB process the input data and support the user wherever the manual implementation of model parameters would be excessively time-consuming and prone to errors. The simulation model is divided into several sub models that serve as input for NASTRAN. In particular, these are a structural FE model (`csm.nastran`) including an interface to an aerodynamic DL model (`panel.nastran`, `camber.nastran`) as well as a mass model (`mass.nastran`).

3.2 Geometry Model

3.2.1 Data Import

In a first step, a geometrical representation of all load carrying structural wing components needs to be created. As the structure is made out of very thin composites, a shell model seems to be an appropriate abstraction. The Generative Shape Design module of CATIA allows fast model generation. Preliminary studies in the MILAN project yield an aerodynamically optimized wing planform as well as different airfoils, which can be seen in figure 3.2:

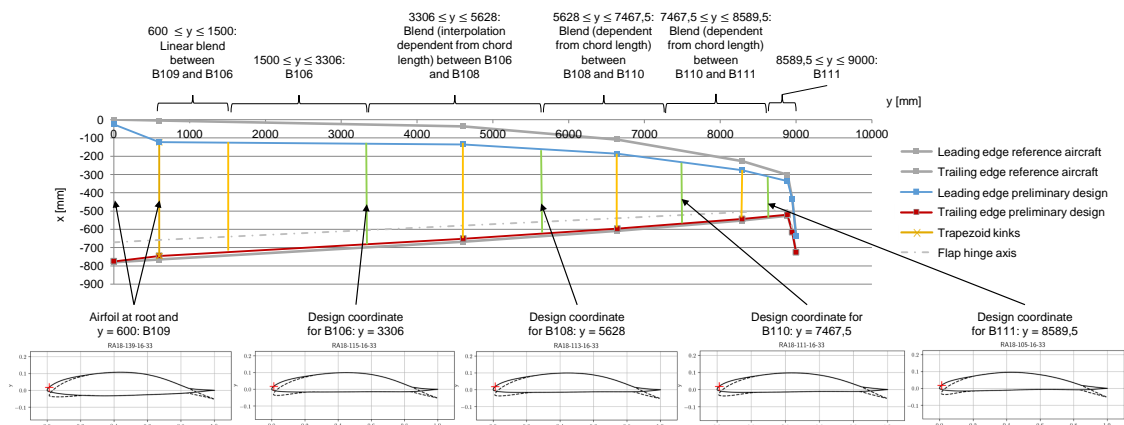


Figure 3.2: Wing planform with according airfoils used for model generation from preliminary studies.

All coordinate values in small letters, if not explicitly stated, refer to the coordinate system (xyz) of the wing that has its origin 110 mm above and 1970 mm behind the global aircraft coordinate system (XYZ). Capital letters refer to the aircraft coordinate system. The origin of the wing coordinate system is defined as the intersection of the leading edge of the wing with the fuselage at $|y| = 300$ mm, projected into the XZ -plane of symmetry.

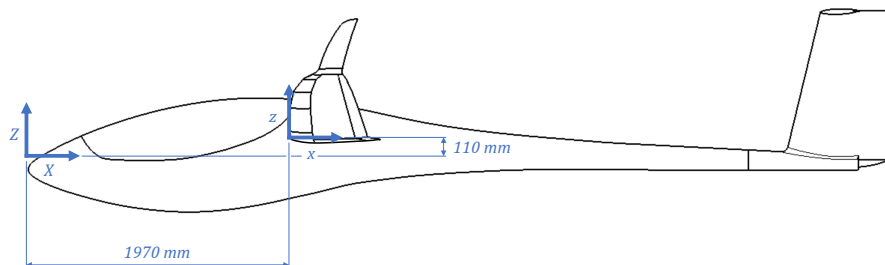


Figure 3.3: Definition of coordinate systems.

Information about the wing planform and the airfoils are stored in a table. This is loaded by the MATLAB program `WingGeo.m`, which is extended for this thesis in order to calculate point coordinates and splines of the wing. There is also information about the location of primary structure elements, in particular the position of the spar and the c web. The output of `WingGeo.m` then is loaded into CATIA.

3.2.2 Geometry Design

The geometry model is built up in several steps. First, the imported airfoil splines together with the leading and trailing edge are used to create an aerodynamic shell. Each trapezoid is represented by one loft. The winglet is omitted as it does not belong to the load carrying structure. Second, the lines representing the positions of the spar cap and the c web are used to extrude surfaces in airfoil thickness direction. In chordwise direction, the first surface stands for the morphing joint, the second and fourth represent the front and rear position of the spar cap, the third the spar web, the fifth the location of the backwards opened c web and the last the flap joint.

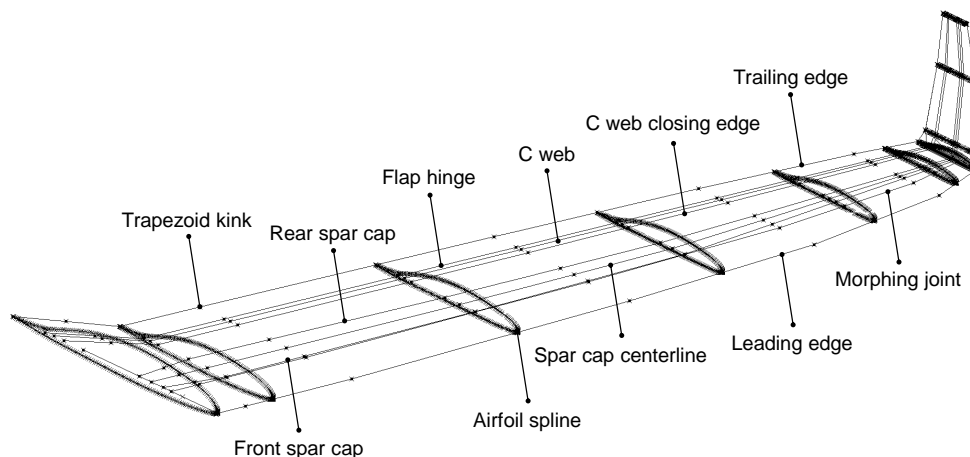


Figure 3.4: CAD imported geometry data.

The spar web is determined to be located at 25% of the spar cap width over a large span range. Towards the wing tip it coincides with the spar cap front. This decision is made in order to enlarge the torsional cross section of the outer wing since the major proportion of twist is assumed to be in this area. The extruded surfaces cut the aerodynamic shape and thus create clearly defined domains. The trailing edge flap is not considered to carry load and therefore not further modeled.

Special attention is to put on the cutouts of the airbrake box and the control ducts. These have a huge influence on the structural design and have to be considered (Schlothauer 2016). In particular the airbrake design represents a challenge in the development due to the rear position of the spar cap. The location of the airbrake ranges from $2346 \text{ mm} \leq |y| \leq 3589 \text{ mm}$. The box being opened towards the top is modeled as an extruded rectangle, connecting upper and lower shell. The ducts cut the upper shell and lace up the c web at $|y| = 2000 \text{ mm}$ and $|y| = 5300 \text{ mm}$ in order to guarantee space for the control rods.

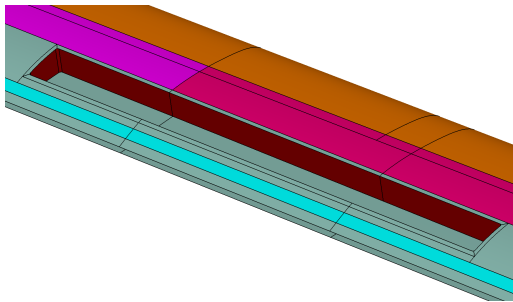


Figure 3.5: Interrupted upper shell for the integration of an airbrake box.

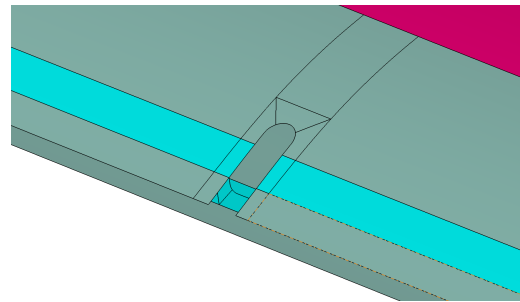


Figure 3.6: Cut upper shell and c web for the integration of control rod ducts.

The compliant mechanisms that actuate the morphing forward wing section also affect the load carrying structure. In order to guarantee a realistic load transfer they need to be modeled. This is realized by chordwise extruded surfaces. The resulting ribs are connected to the morphing skin and the spar web in a spanwise distance of 500 mm to each other. The lower shell is opened between the morphing skin and the spar cap. Despite the continuous transition on the upper side the ribs are the only elements that connect the comparatively low stiff morphing skin with the load carrying structure, i.e. the wing box.

The shell is cut at $|y| = 300 \text{ mm}$, i.e. the half width of the fuselage, in order to realize a root rib that closes the aerodynamic shape to introduce shear loads into the fuselage, which will be described in chapter 3.3 in detail. The spar web splits up into two extruded surfaces and forms, together with the spar cap, a box-shaped root spar tongue that ends in the xz -plane as illustrated in figure 3.7.

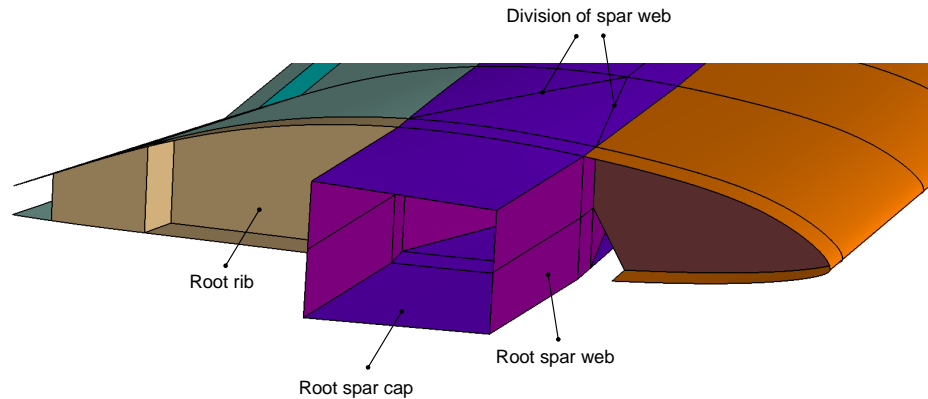


Figure 3.7: Wing root geometry.

3.2.3 Geometry Manipulation

In a last step before the generation of a FE model the surfaces of the created geometry are manipulated and prepared for meshing. Due to layup diversity the wing surfaces need to be partitioned into single domains, each assigned a different property, which will be described in chapter 3.3 in detail.

In order to guarantee a proper mesh, each time the layup of a single component changes in span direction, the whole wing is cut at this point in chordwise direction. First, the wing is separated at $|y| = 5628$ mm, where the shell design changes from a monolithic to a sandwich layup. This point results from a slight shift of the real cut point at $|y| = 5600$ mm to the design coordinate of the airfoil *B108* (see figure 3.2), such that the geometry edges of both coincide. This is to avoid narrow strips and small elements. The spar web layup results in further partitions at $|y| = 2700, 4000, 4800, 6000, 6500, 7200$ and 7800 mm, whereas jumps in the spar cap thickness distribution lead to cut points at $|y| = 1450, 3305, 4400$ and 5628 mm. Again, some coordinates are slightly shifted, in particular the latter, such that geometry edges being close to each other coincide. The compliant mechanisms cut the attached morphing skin as well as the spar web and the front area of the spar cap. In the area of the airbrake box and the control rod ducts surrounding edges are added to achieve a local finer mesh and thus avoid stress singularities (see figure 3.5 and 3.6). All other partitions result from either airfoil edges or trapezoid kinks. The final manipulated and prepared geometry model can be seen in figure 3.8.

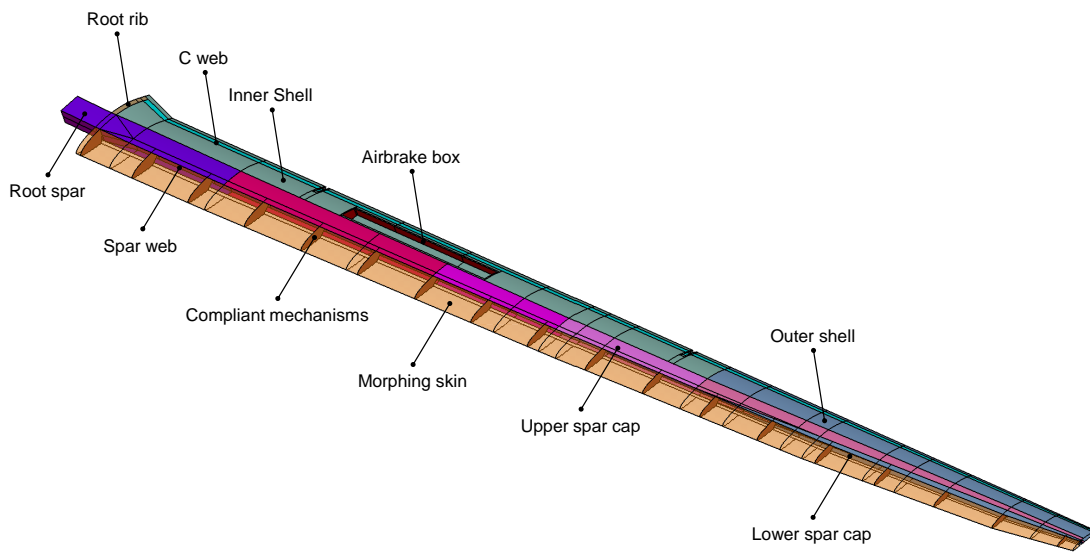


Figure 3.8: CAD shell model with all components.

The geometry model now is well prepared for the creation of a FE model. It has to be mentioned that proper CAD design and some geometric abstractions replace costly and time-consuming geometry cleanup in further steps.

3.3 Finite Element Model

3.3.1 Material Parameters and Layup

The output of any structural analysis strongly depends on the selection of the material parameters. Therefore, it is important to have sufficient knowledge of the stiffness and strength values of the used materials at an early stage of development. The material parameters used in this thesis are predominantly taken from preliminary studies in order to be able appropriately compare the simulation results. It should be pointed out that prior to the final development step, especially when applying Aeroelastic Tailoring, precise knowledge of material values at component level is indispensable. A list of the material parameters that are used to build a FE model can be found in tables 3.1 and 3.2.

Table 3.1: Available input data for anisotropic materials.

ID	Name	Description	E_x [MPa]	E_y [MPa]	G_{xy} [MPa]	ν_{xy} [-]
1	G E 90070 ^a	GF weave lamina	16 200	16 200	3700	0.05
2	C HM 98151 ^b	CF weave lamina	91 820	91 820	19 500	0.05
3	C HM 98141 ^b	CF weave lamina	91 820	91 820	19 500	0.05
4	C HT Roving ^a	CF roving	77 000	3400	2870	0.28
5	C HT T300 ^c	CF UD prepreg	110 438	7099	3516	0.34
8	Innegra S ^d	CF laminate	37 334	5151	2719	0.45

^a Values from (Kickert 1988).

^b Values from a project partner.

^c Values from the Institute of Lightweight Structures (TUM).

^d Monolithic composite of carbon and glass fibers provided by *Innegra Technologies*.

Table 3.2: Available input data for isotropic materials.

ID	Name	Description	E [MPa]	ν [-]
6	PEEK ^a	Thermoplastic polymer	4232	0.36
7	Divinycell H60 ^b	Sandwich foam	70	0.75

^a Values from (Salehar 2015).

^b Values from (Diab 2018).

Polyether ether ketone (PEEK) is used for the compliant mechanisms. These are modeled as flat ribs with isotropic properties. Since the real mechanisms will be strongly anisotropic, a correspondingly lower replacement stiffness must be chosen for the global consideration of the structural model. For the calculation of this replacement stiffness, a proportional relationship between the Young's modulus and the volume of a rib is assumed in a first approximation. Assuming that the volume of a topology-optimized rib is filled with material to 12.5 %, this proportion is also used for the stiffness that contributes to the deformation behavior of a compliant mechanism. Therefore, the Young's modulus for PEEK is corrected to be $E = 529$ MPa in the material database of the FE model. Sandwich foam is used within the outer wing shell and the spar web.

The morphing skin is modeled as monolithic shell laminate with *Innegra* fibers. The T300 prepreg fiber is used wherever the structure is reinforced. This concerns in particular the areas of load introduction in the root rib area. Carbon fiber (CF) rovings form the spar cap due to their high longitudinal tensile stiffness. The two listed high modulus (HM) carbon lamina,

covering the wing box shell as well as the spar web and the c web, differ in the areal weight of the corresponding textile respectively. This results in different ply thicknesses when combining the textiles with a matrix during the manufacturing process as illustrated in figure 3.9.

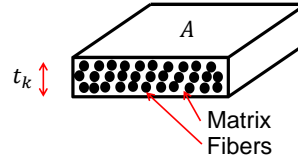


Figure 3.9: Cross section of a UD composite ply (Drechsler et al. 2017).

Equation (3.1) provides a direct expression for the thickness t_k of a single cured composite ply in terms of the areal weight $\frac{m_F}{A}$ of the textile and the fiber density ρ_F as well as the fiber volume content φ_F :

$$t_k = \left(\frac{m_F}{A} \right) \frac{1}{\rho_F \varphi_F} \quad (3.1)$$

The importance of knowing these values is due to the fact, that the bending stiffness of a laminate or sandwich strongly depends on the its cross sectional second moment of area.

Table 3.3: Physical properties of fibers and matrix and resulting ply thicknesses.

Name	ρ_F [t/mm ³]	$\frac{m_F}{A}$ [t/mm ²]	ρ_M [t/mm ³]	φ_F [-]	t_k [mm]
G E 90070	2.55×10^{-9}	8.00×10^{-11}	1.20×10^{-9}	0.35	0.090 ^a
C HM 98151	1.80×10^{-9}	2.45×10^{-10}	1.20×10^{-9}	0.5	0.272 ^a
C HM 98141	1.80×10^{-9}	2.00×10^{-10}	1.20×10^{-9}	0.5	0.222 ^a
C HT T300	1.77×10^{-9}	2.80×10^{-10}	1.20×10^{-9}	0.5	0.316 ^a

^a Derived from other values.

In the areas where the shell and the spar cap overlap, the corresponding thicknesses are added. The same applies to the rear wing section where the shell overlaps with the c web. The thickness values for the spar cap vary along the wing span and are derived in chapter 3.3.2.

Due to the complexity of the FE model, the list of layups in this thesis is limited to the main structural elements. For the detailed construction of the individual components, especially the reinforced areas near the wing root, reference is made to `csm.nastran`. The layups for the essential components, i.e. the morphing forward wing section and the wing box are:

- **Morphing skin** (monolithic)

- layup orientation: 0°
- material ID: 8
- layup thickness: $T_{morphing\ skin} = 2.258\text{ mm}$

- **Inner shell**

- ply orientations: $(0^\circ, 45^\circ, 45^\circ, 45^\circ, 45^\circ, 45^\circ, 45^\circ)$
- material IDs: $(1, 2, 2, 2, 2, 2, 2)$
- layup thickness: $T_{inner\ shell} = 1.722\text{ mm}$

- **Outer shell**

- ply orientations: $(0^\circ, 45^\circ, 45^\circ, [2\text{ mm core}], 45^\circ)$
- material IDs: $(1, 3, 3, 7, 3)$
- layup thickness: $T_{outer\ shell} = 2.756\text{ mm}$

- **Spar web** (at wing root)

- ply orientations: $(45^\circ, 45^\circ, 45^\circ, 45^\circ, 45^\circ, [8\text{ mm core}], 45^\circ, 45^\circ, 45^\circ, 45^\circ)$
- material IDs: $(2, 2, 2, 2, 2, 7, 2, 2, 2, 2)$
- layup thickness: $T_{spar\ web, root} = 10.45\text{ mm}$

- **C web**

- ply orientations: $(45^\circ, 45^\circ, 45^\circ, 45^\circ)$
- material IDs: $(3, 3, 3, 3)$
- layup thickness: $T_{c\ web} = 0.888\text{ mm}$

Hereby, for each component, the stacking sequence is directed inwards starting from the aerodynamic shell. The stacking sequence of the spar web is defined in positive x -direction. Ply orientation angles refer to the local spar axis. Layup thicknesses T_{layup} are calculated by:

$$T_{layup} = \sum_{k=1}^n t_k \quad (3.2)$$

where t_k are the single ply thicknesses from equation 3.1.

3.3.2 Wing Structure Model

Having designed an abstracted shell model as described in chapter 3.2, the geometry, i.e. the split surfaces, are imported in the pre-processor `HYPERMESH`, which is known as very powerful application for preparing FE analysis. `HYPERMESH` is compatible with many FE solvers and translates structural information into a list of commands in the desired, user specified solver language. This is set to be `NASTRAN`, such that the output file of `HYPERMESH` contains commands, traditionally denoted as *cards*, that can be further included in the `NASTRAN BULK` data section. `HYPERMESH` automatically recognizes pre-assigned surface sections from CAD and creates corresponding components. The geometry edge edit tool automatically merges equivalent edges by a user specified tolerance, such that elements of adjacent surfaces share the same edges when a mesh is generated. Having a meticulously designed geometry, this tolerance can be set to a small value and no connection errors appear.

The shell element connections employed for the discretization of the surfaces are quadrilateral `CQUAD4` and triangular `CTRIA3` (MSC 2016b), where the latter is applied predominately in areas where triangular surfaces taper at one end. The seeding size of 10 mm leads to 80 052 elements, where the element node spacing becomes narrower towards the leading edge in order to match with the nose radius.

Element characteristics are described by properties. Each component with its characteristic layup is assigned to a different property. One possibility to define composite stiffness properties in `NASTRAN` shell elements is the specification of a stacking sequence by means of `PCOMP` property cards. `PCOMP` allows to define the thickness, orientation and material of each composite ply. The compliant mechanisms are assigned to the general shell element property card `PSHELL` that can be used for non-stacked materials and besides mechanical parameters defines a shell thickness.

Orthotropic material parameters are specified in `MAT8` cards, including among others the in-plane Young's moduli E_1 and E_2 , the Poisson's ratio ν_{12} as well as in-plane and transverse shear moduli G_{12} , G_{1Z} and G_{2Z} . Unspecified material parameters such as the transverse shear moduli are assumed to be infinite. This has a negligible effect on the deformation behavior of the structure under the assumption of plane stress, which can be made for thin composites (Drechsler & Hartmann 2017). Simulations with arbitrary values for the transverse shear moduli prove this assumption. Isotropic materials are defined with `MAT1` property cards.

Particularly challenging is the implementation of a varying spar cap thickness in span direction. One possible solution is to address single elements and assign specific thickness values to them. As the elements covering the spar cap surfaces sum up to 15 920, this cannot be done manually. Therefore, a MATLAB written interface denoted as `SparThick.m` calls the concerned elements by their ID number, more precisely the corner nodes of the elements, and evaluates their y -coordinates. By means of this information, the local spar cap thickness is determined by linear interpolation between predefined supporting point thicknesses $t_{spar,i}$ for each element with:

$$t_{spar,i} = n_{roving,i} \frac{A_{roving,i}}{w_{spar,i}} \quad (3.3)$$

where $n_{roving,i}$ denotes the number of rovings at any supporting point i with cross sectional area $A_{roving,i}$ and spar width $w_{spar,i}$. The thickness distribution for the upper and the lower spar cap is shown in figure 3.10.

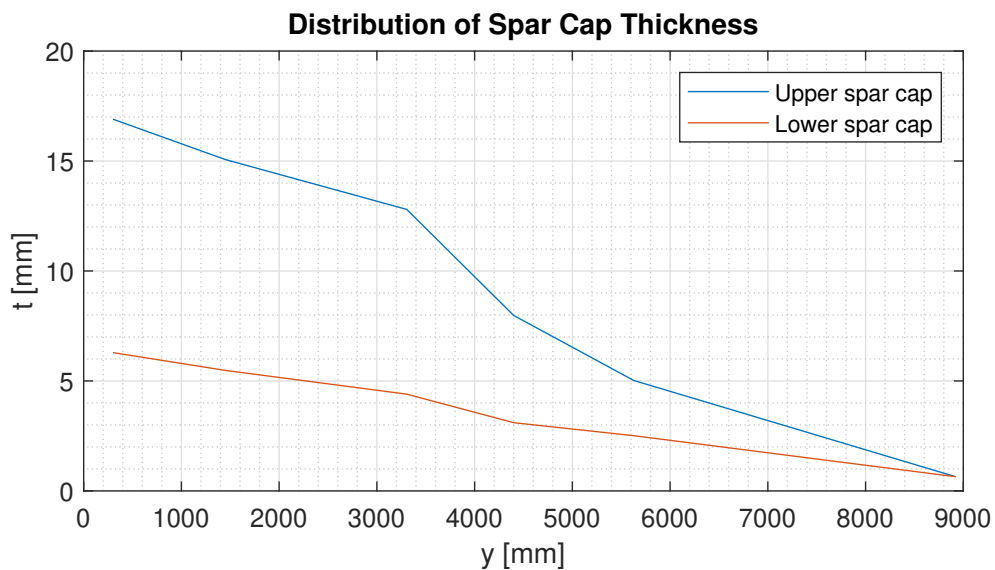


Figure 3.10: Thickness distribution for the upper and the lower spar cap from a preliminary structural design by a project partner.

The design of the spar cap differs significantly from a conventional, symmetrical design. Due to the much lower values for compressive strength compared to the tensile strength of the rovings, the lower spar cap can be dimensioned thinner than the upper spar cap.

As all composite layups have anisotropic characteristics, the elements have to be oriented correctly. In order to do so, a local coordinate system is created at each position where the spar is kinking. The local element x -axes (to be distinguished from the wing x -axis), i.e. the 0° -directions acting as reference for ply orientations, are aligned with the spar. Element normals point towards the interior of the wing and have 0 mm offset to the geometry surfaces. Thus the stacking sequences that strongly influence cross sectional bending stiffnesses may be displayed adequately.

Figure 3.11 shows the usage of one-dimensional rigid body elements of type RBE2 as actuators for the compliant mechanisms that transfer translations and rotations from the corner of the ribs (not displayed) to the spar web via RBE3 multi-point connections. In order to prevent local buckling of the morphing skin, the opened cross section is closed with normal force joints. These are also modeled as RBE2 elements but allow translations in normal direction. Since both the actuators and the normal force joints add stiffness to the structure, they will affect the deformation behavior of the wing, which will be discussed in chapter 4.2

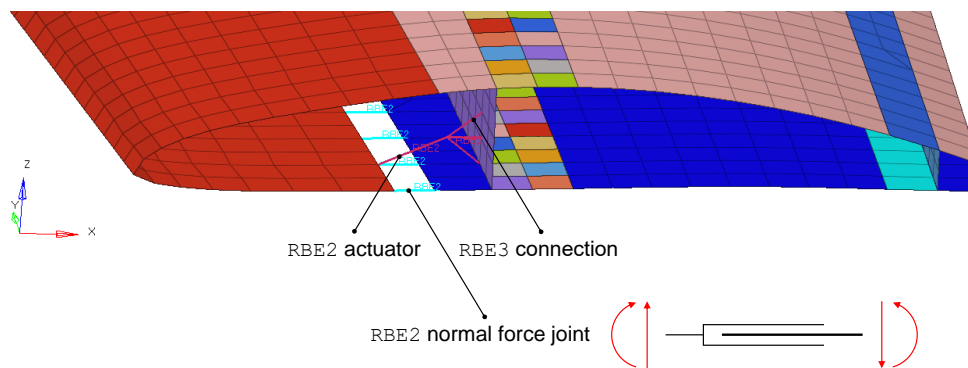


Figure 3.11: RBE2 actuators attach the compliant mechanisms (hidden) to the spar web via RBE3 connections. RBE2 normal force joints close the open wing cross section.

3.3.3 Boundary Conditions

Having defined all property cards, boundary conditions can be set. This is done by single point constraints by means of SPC cards. Forces are carried by shear force bushings integrated in the root web whereas moments are transferred via the spar cap into the opposite wing.

Each shear forces bushing is modeled as RBE3 element, transferring the weighted average of the motions of multiple grid points, i.e. the element nodes where a bushing is located, to another grid point. Only translations are transferred to this reference grid point.

A `RBE2` element then connects the bushing to the fuselage, transferring shear forces. The root spar ends up in the global XZ -plane, where a `SPC` symmetry condition is set, constraining non-symmetrical motions. Thus, only translations in X -direction and in Z -direction, i.e. heaving, as well as pitching around the center of gravity are enabled. The location of the center of gravity will be designated in chapter 3.4.3.

3.3.4 Fuselage and Empennage Model

In order to achieve trimmed flight conditions, the empennage of the sailplane has to be modeled. A fuselage model serves as rigid body connection to the wing structure model. Both, the horizontal stabilizer including the elevator and the fuselage are realized by `RBE2` elements and illustrated in figure 3.15 at the end of this chapter.

3.3.5 Interface Model

Aerodynamic loads and structural deformations are connected with an interface model. `RBE2` elements in chord direction and homogeneously distributed along the span represent the aerodynamic panel. The rigid elements connect the leading edge with the trailing edge of the aerodynamic surface and have additional coupling nodes. Thus, a full coverage of the aerodynamic surface with points that belong to the structural model is achieved. The set of nodes that is used for coupling is defined with a `SET1` card. `RBE3` elements are used to transfer aerodynamic forces from these nodes to shell element grid points and to return averaged structural deformations.

There are two interface models developed in this thesis:

- one for model validation, comprising the entire chord and introducing the aerodynamic forces completely into the wing box, and
- one for the investigation on the influence of the morphing forward wing section, having two separate `RBE2` elements in chord direction and dividing the aerodynamic load between the morphing forward wing section and the wing box.

The results referring to the former configuration, where the morphing forward wing section is omitted, will be treated in chapter 4.1. Figure 3.12 shows the latter, which corresponds to the results described in chapter 4.2.

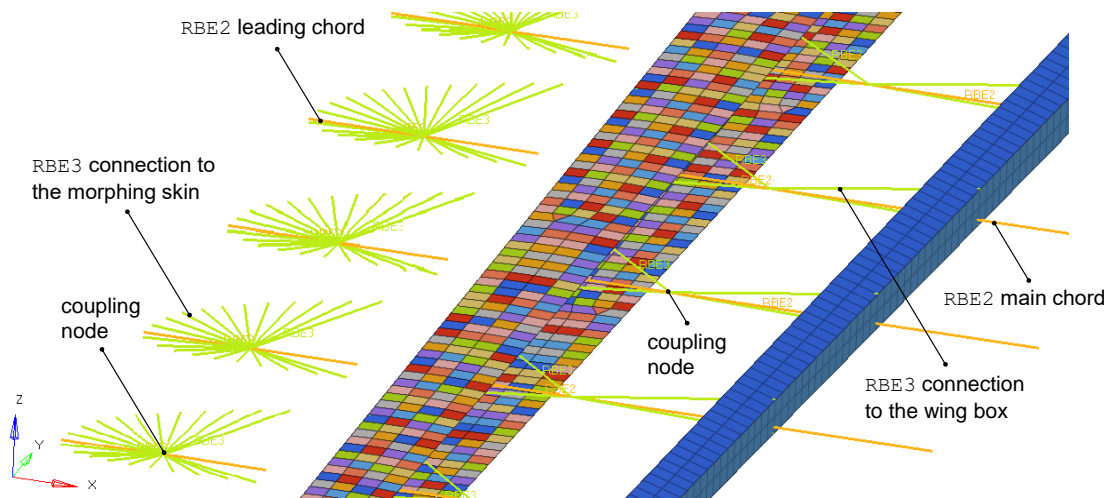


Figure 3.12: Interface model with chordwise RBE2 elements and coupling RBE3 elements for the morphing forward wing section (hidden) and the wing box (only spar and c web displayed).

The mathematical coupling between the aerodynamic and structural model will be described in chapter 3.5.3 more precisely.

3.4 Mass Model

Besides the weighted multi-point connection of specified nodal degrees of freedom, RBE3 elements can also be used for modeling structural parts that do not contribute to the stiffness. This includes masses in front and rear of the load carrying wing box, e.g. water ballast, morphing mechanics and control system.

3.4.1 Structural Mass

The structural mass includes the masses of all components in the FE model. There are two ways to represent the structural mass of the wing. One is to assign densities to the materials. NASTRAN then calculates elementary and homogeneously distributed masses. A disadvantage of this method is that non-modeled components are neglected. Especially adhesions and paint layers are not included in the FE model. In order to also consider non-load-bearing structural components like flaps, ailerons, controls and morphing mechanics, concentrated masses including all mentioned parts are implemented. This is done by discrete masses of type CONM2 from preliminary studies and their predefined focal points. The point masses are attached to the load-carrying wing box with RBE3 multi-point connections and assigned their

values in a separate NASTRAN input file denoted as `mass.nastran`. The targeted structural mass of each wing that results from preliminary studies is $m_{wing}^S = 99$ kg. This value considers the primary structure, the controls as well as the morphing mechanics. A detailed mass distribution is listed in the appendix.

3.4.2 Ballast

In a similar way, the discrete mass points of the wing water ballast located in front of the spar web are attached to the FE model. In order to reach the sailplane's maximum take-off mass (MTOM) $m_{aircraft} = 600$ kg, 51 kg of water has to be filled in per wing. However, it has to be mentioned that due to geometrical reasons only about 40 liters fit into each wing. In this thesis it is assumed that the entire wing ballast mass m_{wing}^B of 51 kg is filled in, starting at the wing root up to $|y| = 4650$ mm for each wing. The water ballast is assigned its own component in HYPERMESH, so that it can be omitted in further simulations to investigate its influence on the aeroelastic behavior of the wing. The total wing mass then calculates to 150 kg by:

$$m_{wing} = m_{wing}^S + m_{wing}^B \quad (3.4)$$

Figure 3.13 indicates the positions of the discrete mass points for the ballast and the structural mass and their RBE3 connection to the primary structure.

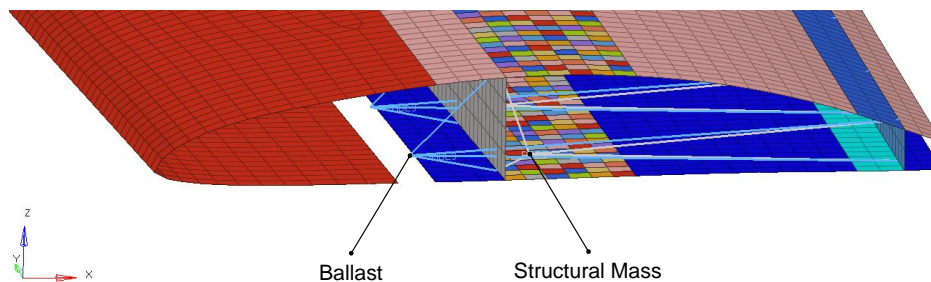


Figure 3.13: Discrete mass grid points and their RBE3 attachment to the wing box.

3.4.3 Center of Gravity

The precise position of the center of gravity of the total aircraft has a considerable influence on the aeroelastic behavior of the wing. This is due to the distribution of lift components on the wings and the horizontal stabilizer. A further forward center of gravity leads to a relative increase in wing lift, as the elevator must increasingly generate downforce to maintain the

aircraft in a trimmed condition. For this reason, in order to achieve the highest possible wing lift, the foremost position is assumed for the model, which is located at $X_{aircraft} = 2107$ mm. This value is taken from a project partner and results from the centers of gravity for the wing and non-lifting parts (NLP), i.e. fuselage and empennage. Both are not known a priori. The former is calculated by NASTRAN to be located at $X_{wing} = 2177$ mm, while the latter is calculated using a moment equilibrium around the aircraft coordinate system origin:

$$X_{NLP} = \frac{m_{aircraft} X_{aircraft} - 2 m_{wing} X_{wing}}{m_{NLP}} \quad (3.5)$$

Inserting the given values into equation (3.5) leads to a center of gravity of the non-lifting parts at $X_{NLP} = 2037$ mm. This value is needed to define the fuselage and empennage mass m_{NLP} as CONM2 point mass in the FE model. Furthermore, the aircraft center of gravity is defined as a node around which rotation is enabled to create a trimmed flight condition during the simulation.

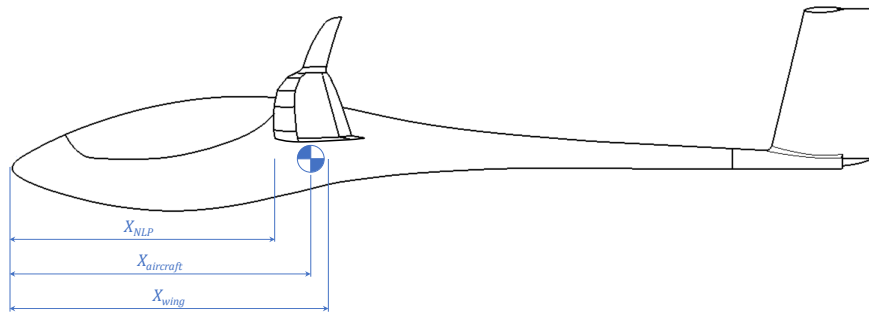


Figure 3.14: Schematic illustration of the lever arms with respect to the aircraft coordinate system for the determination of the centers of gravity.

The values for all masses used in this thesis as well as the locations of their centers of gravity in terms of the defined coordinate systems from figure 3.3 are summarized in table 3.4.

Table 3.4: Masses and corresponding center of gravity locations in MTOM configuration.

Component	Designation	Mass [kg]	X [mm]	x [mm]
Aircraft	$m_{aircraft}$	600	2107	137
Wing	m_{wing}	150	2177	207
NLP	m_{NLP}	300	2037	67

Figure 3.15 shows the finished FE model with all its components including the fuselage and empennage as well as the interface to the aerodynamic model. The solver deck is written within HYPERMESH into a **computational structural mechanics** input file `esm.nastran` for NASTRAN.

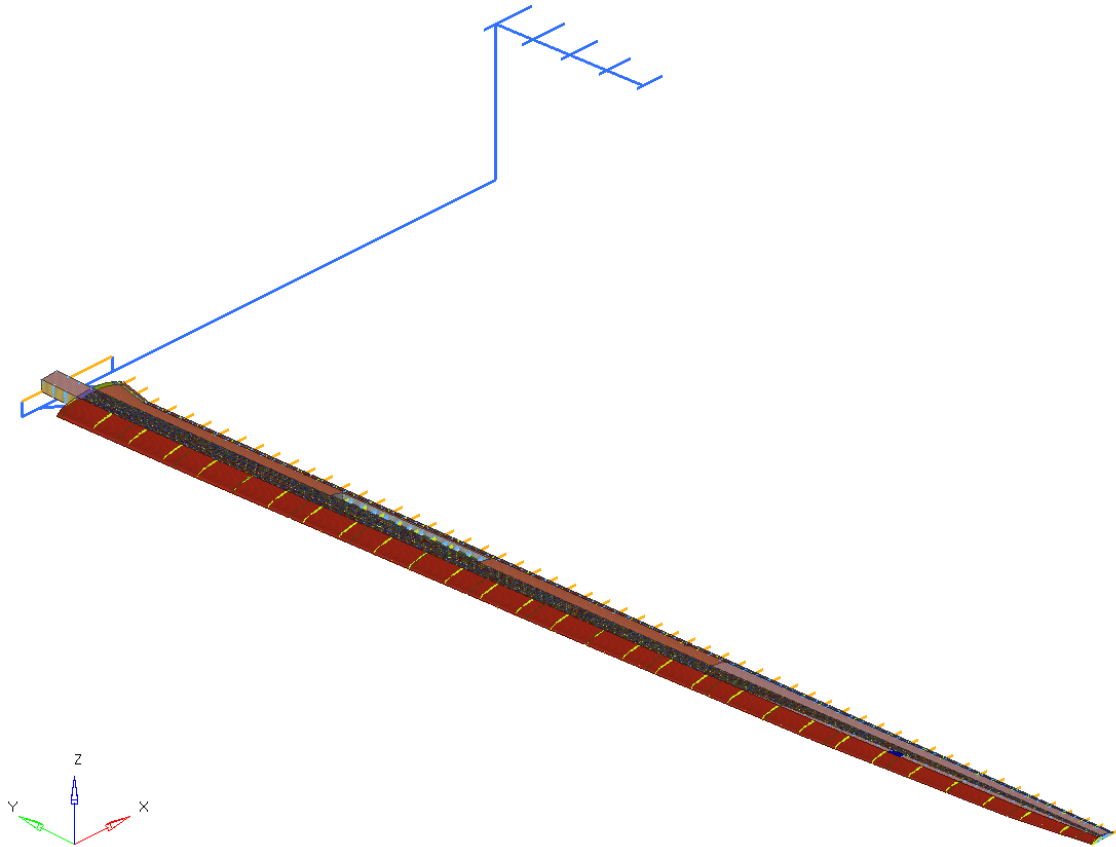


Figure 3.15: FE model with wing including morphing forward wing section, fuselage, empennage and interface.

3.5 Doublet Lattice Model

One reason why aeroelastic simulations are performed with NASTRAN is its provision for aerodynamic tools like DLM that together with the FEM enable coupled calculations. Up to this point, the construction of a structure model and an interface by means of HYPERMESH has been described. However, there is no user interface for building an aerodynamic model. This development step is done manually by coding multiple NASTRAN input files containing information about the wing planform and the airfoils.

3.5.1 Aerodynamic Panel Model

In a first step, the discretized aerodynamic surfaces for the wing and the horizontal stabilizer are defined. This is done by `CAERO1` cards, each defining an aerodynamic macro element, denoted as *panel* in terms of two leading edge locations and side chords (MSC 2016b).

The sequence of box numbering is defined in positive x -direction along the chord and in positive y -direction along the span. Since negative y -values are selected for the wing definition, special attention must be paid to the sequence of box assignments in the code of `panel.nastran`. Figure 3.16 illustrates this process, where n describes the ascending number of leading edge point definitions and N the total number of boxes.

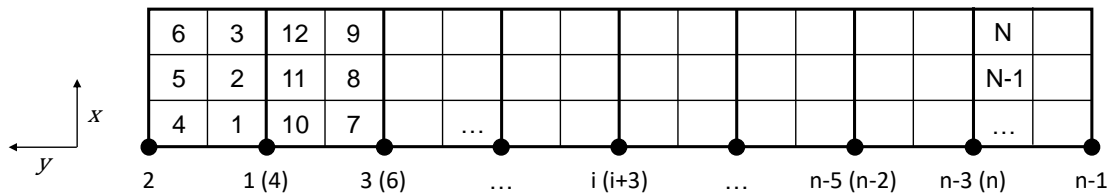


Figure 3.16: Order of box numbering.

Within each panel the number and spacing of boxes can be defined in span and chord direction. Each wing trapezoid is described by its own panel. With the exception of the outermost trapezoid, where the box span widths become smaller with a spacing factor of 0.83 towards the wing tip in order to enable an accurate reproduction of the boundary vortex, the box span widths within all other panels keep constant. Along the entire wing, towards the leading and trailing edge the boxes become closer by a spacing factor of 1.2 in order to map the pressure jumps of adjacent boxes more precisely.

The aerodynamic surface is defined in such a way that its cross section is always parallel to the flow direction. Neither information on the built-in wing twist nor the camber is implemented in the `CAERO1` card. This is equivalent to a non-twisted flat wing by default. The wing dihedral, however, is considered and constant along the entire span. Twist and camber information are modeled as changes of local incident angles as described in chapter 3.5.2.

Control surfaces can be implemented as own panels with the additional definition of a local coordinate system whose y -axis describes the control surface hinge by means of `AESURF` cards. The boxes covering the control surfaces are defined with `AELIST`. Since only symmetrical load cases are to be investigated, the definition of ailerons is not necessary in this thesis.

Therefore, only a deflectable elevator is modeled in order to create trimmed flight conditions. The winglet is neglected, since its influence on the wing tip vortex has only little effect on a first approximation of the global deformation behavior of the wing.

Figure 3.17 shows the finished aerodynamic panel model. The fine mesh at the leading and trailing edge as well as towards the wing tip is clearly visible. The hinge axis of the elevator can also be identified, as the control surface is finer discretized. The DL model comprises in total 3500 boxes for the wing and 225 for the horizontal stabilizer including the elevator.

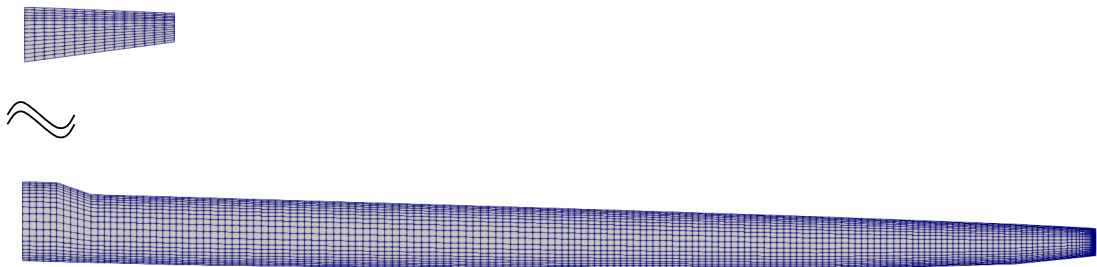


Figure 3.17: Aerodynamic panel model for the wing and the horizontal stabilizer including elevator.

3.5.2 Camber and Twist Correction

By means of a matrix denoted as W_{2GJ} it is possible to perform a rotation of the local downwash angles, representing a cambered airfoil and a twisted wing. In the former case the adaption stands for the angle of the camber line along the chord, while in the latter case it causes wing twisting in span direction, which is illustrated in figure 3.18. Both variants can be changed along the span and thus allow the use of multiple airfoils and the implementation of a geometric twist (Dillinger 2014).

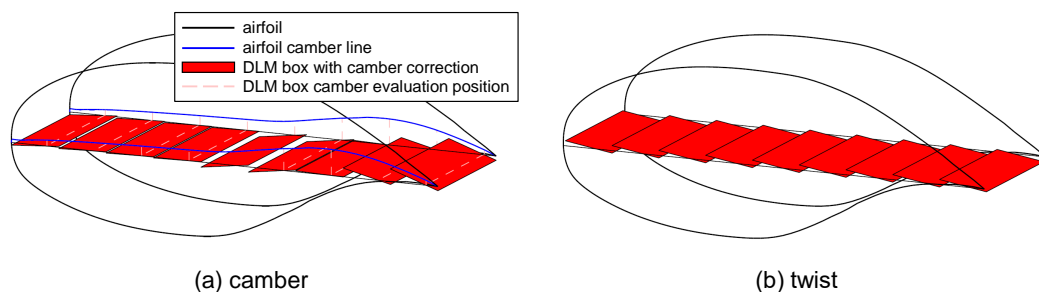


Figure 3.18: Camber (a) and twist (b) correction for a row of DLM boxes in chord direction (Dillinger 2014).

The reason why the aerodynamic panel model is implemented as a composition of plane surfaces with zero angle of attack is that by the subsequent angle correction any camber and twist can be applied, which will be particularly important for the examination of different airfoils. In the same manner as the aerodynamic panel model is created, the application of the `W2GJ` rotation matrix must be implemented code-based within a separate input file `camber.nastran`. This file is created by the `MATLAB` written program `CamberTwist.m`. First, each airfoil is discretized along its chord with the same spacing as the aerodynamic panel. It becomes clear that a finer discretization is necessary towards the leading and trailing edge, since the camber is particularly large there. As described in chapter 2.4, the pressure evaluation of each box is at $\frac{3}{4}$ of its depth in chord direction and half span, denoted as Pistolesi point. This is also the camber evaluation position, exemplary illustrated in figure 3.19.

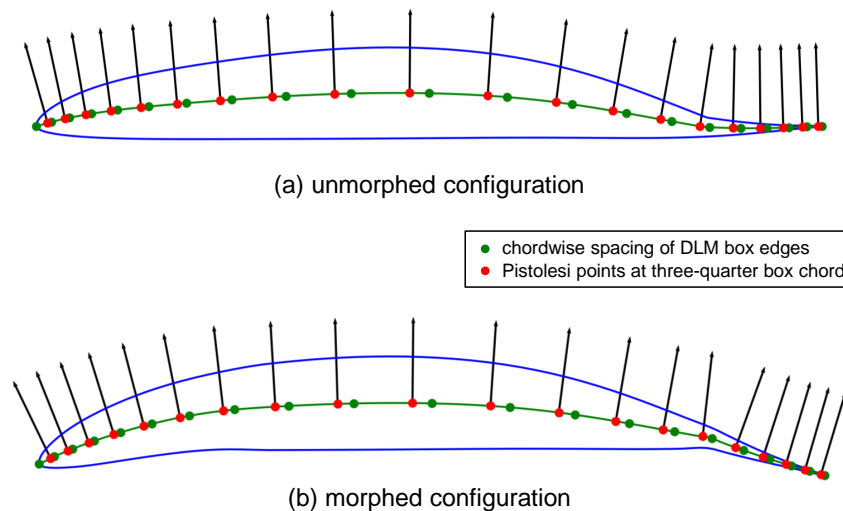


Figure 3.19: Camber evaluation at the Pistolesi points of chordwise DLM boxes in unmorphed (a) and morphed (b) configuration.

At any location where the airfoil changes according to figure 3.2, camber and twist are superimposed to a single value for the angle correction. For all other values in span direction linear interpolation is performed between these supporting points.

There is no user interface to directly verify the implementation of the camber and twist correction. One way to achieve this is to modify the downwash angles at defined span positions in such a way that a significant change in the resulting lift distribution can be seen. This is, for example, the case where the airbrake is located (see chapter 3.2.2). The local lift collapse

induced by the airbrake can be considered in the DL model by a local change of the incident angle, which is equivalent to a `W2GJ` rotation. In this thesis it is assumed that the extended airbrake causes a local change in the angle of attack of -11.5° at all affected boxes.

3.5.3 Coupling

Now that the DL model is complete, it can be coupled with the FE model. `NASTRAN` offers the possibility to transfer aerodynamic forces to structural points, which is called splining, and to return structural deformations to the aerodynamic mesh. More precisely, `SPLINE1` defines a surface spline for interpolating aerodynamic forces on the `CAERO1` panels and transfers them to a defined set of structural grid points. This set consists of the coupling nodes as described in chapter 3.3.5. Thus, the aerodynamic forces are uniformly introduced into the wing box (and into the morphing forward section in the case of an extended wing structure model) and induce structural deformations to be transferred to the aerodynamic model.

4 Design Studies

4.1 Model Validation

4.1.1 Analysis of Influencing Parameters

A model is always an abstraction of reality. It therefore has a large number of parameters that influence simulation results. Geometric simplifications, such as the representation of very thin composite structures by means of shell elements and the neglect of adhesive gaps, are described in chapter 3.2 and represent the first degree of abstraction. There is also a multitude of adjustable parameters in the construction of the structural FE and the aerodynamic DL model as described in chapter 3.3 and 3.5. Some important parameters with a considerable influence on the simulation results are:

- **Material parameters**

In particular the stiffness values and the anisotropy of composites influence the deformation behavior of the wing. These in turn depend on the production. For global considerations the compliant mechanisms are modeled as isotropic ribs with reduced stiffness. These are actually anisotropic, which can affect the torsional stiffness of the morphing forward wing section.

- **Morphing forward wing section**

Despite the open cross section, its integration has a great influence on the deformation behavior of the wing. Especially the attachment to the spar web via normal force joints and the layup of the morphing skin determine the torsional stiffness of the entire wing. Since this section is identified to be the main influencing parameter on the static aeroelasticity, it will be examined extensively in chapter 4.2.2.

- **Shell element thicknesses**

These result from the thickness of the composite layers and have an effect on the second moment of area of the wing cross section and thus on the deformation behavior of the structure. As described in chapter 3.3.2, the composite thickness depends on production parameters such as the achievable fiber volume content.

- **Boundary conditions**

In order to avoid unrealistically high constraining forces, care is taken in the definition of boundary conditions to constrain only as few degrees of freedom as necessary. These are discussed in chapter 3.3.3 and permit rotation of the root rib around the x -axis,

since moments are transmitted to the other wing via the spar cap and transverse forces are transferred to the fuselage via the shear force bushings. This avoids unrealistically high clamping forces, however, it has the effect of increasing deflection, which is accompanied by greater twisting, especially towards the wing tip.

- **Distribution of masses**

The allocation of discrete mass points controls the wing deflection on the one hand, but on the other hand twisting due to the lever arm towards the local shear center. In particular the water ballast placed in front of the spar web counteracts the upward twisting of the wing.

- **Center of gravity**

As described in chapter 3.4.3, the precise determination of the center of gravity in a trimmed flight condition controls the lift division on the wing and the horizontal stabilizer. Lift forces induced by the fuselage are neglected. This leads to a conservative view, since the wing takes over a larger part of the lift.

- **Spacing of boxes**

An insufficient discretization of the aerodynamic panel leads to a non-physical pressure distribution. Therefore, as depicted in chapter 3.5.1 and 3.5.2, a finer mesh is chosen in areas of large airfoil camber and towards the wing tip.

4.1.2 Simulation Preparation

Having generated all input files for the structural, aerodynamic and mass model, they are included within the `BULK` data section of the `SOL144` aeroelastic code. An example code is shown in the appendix. Before running the solution sequence in `NASTRAN`, input values for the dynamic pressure, the Mach number and the vertical acceleration have to be set.

Velocities are indicated in terms of the Equivalent Air Speed (EAS) that is equal to the Calibrated Air Speed (CAS) for low Mach Numbers, since the compressibility of air can be neglected here. EAS does not consider the density decrease with the altitude and always refers to the air density at mean sea level (MSL). The advantage of this is that information on speed, especially values for stall and optimal design speed, are independent of the altitude.

Main data of the International Civil Aviation Organization (ICAO) Standard Atmosphere (ISA) are provided in table 4.1. Any value for the dynamic pressure in this thesis is calculated with the standard air density ρ_0 and the corresponding equivalent air speed V_{EAS} .

Table 4.1: Selected values of the ISA, related to MSL (ICAO 1976).

Air Temperature	T_0	288.15 K
Air Pressure	p_0	1013.25 hPa
Air Density	ρ_0	1.225 kg/m ³

The Mach number Ma is defined as the ratio between the velocity V and the speed of sound a and provides information about the compressibility of air:

$$Ma = \frac{V}{a} \quad (4.1)$$

where

$$a = \sqrt{\kappa \frac{p_{air}}{\rho_{air}}} \quad (4.2)$$

Inserting the isentropic expansion factor $\kappa = 1.402$ for air and the ISA values for the pressure and the density from table 4.1 yields $a_0 = 340$ m/s. Mach numbers are provided in terms of the equivalent air speed V_{EAS} and the speed of sound a_0 in this thesis.

The lift coefficient of the wing c_L is a dimensionless quantity which gives information about the flight condition in which the aircraft is:

$$c_L = \frac{L}{q S_{wing}} \quad (4.3)$$

where S_{wing} denotes the wing reference area, whereas the wing generating lift L equals the load factor n multiplied by the product of mass m and gravitational constant $g_0 = 9.81$ m/s²:

$$L = n m g_0 \quad (4.4)$$

The wing reference area is set to be $S_{wing} = 8.72$ m² for lift coefficient calculations. Wing reference data from preliminary studies are listed in the appendix.

For the evaluation of local lift coefficients c_l , i.e. for certain wing cross sections, the lift per unit span l is considered with the local chord length c as reference:

$$c_l = \frac{l}{q c} \quad (4.5)$$

4.1.3 Identification of Load Cases

In order to test the model, simulation results are compared with those from preliminary investigations by a project partner. The structural model of the pre-design only considers the wing torsion box between the spar web and the c web. Therefore, the morphing forward section including the compliant mechanisms is omitted in the structural model.

For model validation, different load cases are considered, which allow a comparison of the structural behavior in different operational areas of the flight envelope. These and their numbering form an extract of the load case table of a project partner for the structural verification according to the approval regulation CS-22 (EASA 2003) and are listed in table 4.2.

Table 4.2: Relevant load cases to compare for model validation.

Load Case	Description	V_{EAS} [km/h]	n [-]
101	Recover at design maneuvering speed	220	5.3
103	Recover with extended airbrakes at dive speed	312	3.5
117	Glide at high lift coefficient	95	1.0

- **Recover at design maneuvering speed**

This load case represents recovering at design maneuvering speed $V_{EAS} = 220$ km/h (V_A) and a vertical acceleration of $5.3 g_0$ at MTOM. The wing is in unmorphed condition. During this maneuver, the wing must generate a high amount of lift according to equation (4.4) to compensate for the high load factor. The high mass of the sailplane further increases the lift demand, so that the transverse forces in z -direction and the resulting moments around the x -axis result in high amounts. As a consequence, large deformations are to be expected, in particular upward twists, which is why this load case is to be considered dimensioning for the wing with a lift coefficient of $c_L = 1.6$, derived from equation (4.3).

- **Recover with extended airbrakes at dive speed**

This load case simulates the airbrake extension during a fast descent from high altitudes at dive speed $V_{EAS} = 312$ km/h (V_D) at MTOM and unmorphed wing. At the same time, a positive acceleration of $3.5 g_0$ is acting. The airbrakes lead to a drop in lift and a drastic increase in drag in the middle wing area. To compensate for the local lift reduction, the lift in the outer area increases, which leads to high transverse forces in z -direction and thus high bending and torsion moments.

- **Glide at high lift coefficient**

This load case represents a glide with $1.0 g_0$, MTOM and unmorphed wing at estimated stall speed $V_{EAS} = 95 \text{ km/h}$ (V_{S1}) and thus another edge of the flight envelope. It serves to investigate the structural behavior near stall separation at high lift coefficients ($c_L = 1.6$). Due to the comparatively low transverse forces, the structural response is to be considered less critical. However, even small twists can lead to local lift drops for the already high angles of attack.

4.1.4 Comparison of Simulation Results

The assumptions made for the analytical investigations of preliminary studies, carried out by a project partner, are that:

- airfoil aerodynamics are carried out with two-dimensional panel methods, whereas
- wing aerodynamics are calculated by means of an extended lifting-line theory (Mulhopp approach).
- For analytical structural mechanics the wing spar is modeled as a beam and the wing shell as a plate.

With few exceptions in the model, which are explicitly mentioned in the explanations, identical input values are used for the numerical investigations as for the analytical preliminary studies.

Most FE solvers, also NASTRAN, work without physical units. The user must therefore ensure that consistent unit systems are used. These usually depend on the country or application. In Europe, the usual system is [t – mm – s] for structural analysis, since the resulting stresses are specified in N/mm² or rather MPa. The NASTRAN input parameters converted into this unit system are listed in a table 4.3. The values for the vertical acceleration u result from multiplying the gravitational constant g_0 with the respective load factor n from table 4.2.

Table 4.3: NASTRAN SOL144 input values for model validation.

Load Case	q [t/mm s ²]	Ma [–]	u [mm/s ²]
101	2.2874×10^{-3}	0.179	51 993
103	4.6006×10^{-3}	0.255	34 335
117	4.2653×10^{-4}	0.077	9810

Post-processing and result visualization is done by means of HYPERVIEW. The raw data are further processed with MATLAB.

Recover at design maneuvering speed

Figure 4.1 shows the deformed structure at load case 101. Positive values for rotations around the y -axis that come closest to the actual wing twist are displayed in color.

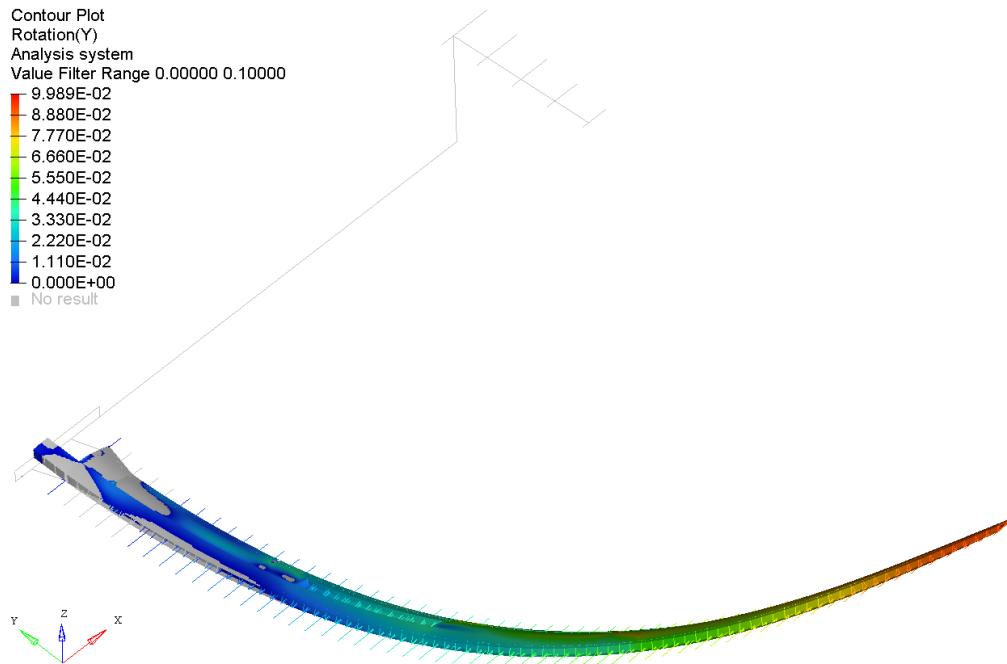


Figure 4.1: Primary structure excluding morphing forward wing section. Twist with respect to the y -axis at load case 101.

The rigid wing has a constant dihedral of $\phi = 3.5^\circ$ along the entire wing span, which is the rotation angle of the non-deformed elastic axis around the x -axis. According to equation (4.6), twist angles around this axis differ from those around the y -axis by 0.2%, which is a negligible order of magnitude in twist evaluation.

$$\theta_{rigid} = \frac{\theta_y}{\cos \phi} \quad (4.6)$$

Further, in the case of small deflection angles, real twist angles around the deformed elastic axis are similar to those with respect to the non-deformed elastic axis and so to the y -axis. However, for large deflections as at the considered load case, it is advisable to consider the twist in relation to the deformed elastic axis as illustrated in figure 4.2.

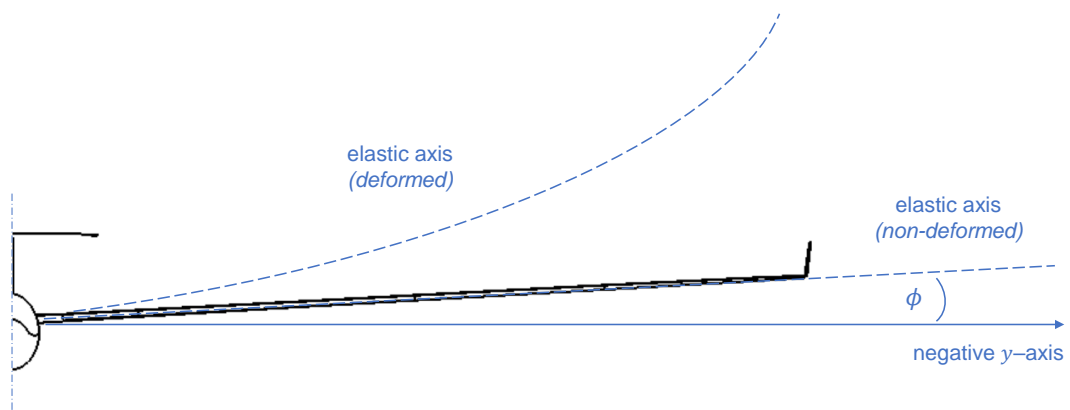


Figure 4.2: Reference axes to describe wing twist.

Figure 4.3 shows twist values. The rigid body rotations of the RBE2 elements that represent the interface between structure and aerodynamic model are used for the evaluation.

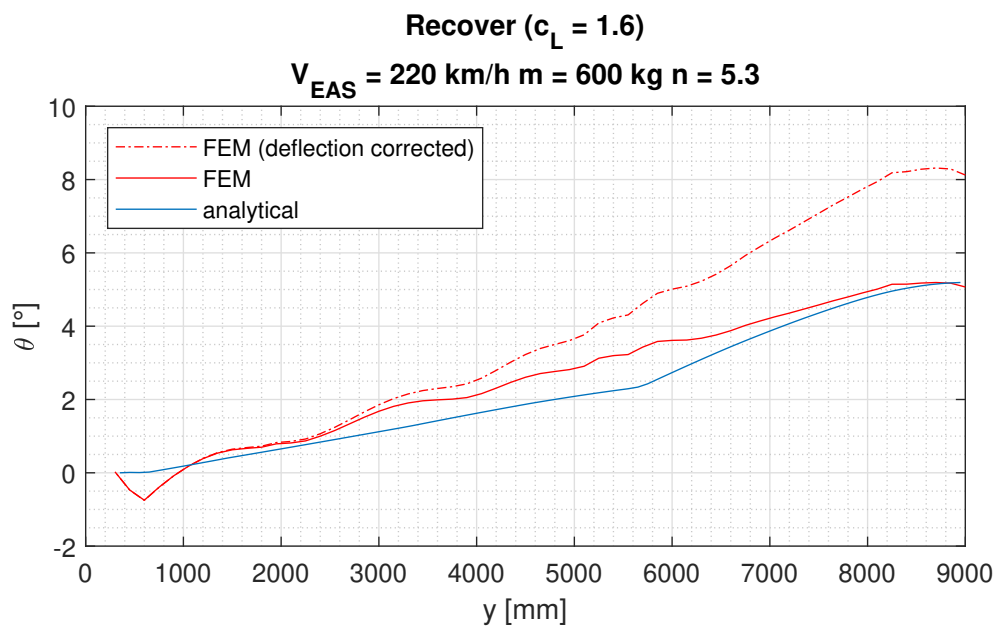


Figure 4.3: Wing twist at load case 101. Continuous lines refer to the non-deformed elastic axis, the dot-dashed line refers to the deformed elastic axis.

Local differences between the two model results (continuous lines) are clearly visible. An initial negative twist results from the trapezoidal geometry of the inner wing, which is reinforced with additional UD plies for load introduction and thus causes a local displacement of the elastic axis. In particular the interrupted wing shell from $2346 \text{ mm} \leq |y| \leq 3589 \text{ mm}$, where the

airbrake is located, leads to a local increase of the twist. This offset remains in the further course of the curve towards to the wing tip. It is not precisely identifiable in which extent the duct at $|y| = 2000$ mm contributes to the local increase of twist, as the effect of the closely located airbrake box predominates. However, a small peak is noticeable and indicates its presence. The kink at $|y| = 5300$ mm, where the second duct is placed, is more apparent, confirming the assumption that local incisions in the wing box significantly influence the overall torsion. Another jump is assigned at $|y| = 5628$ mm, where the wing is separated and the shell layup changes, which indicates a local reduced torsional stiffness.

This effect becomes even more apparent when the twist is considered with respect to the deformed elastic axis (dot-dashed line). It deviates from the torsion around the elastic axis of the rigid wing since the deflection increases towards the wing tip and so does the angle between the deformed and the non-deformed elastic axis. This method allows a qualitatively more accurate assessment of the torsional stiffness along the span, but is not applied further, as wing twist generally refers to the non-deformed wing whereby it can be determined independently from wing deflection (Wright 2015).

The slope of the red line flattens again to the right of the wing separation point and is almost identical to the previous, averaged one. On the contrary, the blue curve shows a clearly different course in the outer area. This can be explained by the fact that the position of the spar web in the inner wing area is fixed at 25 % of the spar cap depth, while in the preliminary design it coincides with the front edge of the spar cap. This is, besides the presence of an airbrake box, another factor that reduces the torsional stiffness in the inner wing area, recognizable by the divergence between the red and the blue curve up to the wing separation point. In the outer wing area, the spar web in both models lies at the front edge of the spar cap. However, in this thesis, the shell extends beyond the spar cap in direction of flight up to the edge, where the morphing skin begins, which in turn increases torsional stiffness compared to the preliminary design, where the wing shell ends with the spar web. Both effects, i.e. the relative reduction of the torsional stiffness in the inner area and the increase in the outer area compared to those of the pre-design, compensate each other in global, so that the twist values at the wing tip are approximately the same.

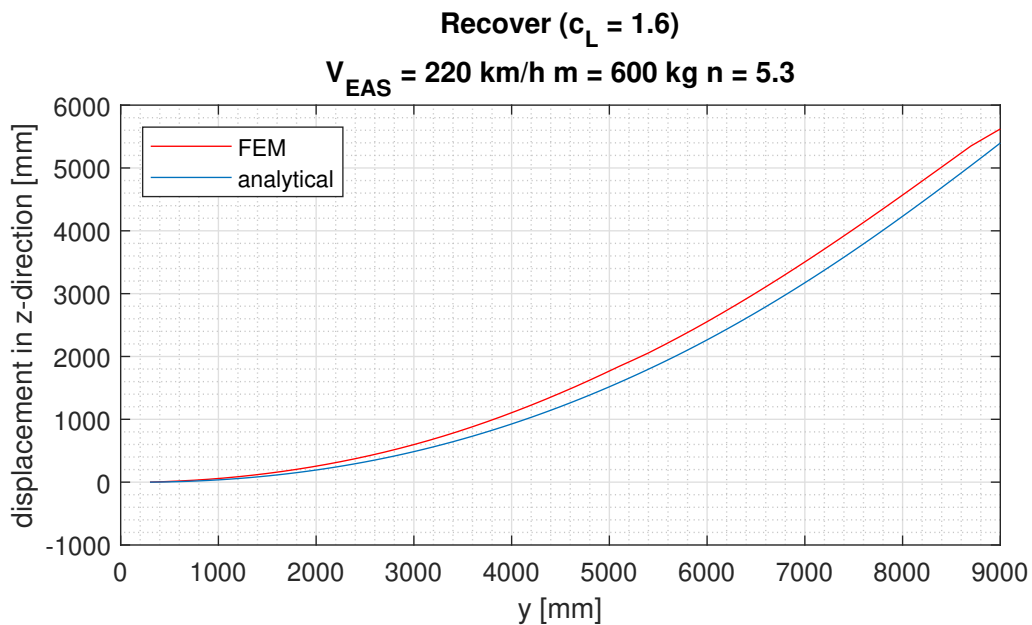


Figure 4.4: Wing deflection at load case 101.

Figure 4.4 shows the displacement of the wing in z -direction, where the y -axis represents the semi-span of the non-deformed wing. The true y -values of the deformed wing are smaller due to geometrical constraints, which is not shown here. Comparing the two lines with each other, a difference in the initial slope at $|y| = 300 \text{ mm}$, where the wing is attached to the fuselage, can be recognized. This is due to the boundary conditions. In the structural preliminary design it was assumed that the wing is fixed to the fuselage, preventing rotation of the root rib around the x -axis. As described previously in detail, the boundary conditions in this thesis allow the wing root to rotate, resulting in an initial slope of approximately 3° . This angle leads to a deviation of the deflection at the wing tip of approximately 220 mm or rather 4% at load case 101, which does not considerably affect the twisting behavior.

The analyses carried out so far are considered to be sufficient to validate the structural model for the use in further development steps. For the verification of the aerodynamic model the local lift coefficients are compared with each other.

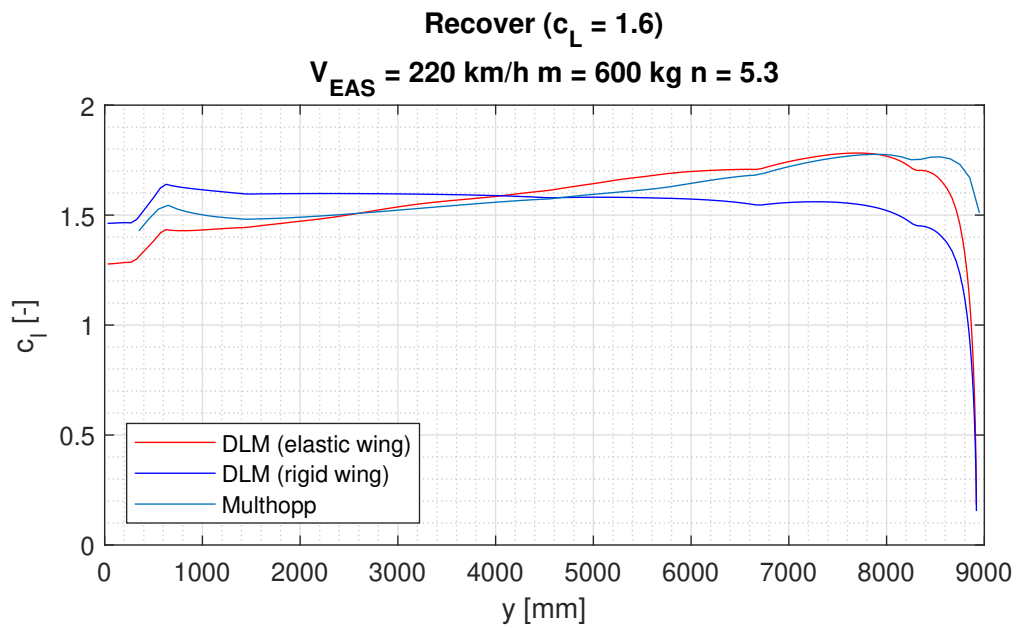


Figure 4.5: Local lift coefficient distribution at load case 101.

Figure 4.5 shows the distribution of local lift coefficients c_l along the span. The values from the DLM fit well with those from the preliminary investigations, which were determined by means of a Multhopp procedure. Towards the wing tip there are recognizable differences between the curves, which are due to the missing winglet. However, this is only a marginal effect that has negligible consequences on the overall deformation of the wing.

By comparing the elliptical lift distributions of the elastic wing and the rigid, non-deformed wing with each other in figure 4.6, the redistribution of lift caused by the wing twisting becomes easily recognizable. In the former case, the outer wing experiences higher angles of attack that are accompanied by an increase in lift. Since the mean value of all lift coefficients, multiplied with the local chord and divided by the mean aerodynamic chord (MAC), distributed over the entire span must remain constant in each configuration, i.e. elastic and rigid, an increase of lift towards the wing tip inevitably leads to a reduction towards the wing root. This also has the secondary effect of an increased root bending moment and is rather undesirable for the structural design.

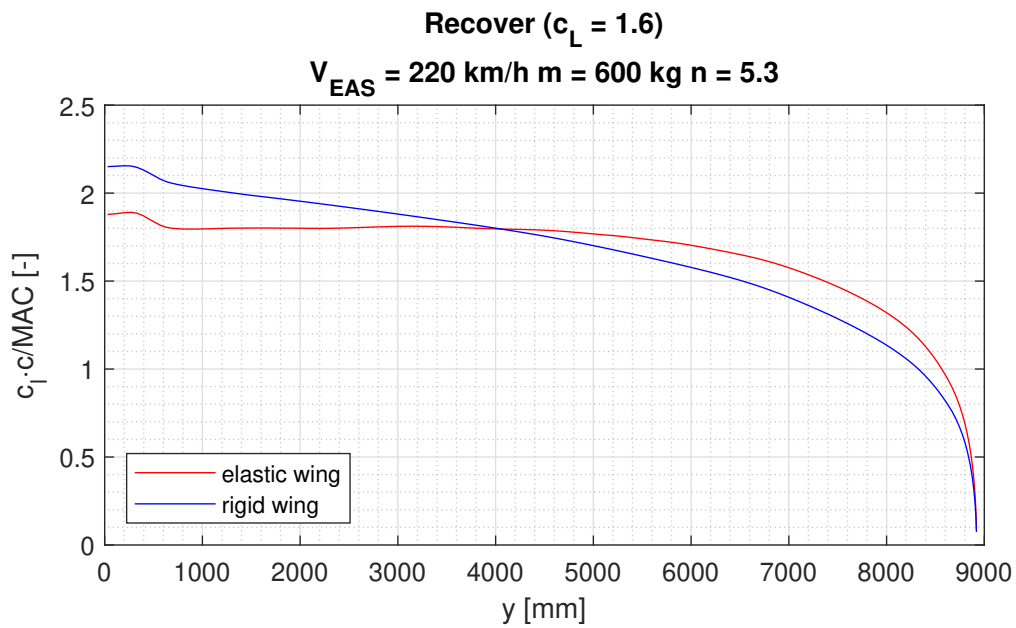


Figure 4.6: Elliptical lift distribution at load case 101.

Recover with extended airbrakes at dive speed

Figure 4.7 shows the distribution of local lift coefficients at load case 103. It is assumed that the airbrake causes a change in the angle of attack of -11.5° from $2346 \text{ mm} \leq y \leq 3589 \text{ mm}$ with reduced lift in this range. As suspected, the airbrake induces a local drop in lift.

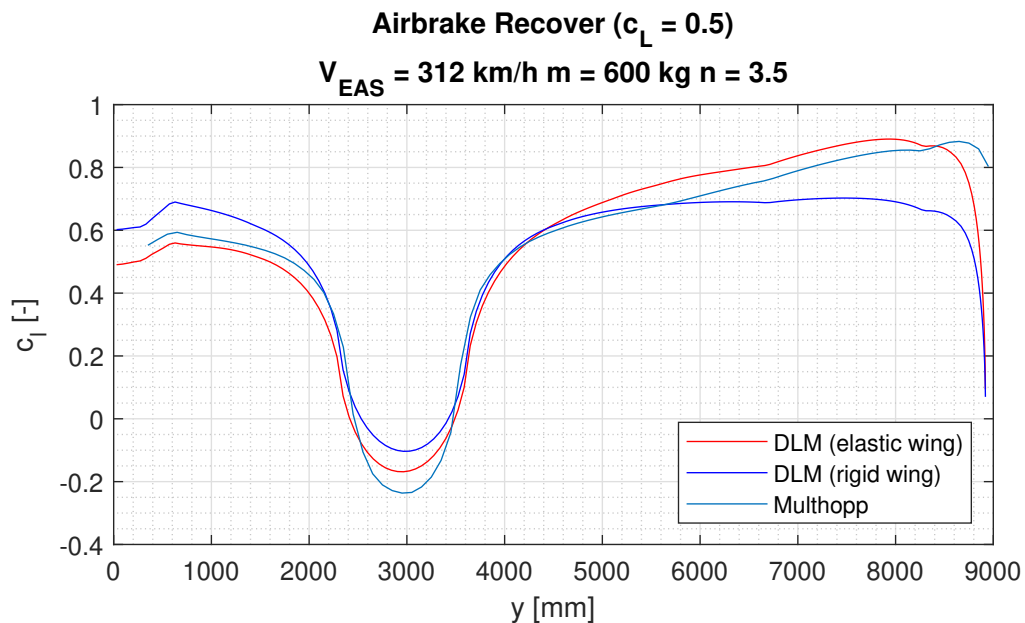


Figure 4.7: Local lift coefficient distribution at load case 103.

To compensate for the local lift drop, the lift coefficients are relatively high in the outer wing area, causing severe torsion. This load case is particularly suitable for validating the aerodynamic model, since the loss of lift in the area of the extended airbrake provides information whether the affected boxes are correctly addressed in the script of camber assignment.

The associated wing torsion in figure 4.8 shows a similar progression to that of the recover load case 101 at $n = 5.3$. Due to the lower lift coefficients caused by the lower load factor $n = 3.5$, the total twist is correspondingly less. In the area of the extended airbrake, the slope of the curves are lower, since the structure experiences less aerodynamic torsional moments.

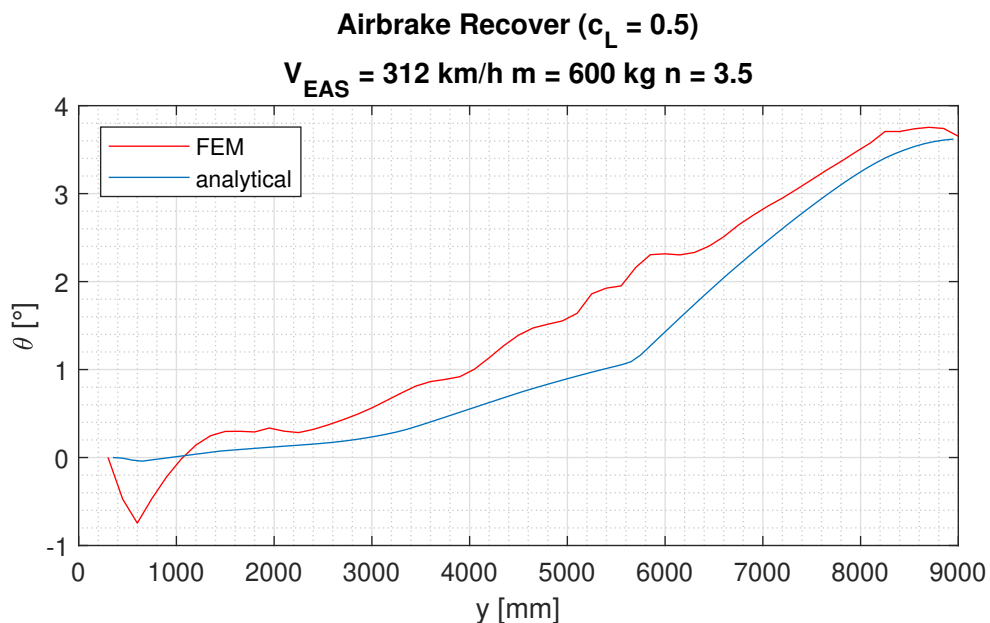


Figure 4.8: Wing twist with respect to the non-deformed elastic axis at load case 103.

Glide at high lift coefficient

Analyzing the local lift coefficients for load case 117 in figure 4.9, it can be seen that the reduced torsional stiffness of the wing has hardly any effect on their distribution. The curves for the elastic and the rigid wing are very close to each other and with the exception of the outer area where the winglet is placed, the small differences to the results from the preliminary investigations can be attributed to the applied calculation methods.

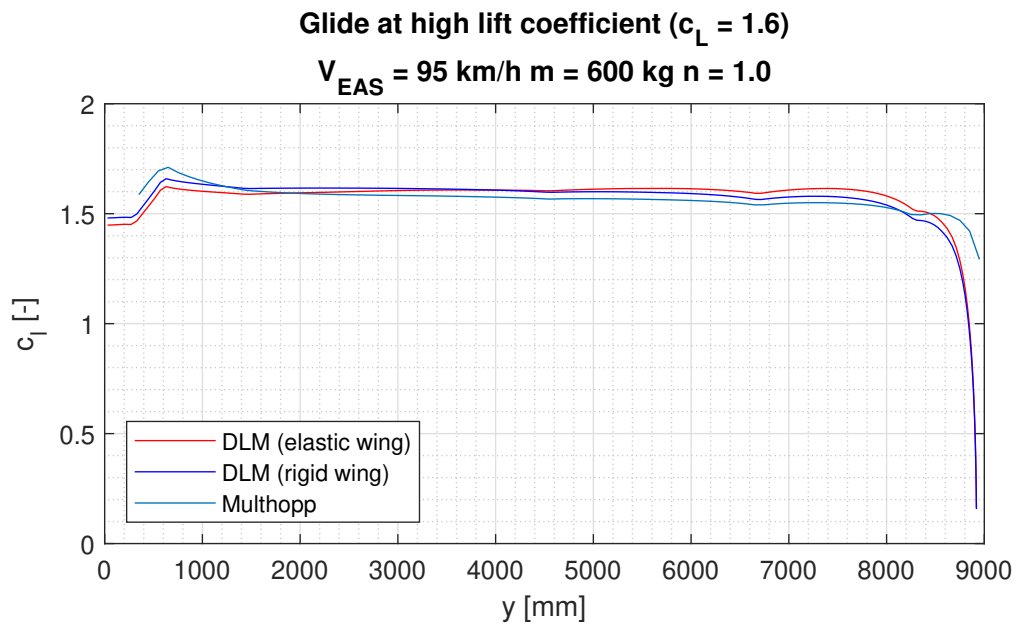


Figure 4.9: Local lift coefficient distribution at load case 117.

The deflection and twist courses are similar to those of load case 101, but due to the load factor $n = 1.0$ and the low dynamic pressure at $V_{EAS} = 95 \text{ km/h}$ they are scaled correspondingly low. The maximum deflection at the wing tip is about 950 mm and the value for twist at this point arises to 0.9° , which is shown in the appendix.

The comparison of the results from all three investigated load cases clearly shows that the wing deflection and twisting strongly depends on the lift distribution. High lift coefficients, as they can be seen at load case 101, have drastic effects on the aeroelastic deformation behavior of the wing box.

4.2 Investigations on Static Aeroelastic Responses

Up to this point, the morphing forward wing section has been omitted in order to validate the crucial wing box model. As announced in chapter 4.1.1, despite the open cross section, the morphing forward section including the compliant mechanisms that is connected to the spar web has a significant influence on the torsional stiffness of the entire wing and is therefore counted as part of the primary structure for further investigations.

4.2.1 Supplementation of Load Cases

Although the load cases considered so far allow an assessment of the structural strength, this does not represent a realistic consideration of the flight conditions. Aeroelastic Tailoring is

therefore not meaningful for maximum loads, since values for twist and deflection do not reflect those that occur during usual flight. Therefore, two additional representative load cases from the envelope are selected, which are of great importance for an optimization of the performance parameters.

- **Cruise flight at design lift coefficient**

During cross country gliding, it is advisable to choose high cruising speeds between upwinds in order to increase the average speed. The respective load factor is $n = 1.0$ under the assumption of steady air conditions, i.e. the absence of vertical gusts. Due to the high wing loading at MTOM, a speed of $V_{EAS} = 220 \text{ km/h}$ is recommended, at which the design coefficient $c_L = 0.3$ is achieved. Since wing twisting is accompanied by a heavy loss of performance, it is necessary to optimize for this scenario, which is assigned the number 201 within this thesis.

- **Thermaling flight with morphed wing**

The circle flight at relatively low speeds and high induced drag takes up about 30 % of the total flight time in thermal cross country gliding. Accordingly, the maximum aerodynamic performance must also be given in this scenario.

Figure 4.10 illustrates the effect of an increased load factor due to the presence of the centrifugal force Z during stationary circle flight at constant altitude. For the herein performed considerations a bank angle of $\theta = 40^\circ$ is assumed, which corresponds to empirical values, leading to a load factor of $n = 1.3$ according to

$$n = \frac{1}{\cos \theta} \quad (4.7)$$

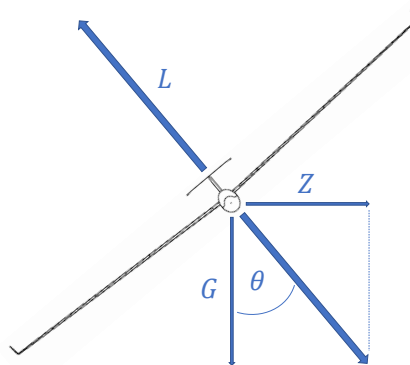


Figure 4.10: Increasing load factor due to centrifugal force Z in stationary level circle flight.

By means of equation (4.3) and a speed of $V_{EAS} = 110$ km/h at MTOM, the lift coefficient of the wing results in $c_L = 1.5$, which is still within the permissible range before flow separation. The wing is, in contrast to previous mentioned configurations, in morphed condition. Within this thesis, this load case is assigned the number 202.

Table 4.4: Relevant load cases for further aeroelastic investigations.

Load Case	Description	V_{EAS} [km/h]	n [-]
101	Recover at design maneuvering speed	220	5.3
201	Cruise flight at design lift coefficient	220	1.0
202	Thermaling flight with morphed wing	110	1.3

Load case number 101 is additionally analyzed in order to show the effect of the morphing forward wing section on the overall torsional stiffness of the wing, comparing the simulation results with those in chapter 4.1.4. The according parameters are listed in table 4.5.

Table 4.5: NASTRAN SOL144 input values for further aeroelastic investigations.

Load Case	q [t/mm s ²]	Ma [-]	u [mm/s ²]
101	2.2874×10^{-3}	0.179	51 993
201	2.2874×10^{-3}	0.179	9810
202	5.7186×10^{-4}	0.090	12 753

4.2.2 Analysis of Simulation Results

In chapter 4.1.1 it has already been pointed out that, despite the open cross section, the morphing forward wing section has a considerable influence on the torsional stiffness of the entire wing. For this reason, it cannot be omitted from aeroelastic investigations. Here, the advantages of the FEM, compared to the analytical structural analysis, become clear. Even the complex geometry of the morphing forward wing section including its structural components, as extensively described in chapter 3.2, can be easily modeled and a computer handles the numerical solution within very little time.

Recover at design maneuvering speed

Figure 4.11 shows the deformed primary structure including the morphing forward wing section at load case 101. For reasons of clarity, the RBE2 elements are not displayed.

The transition area from inner to outer wing is distinctly visible, where the angles of twist

increase drastically due to the layup induced torsional stiffness reduction. Furthermore, the color differences indicate local effects in the area of the morphing skin. Where the ribs are located, the local angles of twist are smaller than in the intracellular area. For a global view of the twist, only the RBE2 elements being connected to the wing box are evaluated.

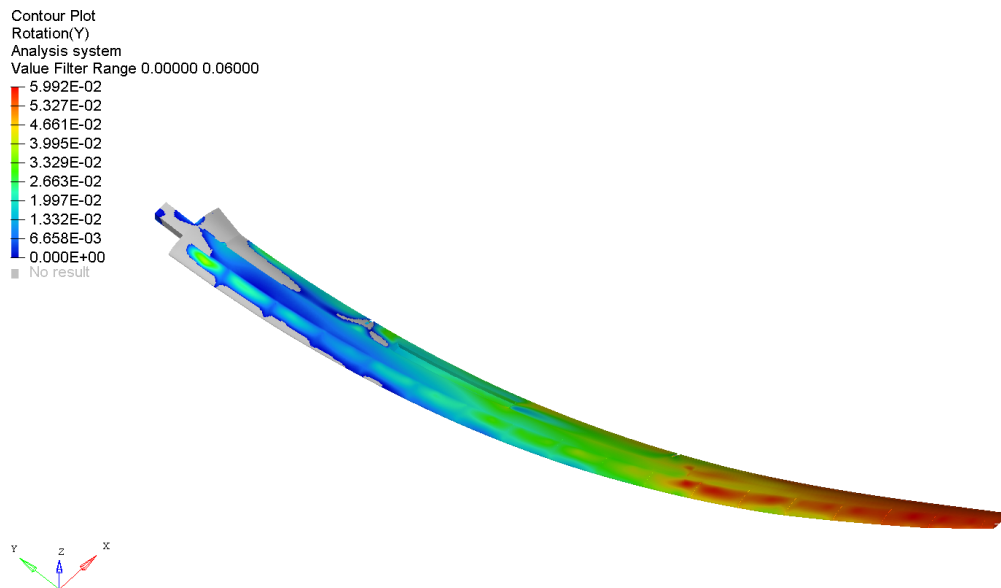


Figure 4.11: Primary structure including morphing forward wing section. Twist with respect to the y -axis at load case 101.

Considering the course of the curves in figure 4.12, it becomes clear at first glance that the absolute values of the wing twist are significantly lowered by taking the morphing forward wing section into account.

Especially in the outer wing area, where the layup of the wing shell changes, the layup of the morphing skin remains the same as in the inner wing area, whereby its percentage of the overall cross sectional torsional stiffness increases. This leads to the observation that with 3.2° the wing tip now twists up only 68 % as much as the purely wing box with respect to the non-deformed elastic axis.

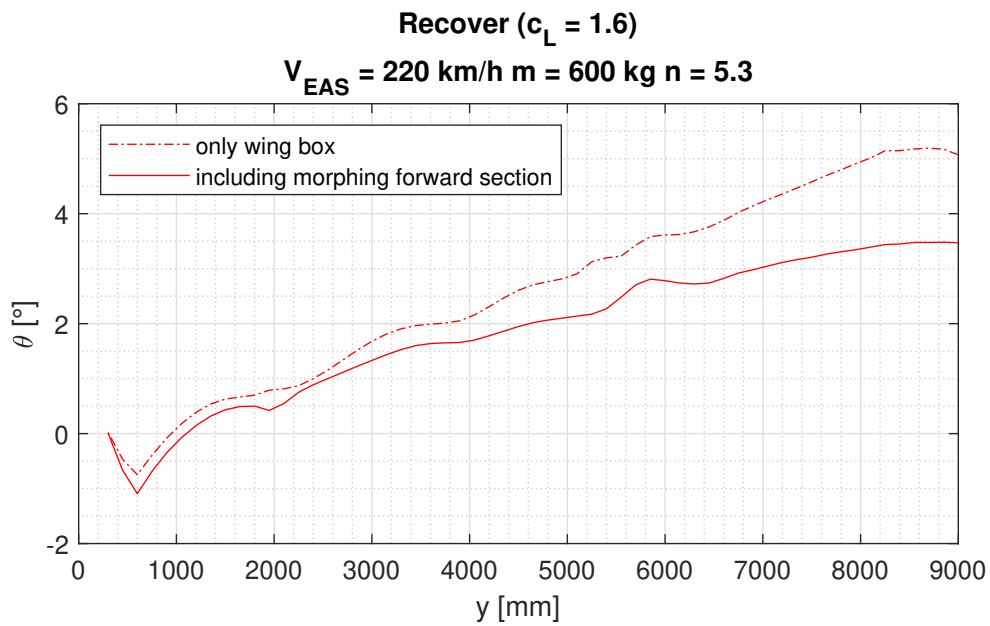


Figure 4.12: Effect of morphing forward wing section on twist behavior at load case 101.

It should be noted, however, that the compliant mechanisms being modeled as isotropic ribs with reduced stiffness and the actuators as well as the connection of the open morphing skin to the spar web via normal force joints overstate the torsional stiffness of the morphing forward wing section. Figure 4.12 therefore represents minimum and maximum values for the wing twist and the true values are assumed to be somewhere in the middle between the displayed curves.

Looking at the deflection lines in figure 4.13, it is noticeable that the wing deflects only 82% as much under the influence of the morphing forward wing section as under its neglect. This is for one thing due to the increase in bending stiffness, since the cross sectional area extends in x -direction and thus the second moment of area. On the other hand, the redistribution of lift with higher coefficients towards the wing root (see figure 4.14 and 4.15) reduces the root bending moment and the overall deflection. This is due to the fact, that lower twist angles result in lower local angles of attack and thus transverse forces.

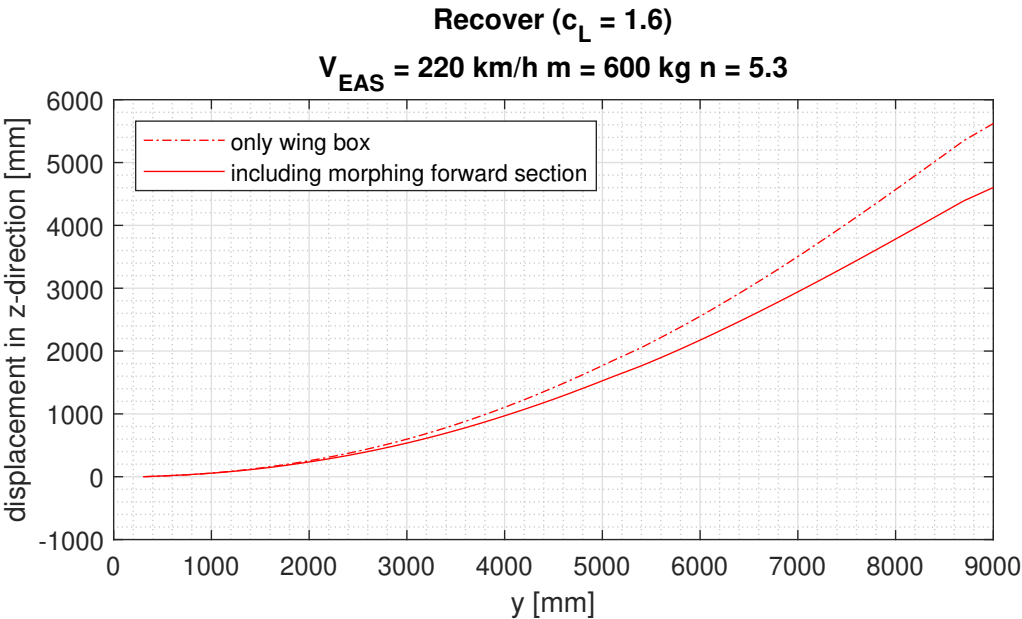


Figure 4.13: Effect of morphing forward wing section on deflection behavior at load case 101.

Figures 4.14 and 4.15 show that the reduced twisting of the wing also has a significant effect on the distribution of the lift coefficients. This is due to the reduction of local angles of attack, so that the point of resulting lift application moves further towards the wing root.

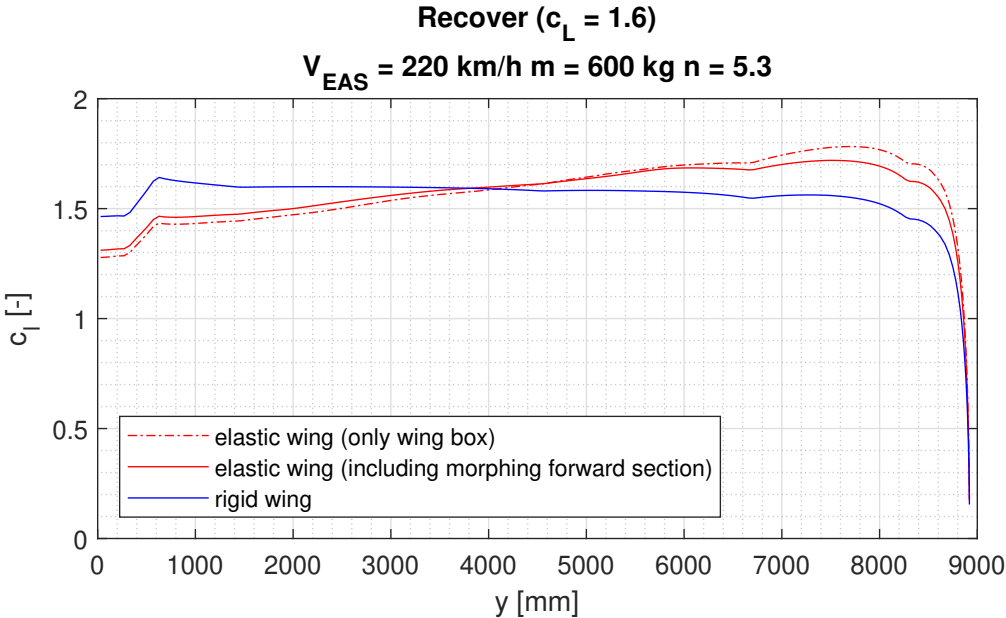


Figure 4.14: Effect of morphing forward wing section on local lift coefficient distribution at load case 101.

The comparison of the three curves in each diagram provides information on how the torsional stiffness of the morphing forward wing section affects the redistribution of lift in relation to the rigid wing. In terms of percentage, the change is in the same order of magnitude as that of the twisting in figure 4.12.

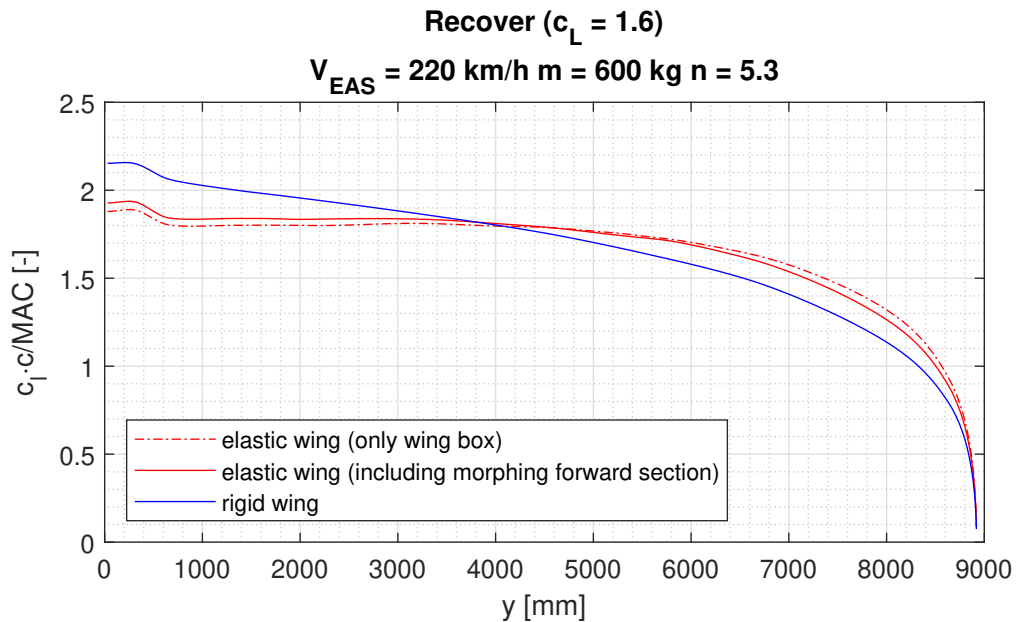


Figure 4.15: Effect of morphing forward wing section on elliptical lift distribution at load case 101.

Cruise flight at design lift coefficient

Figure 4.16 illustrates the wing twist at load case 201. Looking at the vertical scale, it becomes clear that the angle values now scatter only by approximately 1° . The locations of reduced torsional stiffness mentioned in chapter 4.1.4 can be seen more clearly. These include the ducts for the control rods, the airbrake box as well as the wing separation point.

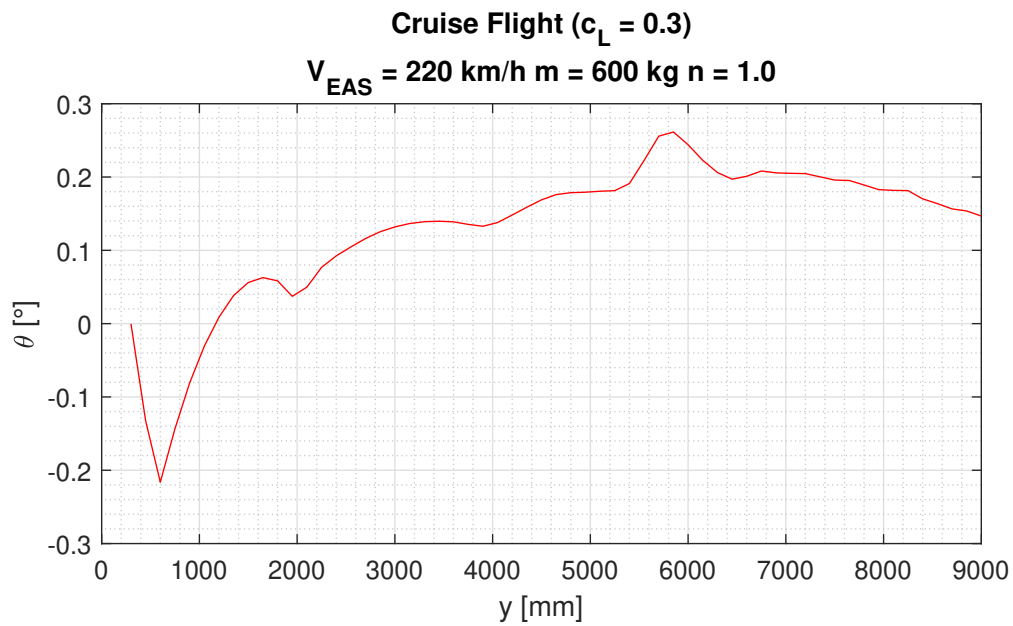


Figure 4.16: Wing twist at load case 201.

The initial negative twist, which was already visible in the previous diagrams, is conspicuous. Being significantly influenced by the composite layup in the areas of load introduction as well as the geometry of the divided spar web, this value should be viewed critically, since its amount is similarly large as the maximum value for the positive twist at this load case. The values of the curve differ from those at load case 101 in the outer wing region where the twist again decreases towards the wing tip. This is due to the fact, that with the comparatively low lift forces at $c_L = 0.3$ (figure 4.17), the restoring moments of the structure predominate the aerodynamic pitching moments.

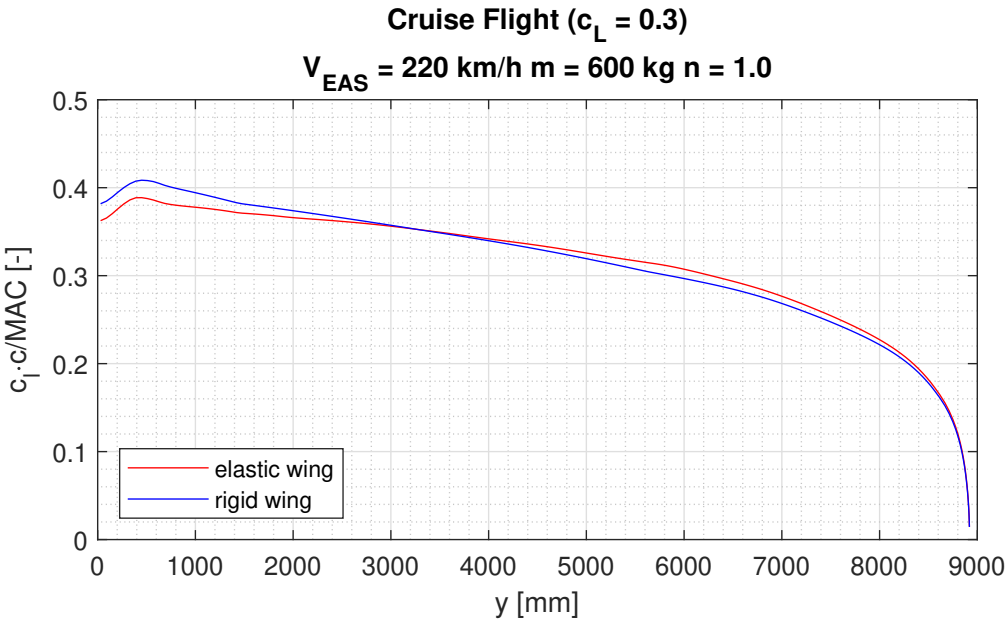


Figure 4.17: Elliptical lift distribution at load case 201.

Cruising with $1.0 g_0$ results in comparatively low wing deflections, as it can be seen in figure 4.18. The vertical displacement of 810 mm at the wing tip and the corresponding strains in the structure are in an order of magnitude in which geometric nonlinearities can be neglected.

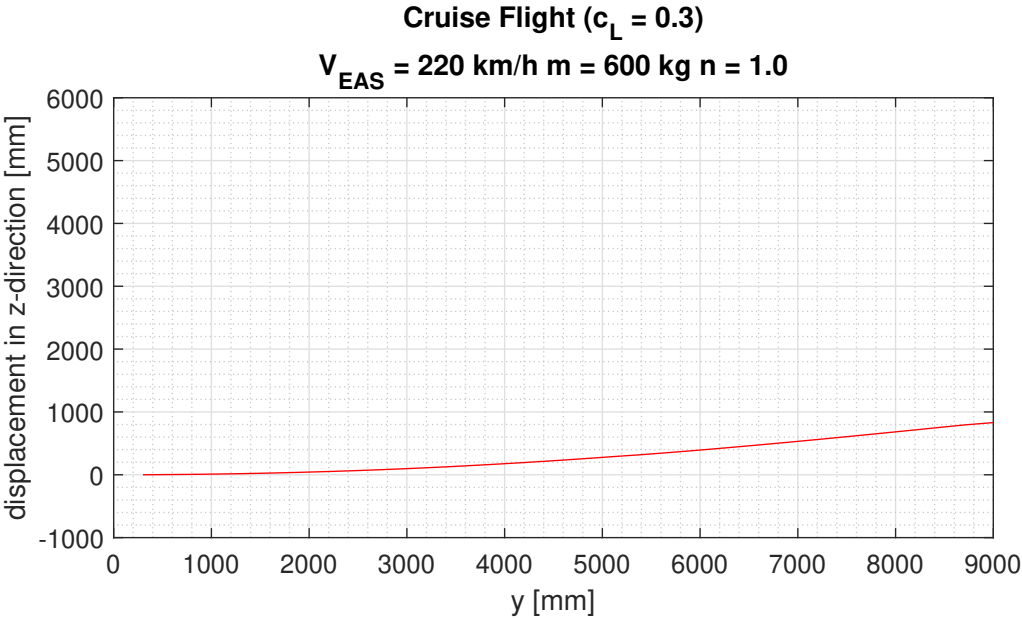


Figure 4.18: Wing deflection at load case 201.

Thermaling flight with morphed wing

As previously outlined, the airfoil camber change due to the lowering of the morphing forward wing section is taken into account in the aerodynamic model, whereas the structural model remain unchanged for reasons of simplicity. This abstraction is based on the assumption that the lowered morphing skin has marginal effects on the overall structural stiffness. Figure 4.19 illustrates the wing twist during thermaling flight.

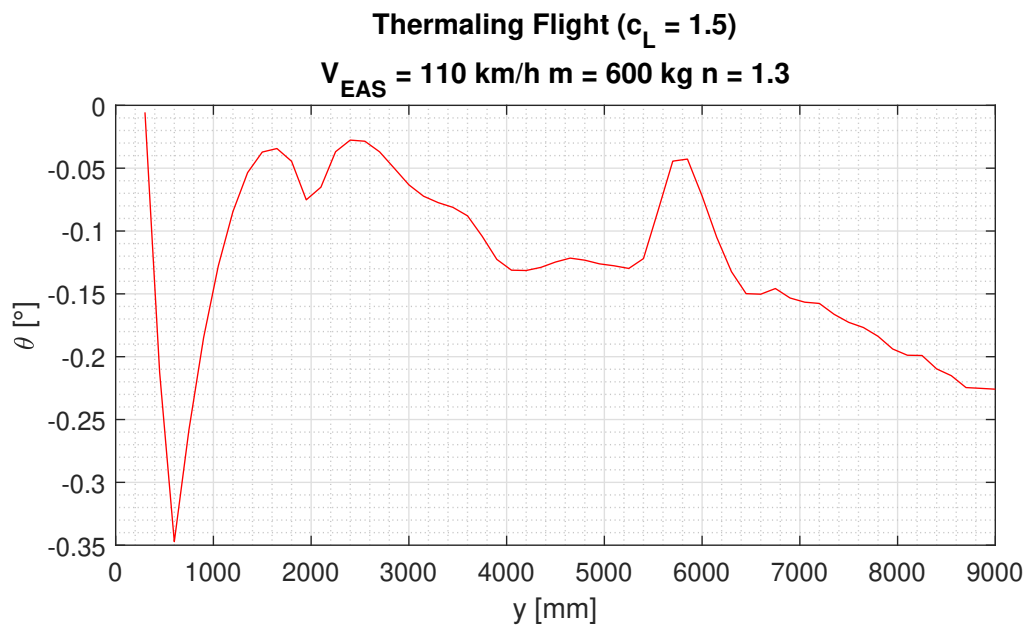


Figure 4.19: Wing twist at load case 202.

Now it becomes clear, that mainly the ducts at $|y| = 2000 \text{ mm}$ and $|y| = 5300 \text{ mm}$ are causing local twist jumps. Furthermore, the twist has negative values along the entire wing span and its minimum value, neglecting the initial twist, at the wing tip. The twist angles are in the same order of magnitude as at load case 201, but with the opposite sign.

A positive deflection, i.e. in negative z -direction, of any control surface, i.e. flap or morphing forward wing section, increases airfoil camber and thus lift. The redistribution of chordwise pressure, i.e. the changed lift resultant point of attack, combined with an increased gravitational force, leads to a nose-down moment.

The wing tip is deflected by 1040 mm in positive z -direction due to the load factor of $n = 1.3$ and the resulting lift increase. However, the little wing twist hardly affects the elliptical lift distribution, as the curves for the rigid and the elastic wing in figure 4.20 are nearly the same.

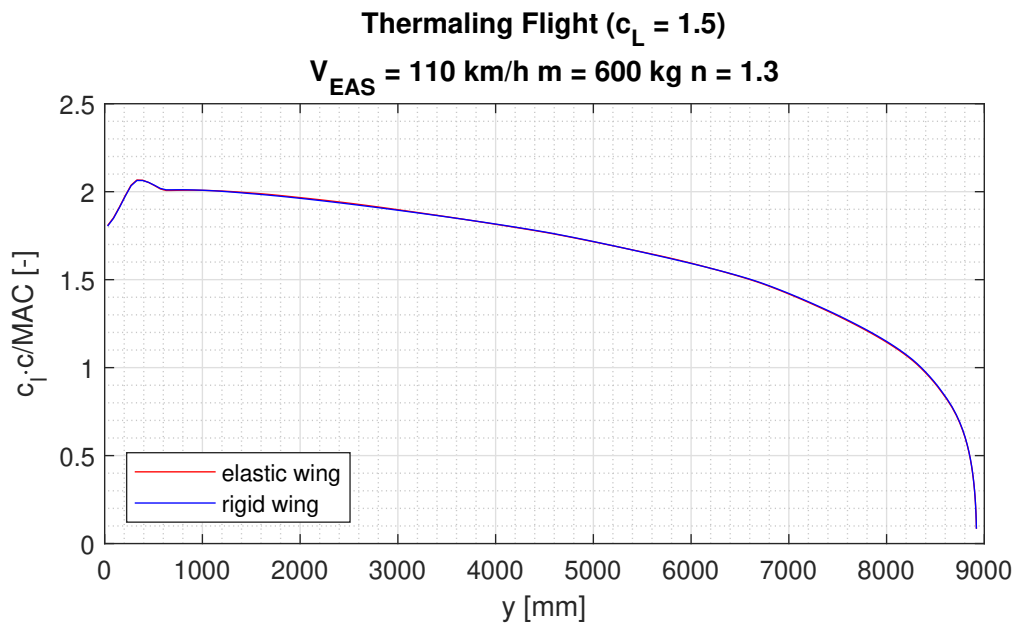


Figure 4.20: Elliptical lift distribution at load case 202.

4.2.3 Effect of Aeroelastic Tailoring

Up to this point, all aeroelastic investigations have been performed for a conventional shell layup with $\pm 45^\circ$ fiber angles as described in chapter 3.3.1. This is due to the fact, that the wing shell is loaded in shear whereas the 0° oriented spar rovings carry normal forces that result from bending moments. Furthermore, this layup is balanced with regard to the laminate main direction, i.e. the spar axis. As bending does not affect torsion in this configuration, structural twist mainly results from aerodynamic moments. Aeroelastic Tailoring, in contrast, makes targeted use of the anisotropy of unbalanced laminates in order to force bending-torsion coupling. The effect of single ply angle variations is illustrated in figures 4.22, 4.23 and 4.24, giving a general impression of how the fiber angle influences the twisting behavior under different load conditions. In order to get a first idea, constant ply angles are assumed along the entire span, which are the same for the above and the bottom side of the wing.

In each diagram, ply orientations, i.e. the respective 0° fiber direction of the weave lamina, refer to the spar axis. Positive angles describe ply rotations towards the leading edge. Since only weave lamina is used, a fiber orientation of 20° towards the leading edge, for instance, is accompanied by a -70° rotation of the respective contrary fiber, i.e. towards the trailing edge. This example is illustrated in figure 4.21.

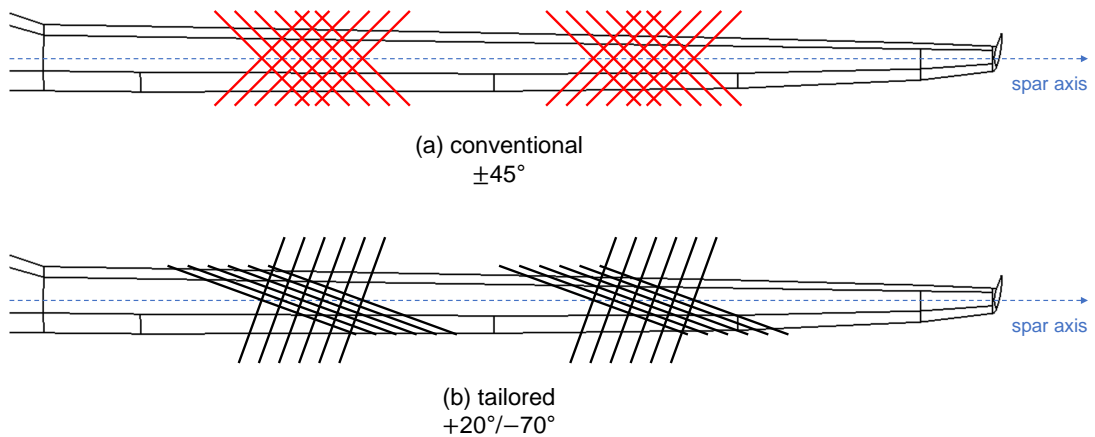


Figure 4.21: Orientation of fibers for conventional layup scheme (a) and applying Aeroelastic Tailoring for the wing box (b).

Figure 4.22 shows that at load case 101 the aeroelastic twist can be significantly reduced by rotating the top and bottom shell weave laminates by only 10° towards the trailing edge along the entire span. Rotations towards the trailing edge would show the reverse effect of twist enhancement and therefore are not displayed.

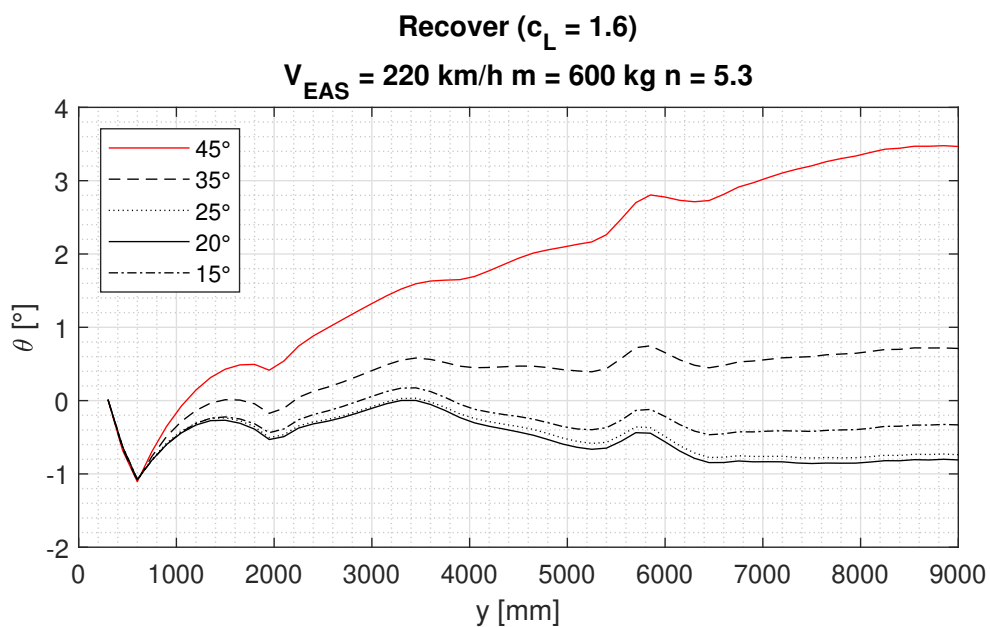


Figure 4.22: Effect of ply angle variation at load case 101.

As all three diagrams indicate, a ply rotation of 20° towards the leading edge causes the strongest bending-torsion coupling, which counteracts the aeroelastic twisting of the wing.

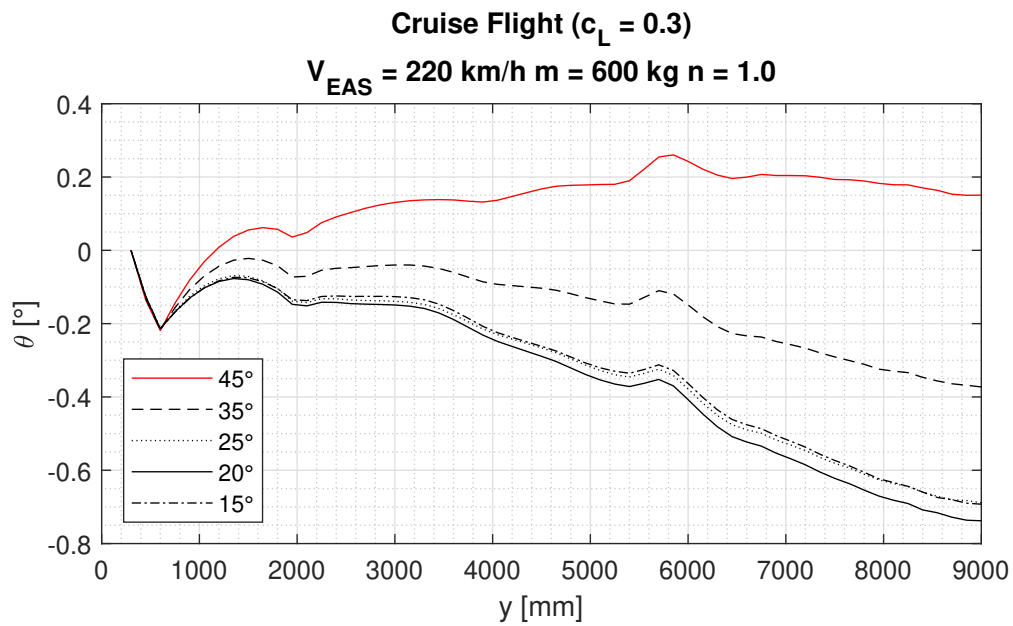


Figure 4.23: Effect of ply angle variation at load case 201.

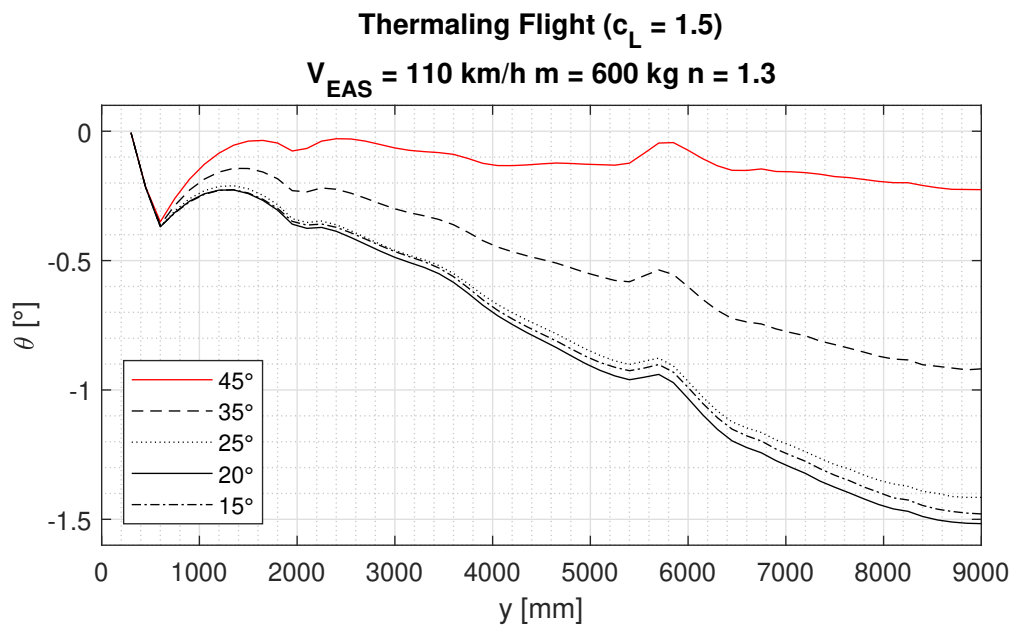


Figure 4.24: Effect of ply angle variation at load case 202.

This is due to the fact, that the maximum unbalanced laminate with non-zero entities D_{16} and D_{26} in the corresponding ABD matrix theoretically is achieved by a ply rotation of 22.5° , which is the mean value between 45° and 0° , which both result in balanced layups with the absence of any bending-torsion coupling. The displayed 20° curve comes closest to this value.

Aeroelastic Tailoring generally aims to avoid wing twisting along the whole span. This can only be achieved for a designated design load case. Figure 4.23 shows that a ply angle somewhere between 45° and 35° fits best to get zero twist during cruising at maneuvering speed. This is, from an aerodynamic point of view, optimal to exploit maximum gliding performance. However, as figure 4.24 indicates, the same ply orientation causes negative twist enhancement during thermaling flight. Therefore, for the further development process, a compromise has to be found between minimal positive wing twisting during cruise flight at design speed and minimal negative wing twisting during thermaling flight. Moreover, an increased absolute torsional stiffness of the wing has to be achieved.

5 Conclusion and Outlook

Within the scope of the present thesis, the static aeroelastic behavior of a morphing forward wing section is numerically investigated. A geometrical parametric preliminary design of the wing including airfoil data as well as a structural design, containing the allocation of main components and their material parameters, serve as input for the generation of a detailed simulation model. With the help of these data a surface model is provided in CAD by means of CATIA and manipulated for the further FE-processing. The model contains parametric positions of several main structural components and can be used for further development steps. Based on the finished geometry, a complex computation and coupling model is created in the FE pre-processor HYPERMESH. Moreover, a DL model for the calculation of aerodynamic loads is created, considering the wing planform including airfoil data. MATLAB coded programs support the process of simulation model generation. The finished model, coupling the FE and DL model via an interface, is delivered to the NASTRAN solver for aeroelastic analysis.

Initially, an abstract structural model that only represents the wing box is used to validate the developed coupling analysis by comparing simulation results with those from analytical preliminary investigations. For this purpose, various representative load cases are identified. The results of the present thesis agree well with those from the preliminary investigations. Recognizable differences are due to details in the model formation as well as the applied calculation methods. After model validation, the morphing forward wing section is added to investigate its influence on the torsional stiffness of the entire wing. In order to do so, further load cases are supplemented. These cover a large operating range for both morphed and unmorphed configurations and are therefore especially relevant with regard to structural optimization. Care is taken to implement as many constructive details as possible, e.g. normal force joints bridging the gap between the morphing skin and the wing box in order to obtain not only a qualitative analysis but also physically plausible values for the elastic behavior of the entire primary structure. Twisting and deflection as well as the induced lift redistribution of the wing are analyzed for each load case. It is concluded that the morphing forward wing section contributes substantially to the torsional stiffness and has to be taken into account for further aeroelastic analysis. By means of targeted layup variations, which cause bending-twisting couplings of the structure, it is shown that Aeroelastic Tailoring is not only applicable with regard to a gain in aerodynamic efficiency, but also necessary in order to prevent the wing from structural failure at high loads.

The present results provide essential findings on the structural feasibility of a morphing wing for a sailplane. They create expertise in static aeroelasticity and support the confidence in numerical calculation and optimization tools, which have been little used in the construction of sailplanes so far. For further development steps and with regard to an aeroelastic optimization, the model has to be iteratively adapted to changing parameters. In particular, this requires precise knowledge of the materials used and their characteristics, as these have a decisive influence on the elastic behavior of any structure. If anisotropic stiffness values are known for the compliant mechanisms, these can be implemented. Knowing strength values, a stress and strength analysis can be performed for the critical load cases. Furthermore, the DL model can be extended by a winglet in order to represent edge effects in the outer wing area more precisely. The water ballast can be omitted in order to investigate its influence on the wing torsion. Once the aerodynamic shape as well as the the positioning of the structural components have been determined, the structure can be optimized by means of Aeroelastic Tailoring. Moreover, dynamic aeroelastic phenomena such as flutter can be taken into account. Manufacturing aspects could be considered as well. For instance, research into the manufacturability could be carried out, including studies that investigate the practicability of fiber angle variations. Alternative production methods such as vacuum infusion with their process parameters could be evaluated with regard to their feasibility.

Bibliography

- Achleitner, J. (2016), CellSkin - A New Flexible Shell Structure for a Morphing Wing Aircraft, Presentation, ICCS19.
- Albano, E. & Rodden, W. P. (1969), A Doublet-Lattice Method for Calculating Lift Distributions on Oscillating Surfaces in Subsonic Flows, Technical report.
- Baier, H. (2011), Leichtbau, Lecture Notes, TUM.
- Butler, D. (2011), The Design of a Competition Sailplane, Soaring Café, available: <http://soaringcafe.com/2011/01/design-of-a-competition-sailplane/> (accessed october 15, 2018).
- Diab (2018), Divinycell H, Technical Data Sheet.
- Dillinger, J. (2014), Static Aeroelastic Optimization of Composite Wings with Variable Stiffness Laminates, PhD thesis.
- Dillinger, J., Abdalla, M., Klimmek, T. & Gürdal, Z. (2013), Static Aeroelastic Stiffness Optimization and Investigation of Forward Swept, Technical report.
- Drechsler, K., Eberl, C. & Zaremba, S. (2017), Production Technologies for Composite Parts, Lecture Notes, TUM.
- Drechsler, K. & Hartmann, M. (2017), Analysis and Design of Composite Structures, Lecture Notes, TUM.
- EASA (2003), 'CS-22 Sailplanes and Powered Sailplanes'.
- Gibbs, Y. (2017), 'NASA Armstrong Fact Sheet: X-29 Advanced Technology Demonstrator Aircraft'.
- ICAO (1976), 'U.S. Standard Atmosphere'.
- Kickert, R. (1988), 'Idaflieg Faserkennwerte'.
- Kress, G. (2004), Strukturanalyse mit FEM, ETH Zürich.

MSC (2016a), *Getting Started with MSC Nastran User's Guide*, MSC Software.

MSC (2016b), *MSC Nastran Quick Reference Guide*, MSC Software.

Salehar, L. (2015), Preliminary Design of a Compliant Mechanism for a Morphing Wing Leading Edge, Term Thesis, TUM.

Schlothauer, A. (2016), Strukturelle Auslegung und Aeroelastic Tailoring eines Segelflugzeug-Tragflügels mit formvariabler Vorderkante, Term Thesis, TUM.

Schwochow, J. (2012), Die aeroelastische Stabilitätsanalyse - ein praxisnaher Ansatz zur intervalltheoretischen Betrachtung von Modellierungsunsicherheiten am Flugzeug, PhD thesis.

Shirk, M. H. & Hertz, T. J. (1984), Aeroelastic Tailoring - Theory, Practice and Promise, Technical report.

Weinzierl, M., Achleitner, J. & Baier, H. (2015), 'Highly extensible skin of a variable geometry wing leading edge of a high-performance sailplane', *Technical Soaring* (Vol. 39, No. 1), 4–9.

Wiessmeier, M. (2011), Konzept einer formvariablen Tragflügelvorderkante bei einem Segelflugzeug mit innenliegender Ansteuerung über ein Rotary Drive System, Diploma Thesis, TUM.

Wright, J. R. (2015), *Introduction to Aircraft Aeroelasticity and Loads*, Wiley.

Declaration of Authorship

I declare that this thesis and the work presented in it are my own and have been generated by me as the result of my own original research.

I confirm that:

1. No part of this thesis has been previously submitted for a degree or any other qualification at any other university or institution than the Technical University of Munich.
2. Where I have consulted the published work of others, this is always clearly attributed and where I have quoted from the work of others, the source is always given. With the exception of such quotations, this thesis is entirely my own work.

.....

City, Date

.....

Signature

A Appendix

A.1 Reference Data from a Project Partner

Mass distribution and stiffness values for analytical calculations

y [m]	mass structure [kg]	x COG structure [1/c]	mass ballast [kg]	x COG ballast [1/c]	x shear center [1/c]	torsional stiffness [Nm ² /rad]	bending stiffness [N mm ²]
0,05	1,67	0,319	0	0	0,419	9E+99	9E+99
0,15	1,67	0,335	0	0	0,435	9E+99	9E+99
0,25	1,67	0,350	0	0	0,450	9E+99	9E+99
0,35	2,89	0,483	0	0	0,468	226097	4,00786E+11
0,45	1,48	0,465	1,450	0,251	0,489	190611	3,55805E+11
0,55	1,45	0,476	1,382	0,263	0,510	159309	3,08497E+11
0,65	1,43	0,482	1,344	0,269	0,520	142716	2,9906E+11
0,75	1,68	0,456	1,344	0,269	0,521	138850	2,89743E+11
0,85	1,67	0,479	1,343	0,270	0,522	135056	2,80572E+11
0,95	1,44	0,479	1,343	0,270	0,523	131338	2,7155E+11
1,05	1,44	0,480	1,342	0,270	0,523	127695	2,62676E+11
1,15	1,43	0,480	1,342	0,271	0,524	124127	2,53951E+11
1,25	1,43	0,480	1,341	0,271	0,525	120632	2,45373E+11
1,35	1,43	0,480	1,340	0,272	0,525	117208	2,3694E+11
1,45	1,42	0,481	1,340	0,272	0,526	114107	2,28915E+11
1,55	1,41	0,480	1,328	0,272	0,525	111567	2,21334E+11
1,65	1,41	0,482	1,316	0,271	0,525	109319	2,13945E+11
1,75	1,40	0,482	1,304	0,271	0,524	107105	2,06744E+11
1,85	1,39	0,477	1,292	0,270	0,523	104927	1,99727E+11
1,95	1,38	0,476	1,281	0,270	0,523	102784	1,92892E+11
2,05	1,37	0,476	1,269	0,270	0,522	100674	1,86235E+11
2,15	2,23	0,503	1,257	0,269	0,521	98599	1,79751E+11
2,25	2,22	0,503	1,246	0,269	0,521	96557	1,73439E+11
2,35	1,53	0,486	1,234	0,268	0,520	94548	1,67295E+11
2,45	1,53	0,486	1,223	0,268	0,519	92572	1,61315E+11
2,55	1,52	0,486	1,212	0,268	0,518	90627	1,55484E+11
2,65	1,51	0,486	1,200	0,267	0,518	88715	1,49797E+11
2,75	1,50	0,485	1,189	0,267	0,517	86835	1,44267E+11
2,85	1,48	0,485	1,178	0,267	0,516	84985	1,3889E+11
2,95	1,47	0,485	1,167	0,266	0,516	83167	1,33664E+11
3,05	1,46	0,485	1,156	0,266	0,515	81379	1,28586E+11
3,15	1,46	0,485	1,145	0,265	0,514	79620	1,23652E+11
3,25	1,45	0,484	1,134	0,265	0,514	77892	1,1886E+11
3,35	1,44	0,484	1,125	0,265	0,513	76514	1,1499E+11
3,45	1,42	0,485	1,116	0,265	0,513	75496	1,1117E+11
3,55	1,41	0,485	1,108	0,265	0,513	74509	1,07341E+11
3,65	1,18	0,468	1,099	0,265	0,513	73531	1,03501E+11
3,75	1,16	0,468	1,091	0,265	0,513	72562	99645697818
3,85	1,15	0,468	1,083	0,265	0,514	71603	95772920350
3,95	1,13	0,468	1,075	0,265	0,514	70653	91878562665
4,05	1,12	0,469	1,066	0,265	0,514	69712	87958813563
4,15	1,10	0,469	1,058	0,265	0,514	68780	84009643195
4,25	1,08	0,469	1,050	0,265	0,514	67857	80026810990
4,35	1,07	0,469	1,042	0,265	0,514	66944	76002231654
4,45	1,06	0,470	1,034	0,265	0,514	66039	71933668640
4,55	1,05	0,471	1,025	0,265	0,514	65084	68418800309
4,65	1,03	0,469	1,009	0,265	0,513	64022	65531021994
4,75	1,03	0,468	0	0	0,511	62911	62693568439
4,85	1,01	0,466	0	0	0,510	61810	59905197690
4,95	1,00	0,465	0	0	0,509	60720	57164643869

5,05	0,99	0,464	0	0	0,508	59641	54470615201
5,15	0,98	0,462	0	0	0,506	58573	51821791889
5,25	0,97	0,460	0	0	0,505	57516	49216823805
5,35	1,26	0,508	0	0	0,504	56469	46648816262
5,45	2,00	0,475	0	0	0,502	55433	44118929699
5,55	1,62	0,441	0	0	0,501	54407	41629822612
5,65	1,52	0,419	0	0	0,501	37612	33416215396
5,75	1,44	0,413	0	0	0,505	20948	31516700373
5,85	0,67	0,409	0	0	0,509	20199	29625636999
5,95	0,66	0,410	0	0	0,513	19465	27760132146
6,05	0,64	0,411	0	0	0,517	18748	25918863673
6,15	0,63	0,412	0	0	0,521	18048	24383432399
6,25	0,62	0,413	0	0	0,525	17365	22878761908
6,35	0,61	0,414	0	0	0,529	16698	21391793281
6,45	0,60	0,415	0	0	0,533	16047	19934418984
6,55	0,59	0,416	0	0	0,537	15414	18495722041
6,65	0,58	0,416	0	0	0,541	14785	17064836740
6,75	0,57	0,416	0	0	0,543	14063	15538827339
6,85	0,56	0,414	0	0	0,544	13270	14094290320
6,95	0,55	0,412	0	0	0,545	12510	12727044092
7,05	0,54	0,410	0	0	0,545	11782	11434225333
7,15	0,53	0,408	0	0	0,546	11085	10214954322
7,25	0,52	0,405	0	0	0,547	10418	9066171482
7,35	0,51	0,403	0	0	0,548	9782	7984506004
7,45	0,51	0,401	0	0	0,549	9151	7040672991
7,55	0,50	0,399	0	0	0,550	8483	6308869357
7,65	0,49	0,396	0	0	0,551	7810	5632036444
7,75	0,48	0,394	0	0	0,553	7179	5008079919
7,85	0,48	0,392	0	0	0,554	6589	4434080635
7,95	0,47	0,389	0	0	0,555	6038	3907252672
8,05	0,46	0,387	0	0	0,556	5523	3424907832
8,15	0,46	0,384	0	0	0,557	5044	2985399484
8,25	0,45	0,382	0	0	0,559	4586	2577268505
8,35	0,44	0,373	0	0	0,553	4041	2135582443
8,45	0,44	0,361	0	0	0,542	3438	1744140158
8,55	0,42	0,351	0	0	0,531	2904	1406106698
8,65	0,42	0,336	0	0	0,518	2489	1150234503
8,75	0,41	0,319	0	0	0,502	2163	914735082,3
8,85	0,41	0,301	0	0	0,487	1851	702447132,9
8,95	0,39	0,512	0	0	0,470	1562	513161991,1

Table A.1: Wing reference sizes.

Area	8.739 04 m ²
Mean chord	0.4855 m
Reference chord	0.507 54 m
Aerodynamic center (x)	0.1368 m
Aspect ratio	37.075
Taper ratio	0.268 83

A.2 Sample Static Aeroelastic Solution Sequence

```

1  $$ #####
2  $$ Language:          NASTRAN Input Deck
3  $$ Date:             2019/02/25
4  $$ Author:          ILLENBERGER GERRIT
5  $$ #####
6  $$ -----
7
8  SOL144
9
10 $$ -----
11 $$ -----
12
13 CEND
14
15 TITLE = NASTRAN_DLM
16 ECHO = NONE
17
18 DISPLACEMENT (SORT1,PLOT) = ALL
19 STRESS (SORT1,PLOT) = ALL
20 STRAIN (SORT1,PLOT) = ALL
21
22 SUBCASE 1
23   TRIM = 1
24   SUPORT1 = 1
25
26   SPC = 100
27
28   AESYMXX = SYMMETRIC
29   AESYMY = ASYMMETRIC
30
31   AEROF = ALL
32   APRES = ALL
33
34 $$ -----
35 $$ -----
36
37 BEGIN BULK
38
39 PARAM,GRDPNT,0
40 PARAM,BAILOUT,-1
41 PARAM,PRGPST,NO
42 PARAM,DBALL,SCRATCH
43 PARAM,POST,-1
44 PARAM,AUTOMSET, YES
45
46 $$ -----
47 $$                               Boundary Conditions
48 $$ -----
49 $<-[1]-><-[2]-><-[3]-><-[4]-><-[5]-><-[6]-><-[7]-><-[8]-><-[9]-><-[10]->
50 SPC          1      83178      1246      0.0
51 SUPORT1      1      83178          35
52 SPCADD       100          1          2
53
54
55 $$ -----
56 $$                               Static Aeroelastic Parameters
57 $$ -----
58 $<--1--><-- 2--><-- 3--><-- 4--><-- 5--><-- 6--><-- 7--><-- 8--><-- 9--><--10-->
59 $AEROS  ACSID  RCSID  REFC  REFB  REFS  SYMXZ  SYMY
60 AEROS      489    8920  4360000
61

```

```

62 $<--1--><-- 2--><-- 3--><-- 4--><-- 5--><-- 6--><-- 7--><-- 8--><-- 9--><--10-->
63 AESTAT 4010 ANGLEA
64 AESTAT 4011 URDD3
65 AESTAT 4012 PITCH
66 AESTAT 4013 URDD5
67
68 $$ -----
69 $$                               Trim
70 $$ -----
71 $<--1--><-- 2--><-- 3--><-- 4--><-- 5--><-- 6--><-- 7--><-- 8--><-- 9--><--10-->
72 $TRIM ID MACH Q LABEL1 UX1 LABEL2 UX2 AEQR
73 TRIM 1 0.1795 2.2874-3URDD3 +9810 PITCH 0.0 1.0
74 URDD5 0.0
75
76 INCLUDE 'panel.nastran'
77 INCLUDE 'camber.nastran'
78 INCLUDE 'csm.nastran'
79 INCLUDE 'mass.nastran'
80
81 ENDDATA

```

A.3 Further Simulation Results

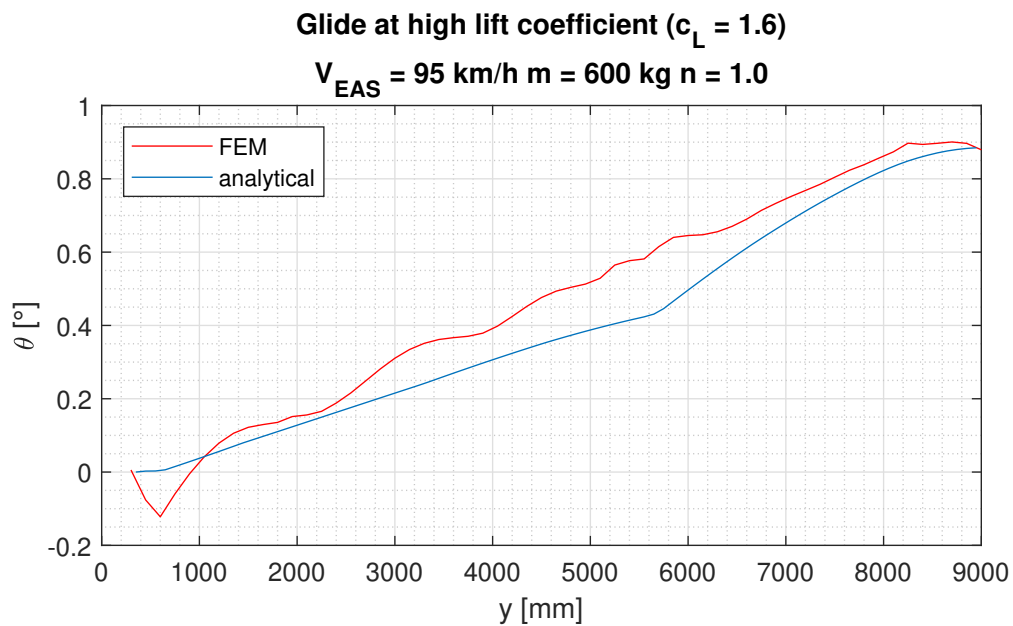


Figure A.1: Wing twist at load case 117.

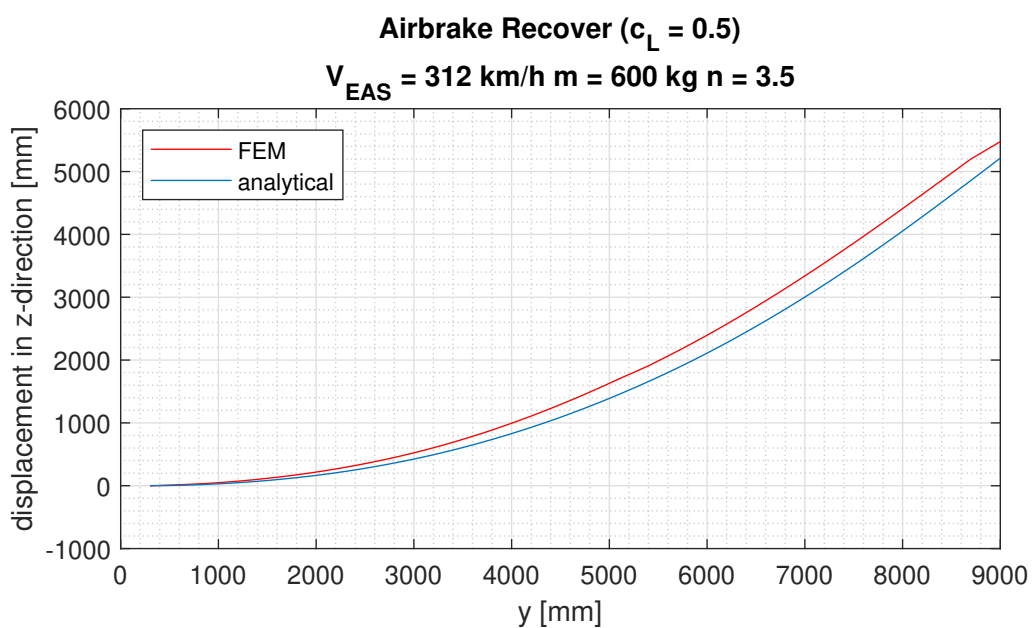


Figure A.2: Wing deflection at load case 103.

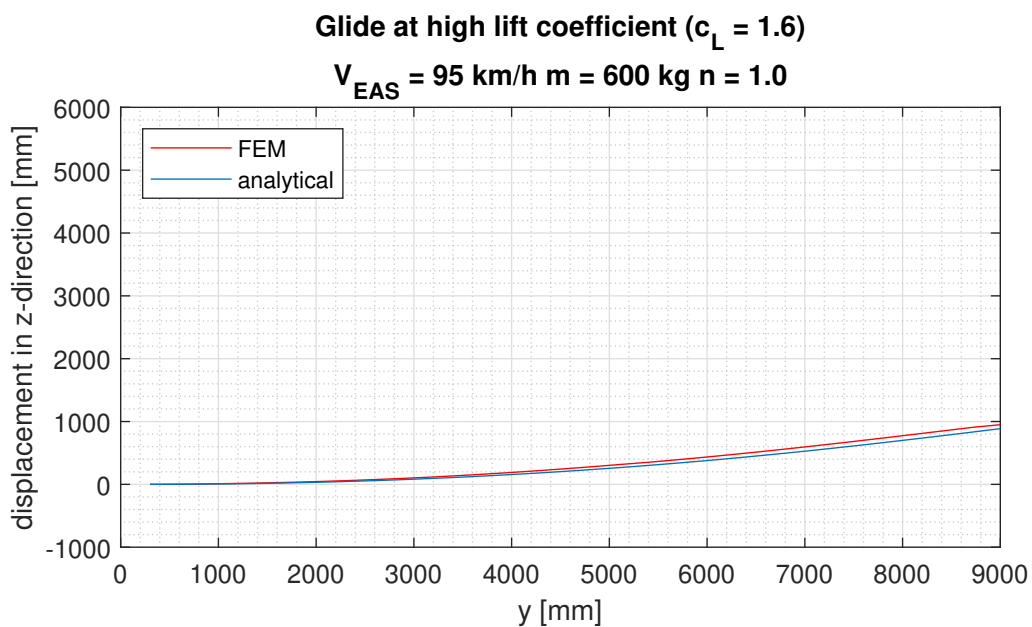


Figure A.3: Wing deflection at load case 117.

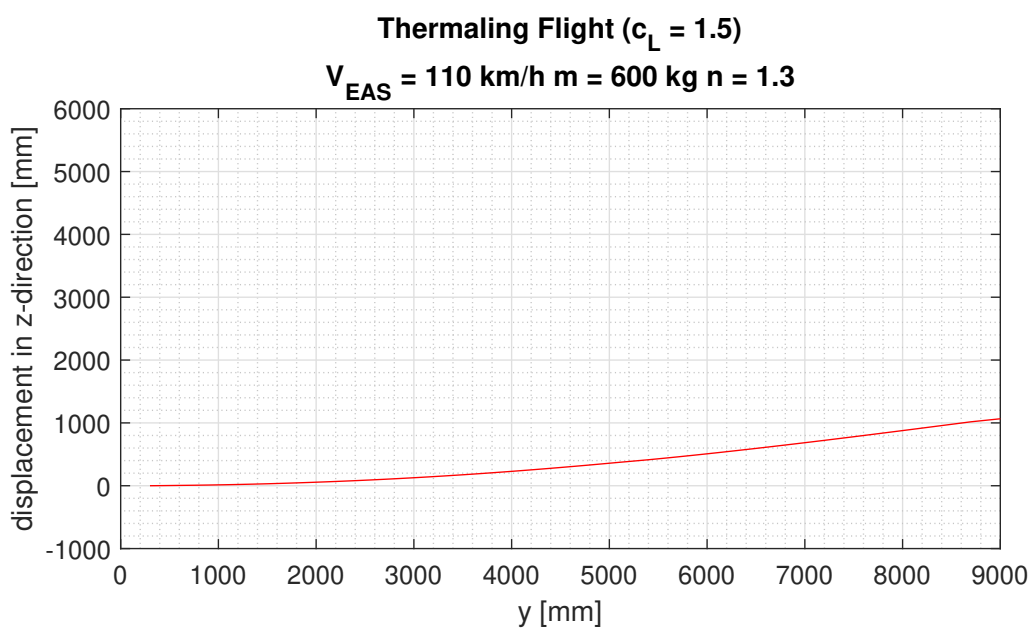


Figure A.4: Wing deflection at load case 202

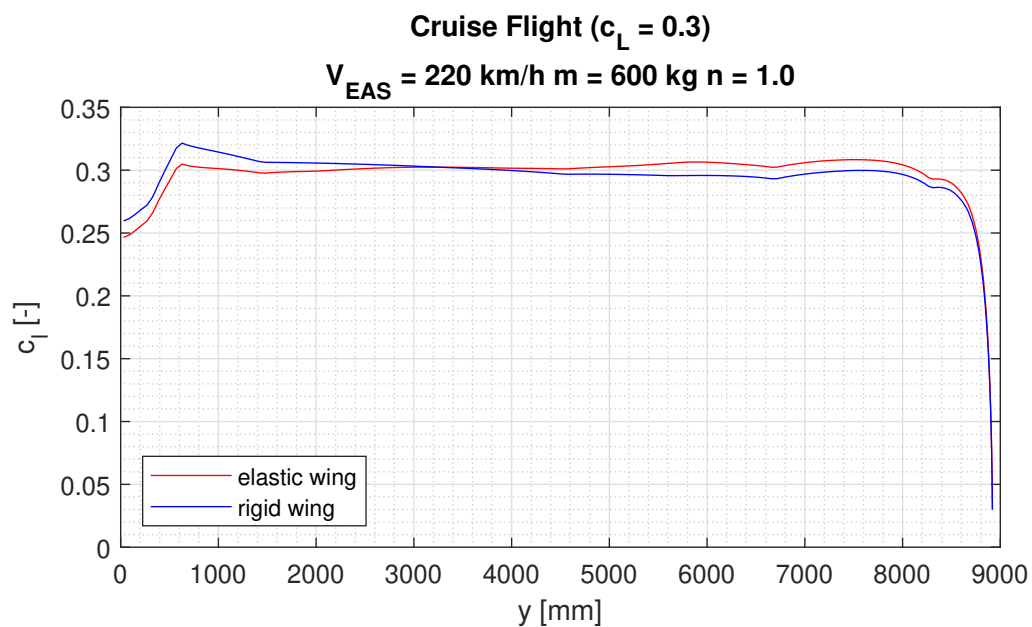


Figure A.5: Local lift coefficient distribution at load case 201.

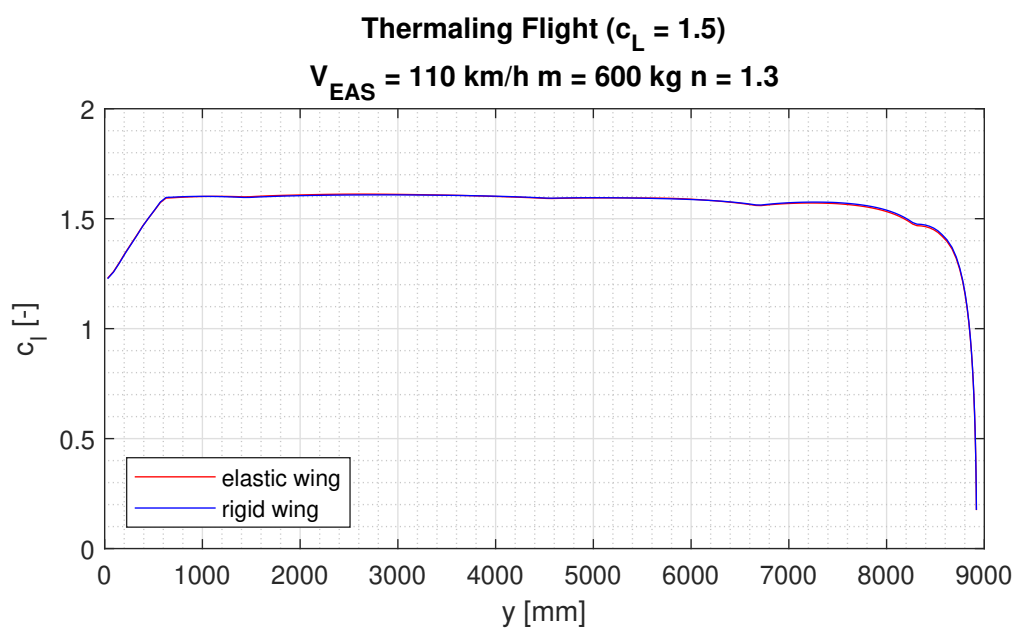


Figure A.6: Local lift coefficient distribution at load case 202.

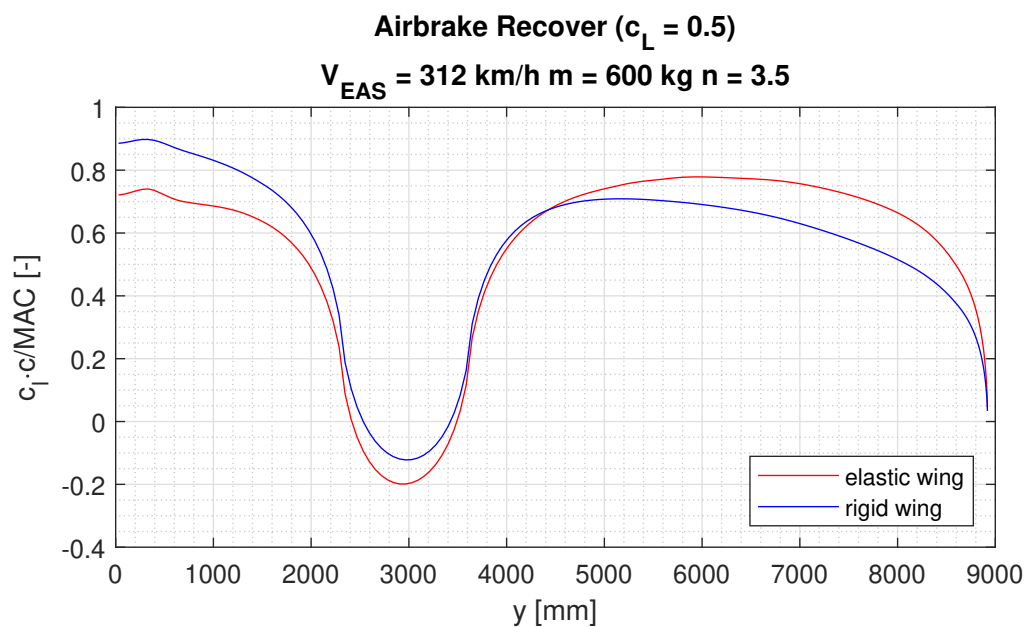


Figure A.7: Elliptical lift distribution at load case 103.

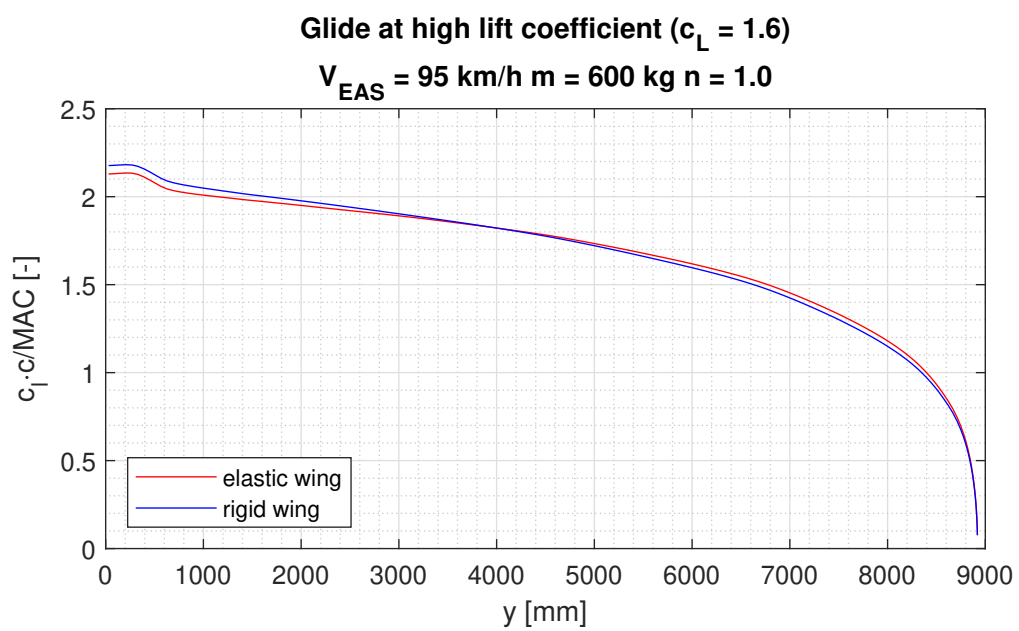


Figure A.8: Elliptical lift distribution at load case 117.